

# **ROBUST AND EFFICIENT METHODS FOR SEGMENTATION OF INTIMA MEDIA THICKNESS OF THE COMMON CAROTID ARTERY**

Thesis

Submitted in partial fulfilment of the requirements for the degree of  
DOCTOR OF PHILOSOPHY

by

**NAGARAJ YAMANAKKANAVAR**

**(145090EC14F06)**



DEPARTMENT OF ELECTRONICS AND COMMUNICATION ENGINEERING  
NATIONAL INSTITUTE OF TECHNOLOGY KARNATAKA  
SURATHKAL, MANGALORE -575025

SEPTEMBER, 2018

# DECLARATION

I hereby *declare* that the research thesis entitled **Robust and efficient methods for segmentation of intima media thickness of the common carotid artery** which is being submitted to the *National Institute of Technology Karnataka, Surathkal* in partial fulfilment of the requirement for the award of the Degree of *Doctor of Philosophy* in **Department of Electronics and Communication Engineering** is a *bonafide report of the research work carried out by me*. The material contained in this research thesis has not been submitted to any University or Institution for the award of any degree.

NAGARAJ YAMANAKKANAVAR,

Reg. No. 145090EC14F06

Department of Electronics and Communication Engineering.

Place: NITK-Surathkal.

Date:

# CERTIFICATE

This is to certify that the research thesis entitled **Robust and efficient methods for segmentation of intima media thickness of the common carotid artery** submitted by **Nagaraj Yamanakkanavar** (Register Number:145090EC14F06) as the record of the research work carried out by him, is accepted as the *Research Thesis submission* in partial fulfilment of the requirements for the award of degree of **Doctor of Philosophy**.

Dr.A.V.Narasimhadhan  
Research Guide  
Assistant Professor  
Department of Electronics and Communication Engineering  
NITK Surathkal-575025

Chairman-DRPC  
(Signature with Date and Seal)

## Acknowledgements

It would not have been possible to write this doctoral thesis without the help and support of the kind people around me, to only some of whom it is possible to give particular mention here.

First and foremost, I want to offer this endeavour to the GOD almighty for the wisdom she bestowed upon me, the strength, peace of mind and good health in order to furnish this research. I would like to express my gratitude towards my family for the encouragement which helped me in completion of this thesis.

It is genuine pleasure to express my deep sense of thanks and gratitude to my mentor, philosopher, and guide Dr. A V Narasimhadhan, Department of Electronics and Communication Engineering, National Institute of Technology, Karnataka. His dedication and keen interest on me at every stage of my research had been solely responsible for completing my work.

I owe a deep sense of gratitude to Dr. Ram Shenoy Basti, Radio-Diagnosis, Father Muller Medical Hospital, Mangalore and Raju Dibbad, Radiologist, Hubli Scan center, Hubballi for their help in collecting the data, validating the results, timely suggestions with kindness and enthusiasm.

I would like to thank my committee members, Dr. Raghavendra B S, Department of Electronics and Communication Engineering and Dr. Satyanarayana Engu, Department of Mathematical and Computational Sciences, National Institute of Technology, Karnataka for their advice and unsurpassed knowledge.

I thank my colleague Asha C S for all her support and advice in the initial stages of my work, and for many interesting technical discussions.

Furthermore, I am thankful to Dr. Jasjit Suri, Atheropoint, CA, USA for his valuable support in my research work.

Last but not least, I would like to thank my friends and colleagues at the National Institute of Technology, Karnataka for their encouragement and moral support which made my stay and studies in surathkal more enjoyable.

This thesis is dedicated to  
**My beloved Parents**

## Abstract

Cardiovascular diseases are the third leading cause of death worldwide. The primitive indication of the possible onset of a cardiovascular disease is atherosclerosis, which is the accumulation of plaque on the arterial wall. To assess carotid atherosclerosis, non invasive ultrasound imaging modality is preferred over other invasive methods due to their safer profile and ability to explore atherosclerosis in its early stages. The intima media thickness (IMT) of the common carotid artery (CCA) is an early marker of the development of cardiovascular disease. The computation of IMT and the delineation of carotid plaque are significant predictors for the clinical diagnosis of the risk of stroke. However, manual measurement of the IMT is tedious, error-prone and subjected to observer variability. Hence, there is a growing interest in the development of automated software system for the measurement of IMT from the carotid ultrasound images. The development of such automated systems is the primary objective of this research.

The presence of speckle noise in carotid ultrasound image reduces the quality of image and automatic human interpretation. Carotid ultrasound images have multiplicative speckle noise and it is difficult to remove as compared to the additive noises. The despeckling filters have a greater restriction on preservation of edges and characteristics. For a robust diagnosis, carotid ultrasound images must be free from speckle noise. To address this problem, we propose the use of a Bayesian least square estimation method for the reduction of speckle noise in logarithmic space. In addition, one of the widely accepted method named optimized Bayesian non local mean filter is adopted in our work to reduce the speckle noise in ultrasound images. The traditional denoising techniques require a significant amount of execution time because of the iterative steps involved. To overcome this problem, we propose the use of Wiener filtering in the wavelet domain. Wiener filter smoothens the image while retaining the edges, and performs region of interest (ROI) extraction significantly faster than other similar techniques. Further, the state-of-the-art enhancement techniques are adopted in order to increase the contrast after denoising. Finally, the comparative study of edge detection algorithms is done based on the framework of despeckling carotid ultrasound images.

In the literature, several edge-based algorithms is proposed for estimating the IMT. However, accurate segmentation still remains a challenge. Extracting the ROI prior to the segmentation from carotid ultrasound images has been very much challenging as it is the basis for further image analysis, interpretation, and classification. In order to extract ROI of ultrasound images, several types of morphological functions are applied. The identified region is analysed to detect the carotid wall boundaries. The ROI extraction must be performed properly otherwise it leads to a lot of misinterpretation, and false measurement. To address this problem, we present novel approaches for automatic ROI extraction followed by new segmentation algorithms based on threshold-based wind driven optimization, support vector machine and structured random forest classifier for measurement of the IMT of the CCA. The results obtained are compared with the state-of-the-art algorithms, and the results show that the proposed methods outperform the existing techniques in terms of IMT segmentation accuracy and computational speed.

**Keywords:** Ultrasound Imaging, Common Carotid Artery, Intima Media Thickness, Denoising, Support Vector Machine, Wind Driven Optimization, Structured Random Forest.

# Contents

|  |           |
|--|-----------|
| Acknowledgements . . . . .                                     | i         |
| Dedication . . . . .   | ii        |
| Abstract . . . . .   | iii       |
| List of figures . . . . .                                      | vii       |
| List of tables . . . . .                                       | xii       |
| Nomenclature . . . . .   | xiv       |
| Abbreviations . . . . .  | xiv       |
| <b>1 INTRODUCTION</b>  | <b>1</b>  |
| 1.1 Background on Cardiovascular Diseases . . . . .            | 1         |
| 1.2 Brief review on Ultrasound Imaging . . . . .               | 3         |
| 1.2.1 Plaque characteristics . . . . .                         | 5         |
| 1.2.2 IMT of the Common Carotid Artery . . . . .               | 5         |
| 1.3 Motivation . . . . .                                       | 6         |
| 1.4 Problem Statement . . . . .                                | 7         |
| 1.5 Research Objectives . . . . .                              | 8         |
| 1.6 Major Contribution . . . . .                               | 8         |
| 1.7 Organization of the Thesis . . . . .                       | 9         |
| <b>2 COMMON CAROTID ARTERY SEGMENTATION APPROACHES</b>         | <b>11</b> |
| 2.1 General frame work for carotid wall segmentation . . . . . | 11        |
| 2.1.1 Despeckling filters . . . . .                            | 12        |
| 2.1.2 Region of Interest (ROI) . . . . .                       | 13        |
| 2.1.3 Gradient-based Segmentation . . . . .                    | 13        |
| 2.1.4 Threshold-based Segmentation . . . . .                   | 15        |
| 2.1.5 Learning-based Segmentation . . . . .                    | 18        |
| 2.2 Challenges during Segmentation . . . . .                   | 19        |



|          |  |           |
|----------|--|-----------|
| 2.3      | Performance metrics for despeckling and IMT measurement . . . . .                  | 20        |
| 2.3.1    | Performance metrics for despeckling filters . . . . .                              | 20        |
| 2.3.2    | Validation metrics for IMT measurement . . . . .                                   | 22        |
| 2.4      | Summary . . . . .  | 24        |
| <b>3</b> | <b>DENOISING AND EDGE DETECTION OF COMMON CAROTID ARTERY IMAGES</b>                | <b>27</b> |
| 3.1      | Related work on despeckling filters and edge detection methods . . . . .           | 28        |
| 3.2      | Proposed Methodology for despeckling using BLSE . . . . .                          | 29        |
| 3.2.1    | Results . . . . .  | 31        |
| 3.3      | Comparison of edge detection and despeckling on carotid ultrasound images          | 37        |
| 3.3.1    | Automatic ROI extraction . . . . .   | 38        |
| 3.3.2    | Results . . . . .  | 40        |
| 3.4      | Summary . . . . .  | 47        |
| <b>4</b> | <b>AUTOMATIC SEGMENTATION OF INTIMA MEDIA COMPLEX OF THE COMMON CAROTID ARTERY</b> | <b>49</b> |
| 4.1      | Proposed method based on Support Vector Machine . . . . .                          | 49        |
| 4.1.1    | Automatic Extraction of the ROI . . . . .  | 50        |
| 4.1.2    | Segmentation using SVM . . . . .   | 53        |
| 4.1.3    | Results . . . . .  | 54        |
| 4.2      | Proposed method based on Wind Driven Optimization technique . . . . .              | 59        |
| 4.2.1    | Background of Wind Driven Optimization Technique . . . . .                         | 60        |
| 4.2.2    | Proposed Methodology . . . . .   | 63        |
| 4.2.3    | WDO for the Optimization of Otsu's Function . . . . .                              | 67        |
| 4.2.4    | Results . . . . .  | 68        |
| 4.2.5    | Discussion . . . . .   | 73        |
| 4.3      | Proposed method based on Structured Random Forest . . . . .                        | 77        |
| 4.3.1    | Related Work on Structured Random Forest . . . . .                                 | 77        |
| 4.3.2    | Proposed Methodology . . . . .   | 78        |
| 4.3.3    | Results . . . . .  | 87        |
| 4.3.4    | Discussion . . . . .   | 91        |
| 4.4      | Summary . . . . .  | 94        |

|   |            |
|---|------------|
| <b>5 CONCLUSIONS AND FUTURE WORK</b>    | <b>97</b>  |
| 5.1 Conclusions . . . . .               | 97         |
| 5.2 Future Work . . . . .               | 98         |
| <b>Bibliography</b>                     | <b>100</b> |
| References . . . . .                    | 113        |
| <b>Publications based on the thesis</b> | <b>114</b> |

# List of Figures

|     |   |    |
|-----|---|----|
| 1.1 | Side and front view of common carotid artery ( <a href="https://wiki/Carotidartery">https://wiki/Carotidartery</a> ). . . . .   | 2  |
| 1.2 | (a) Normal and abnormal blood flow in the common carotid artery. (b) Carotid artery with plaque ( <a href="https://www.vascularweb.org">https://www.vascularweb.org</a> ). . . . .  | 3  |
| 1.3 | Diagnosis using ultrasound imaging.(a) Common Carotid Artery.(b) Carotid duplex with ultrasound probe.(c) B-mode longitudinal image. ( <a href="http://www.biosim.ntua.gr/en">http://www.biosim.ntua.gr/en</a> ) . . . . .  | 4  |
| 1.4 | Ultrasound B-mode longitudinal image with manually delineated plaque. . . . .   | 4  |
| 1.5 | Illustration of the common carotid artery in longitudinal and transverse projection. . . . .  | 6  |
| 2.1 | General flow diagram for segmentation of IMT of the CCA. . . . .  | 12 |
| 3.1 | Carotid ultrasound images with speckle noise variance ( $\sigma^2$ ) 0.1. (a) Noise-free image. (b) Noisy image. (c) Median. (d) SRAD. (e) NLM. (f) Total-Variation. (g) DPAD. (h) Lee. (i) Frost. (j) Wavelet filter. (k) Proposed filter. . . . .   | 32 |
| 3.2 | SSIM factor of carotid ultrasound images with variance ( $\sigma^2$ ) 0.1 (Brighter indicates better SSIM value). (a) Noise-free image. (b) Noisy image. (c) Median. (d) SRAD. (e) NLM. (f) Total-Variation. (g) DPAD. (h) Lee. (i) Frost. (j) Wavelet filter. (k) Proposed filter. . . . . | 33 |
| 3.3 | Carotid ultrasound images with speckle noise variance ( $\sigma^2$ ) 0.5. (a) Noise-free image. (b) Noisy image. (c) Median. (d) SRAD. (e) NLM. (f) Total-Variation. (g) DPAD. (h) Lee. (i) Frost. (j) Wavelet filter. (k) Proposed filter. . . . .   | 35 |

|      |   |    |
|------|---|----|
| 3.4  | SSIM factor of carotid ultrasound images with variance ( $\sigma^2$ ) 0.5 (Brighter indicates better SSIM value). (a) Noise-free image. (b) Noisy image. (c) Median. (d) SRAD. (e) NLM. (f) Total-Variation. (g) DPAD. (h) Lee. (i) Frost. (j) Wavelet filter. (k) Proposed filter. . . . .   | 36 |
| 3.5  | Outline of ROI extraction. . . . .  | 38 |
| 3.6  | Automatic extraction of ROI. (a) Original carotid longitudinal ultrasound image. (b) De-speckled image using BLSE filter. (c) Enhancement using TV- $L^1$ norm. (d) Conversion to the binary image with automatic thresholding procedure. (e) Morphological operation on the binary image. (f) Canny edge detection. (g) Extraction of the near and Far wall. (h) Automatic ROI extraction. . . . . | 39 |
| 3.7  | Edge detection techniques for carotid ultrasound images of Dataset 1 with noise variance of 0.05. . . . .   | 40 |
| 3.8  | Edge detection techniques for carotid ultrasound images of Dataset 2 with noise variance of 0.05. . . . .   | 41 |
| 3.9  | Structural similarity index (Brighter indicates better SSIM value) of carotid ultrasound images of Dataset 1 with variance of 0.05. . . . .   | 41 |
| 3.10 | Structural similarity index (Brighter indicates better SSIM value) of carotid ultrasound images of Dataset 2 with variance of 0.05. . . . .   | 42 |
| 3.11 | Edge detection techniques for carotid ultrasound images of Dataset 1 with noise variance of 0.1. . . . .  | 43 |
| 3.12 | Edge detection techniques for carotid ultrasound images of Dataset 2 with noise variance of 0.1. . . . .  | 44 |
| 3.13 | Structural similarity index (Brighter indicates better SSIM value) of carotid ultrasound images of Dataset 1 with variance of 0.1. . . . .  | 45 |
| 3.14 | Structural similarity index (Brighter indicates better SSIM value) of carotid ultrasound images of Dataset 2 with variance of 0.1. . . . .  | 46 |
| 4.1  | Outline of ROI extraction. . . . .  | 50 |

|      |   |    |
|------|---|----|
| 4.2  | Automatic extraction of ROI. (a) Original carotid longitudinal ultrasound image. (b) Despeckle image using BLSE filter. (c) Enhancement using TV- $L^1$ norm. (d) Dilation of the image. (e) Erosion of the image. (f) Morphological gradient of the image. (g) Boundaries of the watershed regions of the morphological gradient image over segmentation. (h) Boundaries of the watershed regions of the morphological gradient image over segmentation resolved. (i) Morphologically reconstructed image. (j) Largest Object in the lower half of the image. (k) ROI cropped image. . . . . | 51 |
| 4.3  | (a) Original longitudinal carotid ultrasound sample image with manual delineation from an expert. (b) Automated delineation using DP. (c) Automated delineation using MB. (d) Automated delineation using SS. (e) Automatic segmentation using NN. (f) Automated delineation using proposed method. . . . .   | 55 |
| 4.4  | Regression analysis plots comparing automated segmentation measurements with manual measurement. (a) DP (b) MB (c) SS (d) NN (e) Proposed Method.   | 57 |
| 4.5  | Box plots comparing automated segmentation measurements with manual measurement. (a) DP (b) MB (c) SS (d) NN (e) Proposed Method. . . . .   | 58 |
| 4.6  | Outline of ROI extraction. . . . .  | 64 |
| 4.7  | Automatic extraction of ROI. (a) Original carotid longitudinal ultrasound image. (b) De-speckled image using OBFLM filter. (c) Enhancement using TV- $L^1$ norm. (d) Conversion of the binary image with automatic thresholding procedure. (e) Area opening for removing small objects. (f) Dilation for to seal the plaque contour. (g) Canny edge detection. (h) Extraction of the near and Far wall. (i) Automatic ROI extraction. . . . .   | 65 |
| 4.8  | Flowchart of WDO implementation. . . . .  | 68 |
| 4.9  | (a) Original longitudinal carotid ultrasound sample image of Dataset1 with manual delineation from an expert. (b) Automated delineation using Model-based approach. (c) Automated delineation using Dynamic programming. (d) Automated delineation using Snake contour. (e) Automated delineation using proposed method. . . . .  | 71 |
| 4.10 | (a) Original longitudinal carotid ultrasound sample image of Dataset2 with manual delineation from an expert. (b) Automated delineation using MB approach. (c) Automated delineation using DP. (d) Automated delineation using SS approach. (e) Automated delineation using proposed method. . . .  | 72 |

|  |    |
|--|----|
| 4.11 Bland Altman plots of the mean against the difference in the IMT mean values estimated for 90 carotid ultrasound images (automatic segmentation corresponding to the ground truth data). a) MB b) DP c) SS d) Proposed Method. . . . .  | 73 |
| 4.12 The mean intima-media thickness calculated for the database of 90 carotid ultrasound images for the automatic segmentation (IMT_mean_AS) and ground truth data (IMT_mean_GT). a) MB b) DP c) SS d) Proposed Method. . . . .   | 74 |
| 4.13 Regression analysis plots comparing automated segmentation measurements with manual measurement. a) MB b) DP c) SS d) Proposed Method. . . . .  | 75 |
| 4.14 Outline of ROI extraction. . . . .  | 79 |
| 4.15 Block diagram of denoising method. . . . .  | 79 |
| 4.16 Automatic extraction of ROI. (a) Original carotid longitudinal ultrasound image. (b) De-speckled image using Wiener filter in the wavelet domain. (c) Enhancement using adaptive gamma correction. (d) Conversion of the binary image with automatic thresholding procedure. (e) Area opening for remove smaller objects. (f) dilation is for filling gaps and holes in the plaque contour. (g) Edge detection using canny operator. (h) The cropped canny edge detected an image. (i) Center point is detected based on maximum zeros lies on the vertical line. (j) Near-wall extraction. (k) ROI extraction. . . . . | 81 |
| 4.17 (a) Selection of line in the binary image for detection of a center point. (b) The intensity profile of the column denoted by a vertical line in the binary image. (c) The vertical line is differentiated based on positive peak $p$ and negative peak $q$ . . . . .   | 82 |
| 4.18 Pictorial representation of an ensemble of independent trees in the training process. . . . .   | 85 |
| 4.19 Manual delineation from an expert and Automated segmentation IMT using DP, MB, SS, WDO, NN and Proposed method of longitudinal carotid ultrasound six sample images. . . . .  | 88 |
| 4.20 The mean IMT (using MAD metric) calculated for the database of 70 carotid ultrasound images for ground truth data (IMT_mean_GT) and the automatic segmentation (IMT_mean_AS) of DP, MB, SS, NN, WDO, and proposed method(PM). . . . .   | 90 |

|      |  |    |
|------|--|----|
| 4.21 | Bland Altman plots of the mean against the difference in the IMT mean values (automatic segmentation corresponding to the ground truth data) (using MAD metric). a) DP b) MB c) SS d) NN e) WDO f)Proposed Method. . . . | 91 |
| 4.22 | Regression analysis plots comparing automated segmentation measurements with manual measurement (using MAD metric). a) DP b) MB c) SS d) NN e) WDO f) Proposed Method. . . . .   | 92 |

# List of Tables

|     |  |    |
|-----|--|----|
| 2.1 | Overview of despeckle filtering Techniques . . . . .   | 14 |
| 2.2 | Overview of ultrasound IMT segmentation techniques . . . . .   | 16 |
| 2.3 | Advantages and limitation of carotid wall segmentation methods . . . . .   | 18 |
| 3.1 | The quality metrics evaluated with variance of 0.1 . . . . .   | 31 |
| 3.2 | The quality metrics evaluated with variance of 0.5 . . . . .   | 34 |
| 3.3 | Mean PSNR, Mean MSE, Mean CoC and Mean SSIM of Lee denoising filter with different edge detection techniques for 50 carotid ultrasound images. . . . .   | 42 |
| 3.4 | Mean PSNR, Mean MSE, Mean CoC and Mean SSIM of SRAD denoising filter with different edge detection techniques for 50 carotid ultrasound images. . . . .  | 43 |
| 3.5 | Mean PSNR, Mean MSE, Mean CoC and Mean SSIM of OBFLM denoising filter with different edge detection techniques for 50 carotid ultrasound images. . . . .   | 44 |
| 3.6 | Mean PSNR, Mean MSE, Mean CoC and Mean SSIM of Proposed denoising filter with different edge detection techniques for 50 carotid ultrasound images. . . . .                                      | 45 |
| 4.1 | Cross Validation of 49 ultrasound carotid images. . . . .  | 54 |
| 4.2 | Mean IMT values of automated segmentation (AS) method and the ground truth (GT) for 49 carotid ultrasound images. . . . .  | 56 |
| 4.3 | Validation(out of 5) of ultrasound carotid images from the radiology expert. . . . .   | 59 |
| 4.4 | Parameters used for the WDO: . . . . .   | 69 |
| 4.5 | Mean IMT values, R-correlation co-efficient, IOE-intra observer error, CV-coefficient variation and mean bias of automated method and the ground truth for 90 carotid ultrasound images. . . . . | 70 |
| 4.6 | Validation(out of 5) of ultrasound carotid images from the radiology expert. . . . .   | 76 |



|      |  |    |
|------|--|----|
| 4.7  | Mean IMT values, CV-coefficient variation, R-correlation co-efficient, mean bias and execution time of automated method and the ground truth for 70 carotid ultrasound images. . . . . | 89 |
| 4.8  | Parameter setting used for Dynamic programming, Model based, Snake segmentation and WDO algorithms. . . . .  | 93 |
| 4.9  | Validation(out of 5) of ultrasound carotid images from the radiology experts. . . . .  | 93 |
| 4.10 | Summary of IMC segmentation algorithm using other techniques . . . . .   | 94 |

## Nomenclature

| Symbol     | Meaning  |
|------------|--|
| $L$        | Number of threshold levels                     |
| $RT$       | Temperature in physical model                  |
| $\rho$     | Density of air parcel                          |
| $a$        | Acceleration of air parcel                     |
| $F$        | Force acting on air parcel                     |
| $\delta V$ | Finite value of air parcel                     |
| $\mu$      | Coefficient of friction                        |
| $u$        | Velocity of the air parcel                     |
| $g$        | Gravitational force                            |
| $\Omega$   | Rotation of the earth                          |
| $l_{opt}$  | Location of the air parcel                     |
| $l_{curr}$ | Position of the air parcel                     |
| $P_{opt}$  | Optimal pressure value                         |
| $P_{curr}$ | Pressure of the air parcel at current location |
| $C$        | Constant Coriolis effect                       |
| $u_{max}$  | Maximum velocity value                         |
| $l_{max}$  | Maximum position value                         |
| $R$        | Correlation Coefficient                        |

## Abbreviations

| <b>Abbreviation</b> | <b>Expansion</b>           | <b>Abbreviation</b> | <b>Expansion</b>                        |
|---------------------|----------------------------|---------------------|---|
| CCA                 | Common Carotid Artery      | SD                  | Standard Deviation                      |
| CVD                 | Cardiovascular Disease     | RAM                 | Random Access Memory                    |
| IMT                 | Intima Media Thickness     | NLM                 | Non Local Mean                          |
| IMC                 | Intima Media Complex       | SVM                 | Support Vector Machine                  |
| WHO                 | World Health Organisation  | WDO                 | Wind Driven Optimization                |
| US                  | Ultrasound                 | IQR                 | Inter Quartile Range                    |
| TV                  | Total Variation            | DP                  | Dynamic Programming                     |
| ICA                 | Internal Carotid Artery    | MB                  | Modal Based                             |
| ECA                 | External Carotid Artery    | SS                  | Snake Segmentation                      |
| LI                  | Lumen Intima               | NN                  | Neural Network                          |
| MA                  | Media Adventitia           | RBF                 | Radial Basis Function                   |
| AS                  | Automatic Segmentation     | SSIM                | Structural Similarity Index Map         |
| GT                  | Ground Truth               | AGC                 | Adaptive Gamma Correction               |
| CV                  | Coefficient of Variation   | MRI                 | Magnetic Resonance Imaging              |
| MAD                 | Mean Absolute Distance     | SNR                 | Signal Noise Ratio                      |
| PSNR                | Peak Signal Noise Ratio    | SRF                 | Structured Random Forest                |
| MSE                 | Mean Square Error          | BLSE                | Bayesian Least Square Estimation        |
| RMSE                | Root Mean Square Error     | OBNLM               | Optimized Bayesian Non Local Mean       |
| IQI                 | Image Quality Index        | DPAD                | Detail Preserve Anisotropic Diffusion   |
| CoC                 | Correlation of Coefficient | SRAD                | Speckle Reduction Anisotropic Diffusion |
|                     |                            | PCA                 | Principle Component Analysis            |

# Chapter 1

## INTRODUCTION

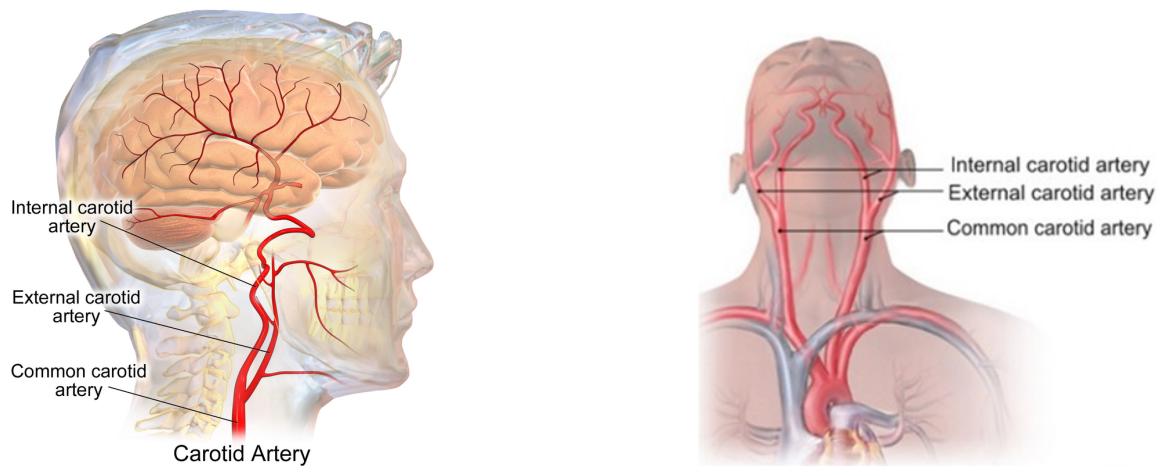
The rapid progression of medical image processing techniques has benefited to the mankind and plays an important role in clinical diagnosis. The current advances in medical imaging help to view the human body in order to diagnose and monitor medical conditions. The imaging techniques such as ultrasound (US), magnetic resonance imaging (MRI) and X-ray imaging give an image information by which the radiologist has to analyse and evaluate comprehensively in shorter time. Early detection of the cardiovascular diseases (CVDs) allows the observer to follow up on the subject. Hence, the main objective is to derive better tools that help to interpret the images.

In this chapter, we present brief review on CVDs which are associated with the common carotid artery (CCA), and description of the ultrasound imaging. Section 1.1 describes an introduction for the CVDs and explains how medical image processing helps in the assessment of risk of stroke. Section 1.2 explains about the ultrasound imaging techniques. Section 1.3 presents the motivation of the research work. Section 1.4 explains about the problem statement for the research work, followed by research objectives are given in section 1.5. In section 1.6, the major contributions of the thesis are explained. Finally, a conclusive summary of the chapters is presented in section 1.7.

### 1.1 Background on Cardiovascular Diseases

In a recent survey (WHO (2013)), it was found that approximately 17.5 million people die owing to CVDs (Approximately 31% of all global deaths). The main cause of cardiovascular diseases is atherosclerosis (Walker *et al.* (1995)), which is the accumulation of plaque on the arterial wall. The incidence of stroke is associated with the rupture of atheroscle-

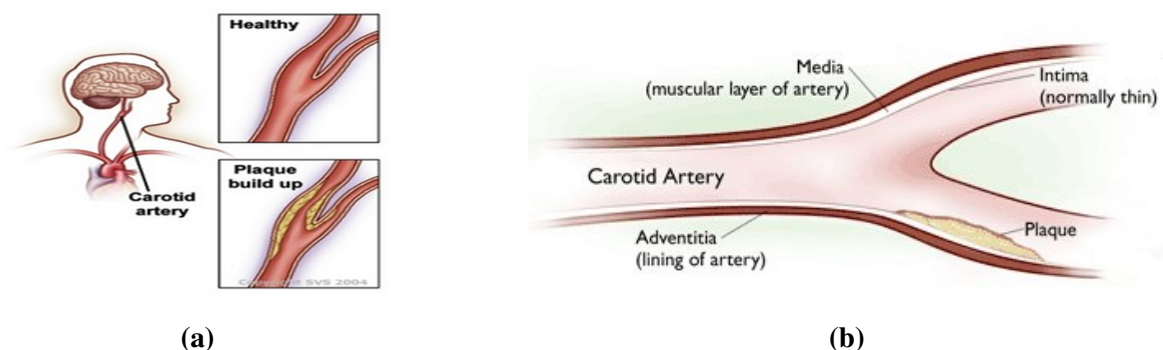
rotic plaques in the common carotid artery (CCA) (Masuda *et al.* (2013)). Atherosclerosis disease is characterised by accumulation of proteins, lipids, and cholesterol, which significantly reduces blood flow (Association *et al.* (2002)). Carotid arteries are responsible for supplying blood from heart to the brain and muscle of the face. The carotid arteries are mainly divided into two parts: right CCA and left CCA. Each of the arteries again divided into two branches: internal carotid artery (ICA) and external carotid artery (ECA), which are shown in the Figure 1.1. The ICA supplies oxygenated blood to the brain and ECA



**Figure 1.1:** Side and front view of common carotid artery (<https://wiki/Carotidartery>).

supplies oxygenated blood to the skull such as ears and nose. The risk of stroke increases with the severity of carotid stenosis (narrowing of artery caused due to accumulation of plaque). The accumulated plaque causes narrowing of the inner surface of the carotid artery which in turn results in irregularity of the artery (Mughal *et al.* (2011)). The degree of luminal narrowing is considered as an indirect measure of stenosis severity due to carotid atherosclerosis.

It is assumed that an increased plaque thickness in the carotid artery is a predictor of future cardiovascular events such as heart attack and stroke (Group (1994)). A stroke usually occurs when the blood supply to parts of the brain is suddenly blocked (i.e. Ischemic stroke) which is shown in Figure 1.2(a). The ischemic stroke caused by artery stenosis, accounts for approximately 75% of all strokes and blockage, caused by fatty build up, is referred as atherosclerosis (Christodoulou *et al.* (2003)). When a blood vessel in the brain bursts, spilling of blood occurs into the spaces surrounding brain cells and leads to haemorrhagic stroke. The degree to which the vessel is narrowed as a result of plaque growth (shown in Figure 1.2(b)), is an indirect measure used to describe the sensitivity of the atherosclerosis,

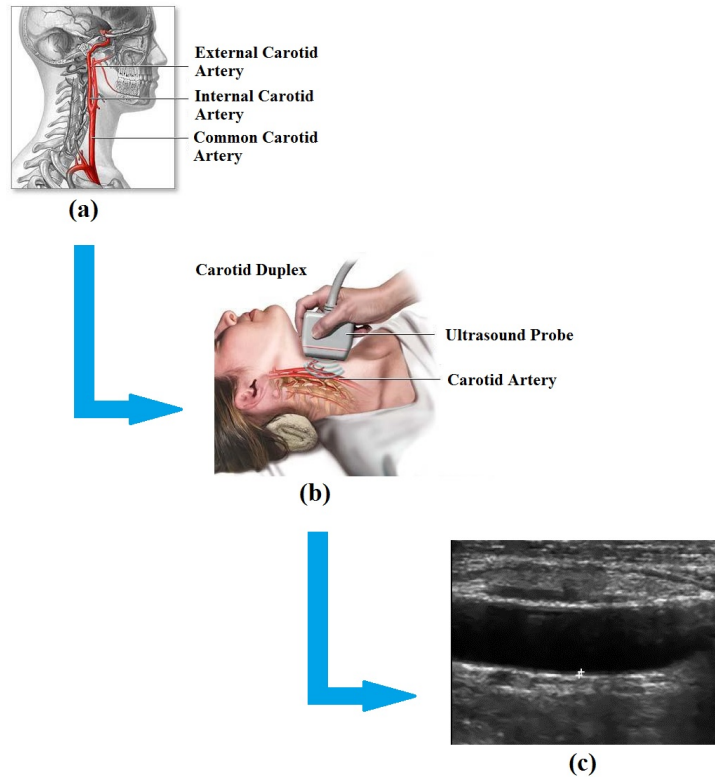


**Figure 1.2:** (a) Normal and abnormal blood flow in the common carotid artery. (b) Carotid artery with plaque (<https://www.vascularweb.org>).

where the presence of a plaque is direct indicator of the risk of stroke (Lamont *et al.* (2000)). Hence, monitoring of the changes occurring in the carotid artery via imaging technique may provide us a new clinical and practical strategy to treat patients with severe cardiovascular complications.

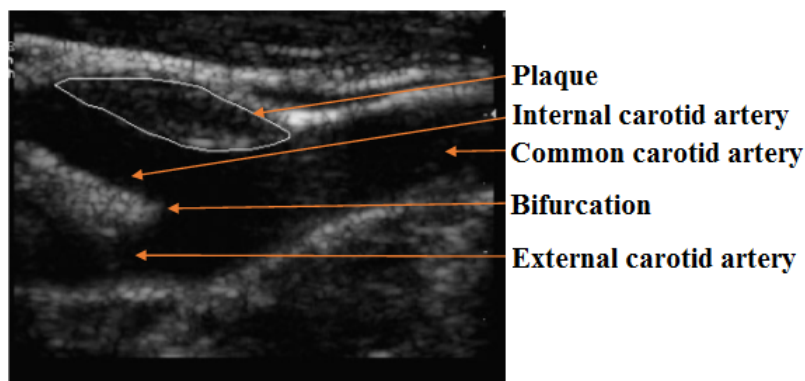
## 1.2 Brief review on Ultrasound Imaging

The ultrasound imaging is used for diagnosing cardiac and carotid diseases. Ultrasound is recognized as a simple and rapid imaging method which allows real time dynamic examination of the carotid artery. The medical ultrasound referred as an ultrasonography, uses high frequency sound waves (> 20,000 Hz) for imaging. For diagnosis and assessment of imaging organs, the ultrasound is popular because of its non invasive nature and high imaging quality. Figure 1.3 shows the diagnosis of carotid ultrasound imaging in which transducer probe is kept in to the neck for acquiring carotid B-mode images (see Figure 1.3(b)). The ultrasound transducer probe generates and receives sound waves using principle called piezoelectric effect. These sound waves propagate through soft tissue and fluids, it reflected back in the form of echoes. The echoes are detected by the transducer and displayed as 2D longitudinal carotid B-mode images (see Figure 1.3(c)). B-mode refers to the brightness mode. The B-mode ultrasound image displays the acoustic impedance of a two dimensional cross section of a tissue (Quistgaard (1997)). The intensity of the echo is represented by modulation of the brightness of the spot and the position of echo is determined from the angular position of the transducer. B-mode ultrasonography is widely used in carotid imaging because of its low cost and ability to provide real information about both lumen and vessel wall (Stein



**Figure 1.3:** Diagnosis using ultrasound imaging.(a) Common Carotid Artery.(b) Carotid duplex with ultrasound probe.(c) B-mode longitudinal image. ([http://www.biosim. ntua.gr/en](http://www.biosim.ntua.gr/en))

*et al.* (2005)). In B-mode, echoes are displayed as a 2D gray scale image. The amplitude of



**Figure 1.4:** Ultrasound B-mode longitudinal image with manually delineated plaque.

the returning echoes are represented as dots (pixel) of an image with different gray values as shown in Figure 1.4. The image is constructed by these pixels values line by line. Advances in B-mode ultrasound have resulted in improved anatomic definition, which has enabled

plaque characterization. The major drawbacks of the ultrasound imaging are; it has poor penetration through bone or air, obtained images can be difficult to interpret (Wells (2000)). However, the ultrasound imaging offers many benefits as follows; ultrasound equipment has relatively low cost as compared to other imaging devices, it allows safe and relatively quick examination of the subject.

### 1.2.1 Plaque characteristics

To validate the atherosclerosis disease, IMT measurement is used in the CCA by ultrasound imaging. The degree of the artery stenosis is defined as the percentage of the lumen diameter reduction relative to a reference vessel diameter. It is measured as the difference between the largest and smallest area of the artery in relation to the largest area and is defined by the North American Symptomatic Carotid Endarterectomy Trial (NASCET) study as (Ferguson *et al.* (1999)),

$$\text{Degree of artery stenosis} = 100 \left[ 1 - \frac{D_{ICA,min}}{D_{ICA,distal}} \right] \quad (1.1)$$

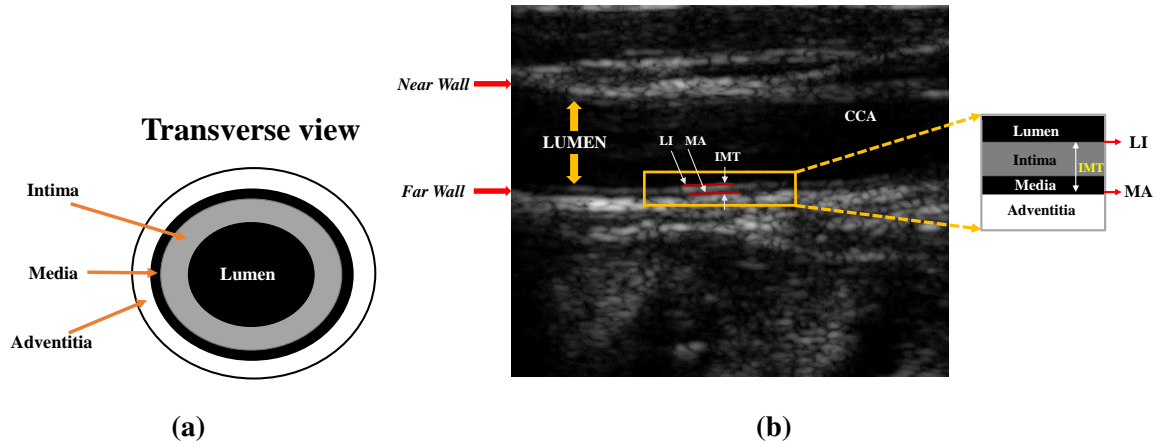
where  $D_{ICA,min}$  is the minimum lumen diameter in the ICA at the location of maximal stenosis and  $D_{ICA,distal}$  is the lumen diameter in the distal diseased free portion of the ICA. The plaque characteristics are useful in determining high risk plaques, which are more likely to cause thromboembolic events leading to stroke (Zarins *et al.* (2001)). Mainly two types of plaques are visible in the carotid artery which are homogeneous plaque and heterogeneous plaque. Homogeneous plaques are characterised by uniform high level echoes, smooth surface, echogenicity, and are associated with stable plaques. Heterogeneous plaques are associated with advance stages of carotid plaque lesion, irregular surface, and echolucency. Echogenic plaques reflect strongly the ultrasound signal, whereas echolucent plaques have less reflective ability (Ebrahim *et al.* (1999)).

### 1.2.2 IMT of the Common Carotid Artery

The carotid artery wall mainly consists of three layers, which is shown in Figure 1.5(a); **Intima**: it is the innermost layer which is composed of a layer of endothelial cells, and it is adjacent to the flowing blood and responsive to change in wall shear stress and stretching. **Media**: it is the middle layer which is composed of smooth muscle cells, elastin fibres, collagen fibres and ground substances. **Adventitia**: it is the outer layer and composed of



collagen fibres with smaller amounts of ground substance and fibroblasts.



**Figure 1.5:** Illustration of the common carotid artery in longitudinal and transverse projection.

Figure 1.5(b) illustrates a longitudinal B-mode ultrasound images of the CCA. In the longitudinal view, the CCA can be seen as a dark portion constituting the lumen, which is bound at the top by the near wall and at the bottom by the far wall (Illustrated in Figure 1.5). The intima layer is not adequately visible and is often seen with the adventitia layer owing to the poor difference in the acoustic impedance between the two adjacent interfaces. The adventitia layer normally appears as bright gray (highly echogenic), whereas the media layer appears as dark gray. The image consists of two semi-parallel traces that constitute the lumen intima (LI) and media adventitia (MA). The distance between LI and MA is called intima media thickness (IMT) which is the key marker of cardiovascular risk. Generally, the IMT measurement  $< 1\text{mm}$  are considered as normal whereas  $> 1\text{mm}$  as abnormal. The increase in IMT is linearly related to the progression of stroke, which is observed more in the elderly (Bots *et al.* (1997), Lamont *et al.* (2000)). Segmentation of the IMC in CCA is one of the most important challenges in computer aided clinical applications.

### 1.3 Motivation

The World Health Organization reported that stroke is one of the common causes of morbidity and mortality worldwide. In a recent survey (WHO (2013)), it was found that 31% of the mortality around the world is due to cardiovascular diseases. Among them, around 6.9 million people were dead owing to stroke and it accounts for some modifiable risk factors such as diabetes, alcohol consumption, smoking and hypertension etc. It is estimated that,

by 2030, over 23 million people will die from CVDs each year since most of the low to middle income countries are seriously affected by CVDs. For current lifestyle, prevention is the key to decreasing the occurrence of CVDs and thus the number of global deaths. Therefore, an early marker of the increased risk of CVD is a significant predictor for clinical diagnoses. The expert performs diagnosis of a CVD based on several factors such as medical test results, clinical history and acquisition of medical images. In certain cases, the diagnosis becomes more difficult for an expert to analyse a large amount of data in shorter time. The advancement of medical imaging techniques and computer softwares are used to aid the experts for identification and interpretation of the disease in short duration. These softwares provide an assessment of the disease using image based information alone. In fact, developing software tool for radiological image processing is one of the challenging problems in the medical domain. Since accurate diagnosis of a disease depends on both image acquisition and interpretation, modern diagnostic systems are built by incorporating the cutting edge computing and data processing technologies. Even though computer based diagnostic systems are commercially available, fully automated approaches have not yet been completely formalized in the literature. This deficiency has led to difficulty in their use for diagnostic purpose.

## **1.4 Problem Statement**

The earliest appearance of the possible attack of CVD is atherosclerosis. The atherosclerosis process affects the size and shape of the carotid wall and leads to major cause of stroke. In the past decade, a number of studies have investigated the predictive measures for carotid atherosclerosis based on different imaging techniques. Among all, ultrasound imaging technique is non-invasive and considered as a reliable technique to measure IMT for CCA. The disadvantage of the ultrasound imaging include poor quality of image due to speckle noise. Hence, the expert takes considerable effort to extract significant information about carotid wall and possible existence of plaque layers. This task requires highly skilled experts. However, manual tracing of intima media complex (IMC) generates a result that is not reproducible. Thus, computer based fully automatic detection of carotid wall leads to more effective treatment.

## 1.5 Research Objectives

The main goal of this work is to develop automated algorithms that assist in patient risk prediction in atherosclerosis subjects from ultrasound images. The objectives of this work are;

- To develop image despeckling techniques to enhance the carotid ultrasound images.
- To conduct comparative study of edge detection algorithms in the framework of despeckling carotid ultrasound images.
- To develop novel approaches for fully automatic ROI extraction of the carotid ultrasound images.
- To develop efficient algorithms for the segmentation of intima media complex (IMC) of the common carotid artery.

## 1.6 Major Contribution

This section refers the research contributions that are carried out in our research work to achieve our research objectives;

- Initially a systematic literature survey is carried out on denoising techniques and IMC segmentation for CCA.
- We propose the use of a Bayesian least square estimation algorithm for denoising the carotid ultrasound images.
- The key contribution of the thesis is to propose novel approaches for fully automatic ROI extraction of the carotid ultrasound images.
- We present automatic segmentation of IMC in carotid ultrasound images for estimation of the IMT using support vector machine.
- A fully automated threshold-based wind driven optimization technique is developed for segmentation of the CCA from longitudinal ultrasound images.
- The measurement accuracy and high computational speed are further improved by using pre-trained structured random classifier for handling curved carotid ultrasound images.

## **1.7 Organization of the Thesis**

The remaining part of thesis is organised as follows: chapter 2 presents a literature survey on despeckling filters and IMT segmentation methods for the CCA images. The survey describes various techniques for carotid wall segmentation in ultrasound images. The theoretical background of different techniques is furthermore explained.

Chapter 3 introduces a state-of-the-art denoising and enhancement techniques for carotid ultrasound images. The denoising filters are used to reduce the speckle noise, followed by an enhancement techniques are used to improve the robustness of carotid ultrasound images. Further, comparative study of edge detection algorithms is presented based on the framework of despeckling the carotid ultrasound images.

Chapter 4 describes novel approaches for automatic ROI extraction using morphological functions and edge detection methods. Further, proposed methods based on support vector machine, threshold based wind driven optimization and structured random forest algorithms are applied to the extracted ROI for segmentation of IMC of the CCA. Later, experimental results are presented and compared with the results obtained using state-of-the-art algorithms.

Finally, chapter 5 concludes with the brief discussion on the findings of this work along with the future work suggestions.



## Chapter 2

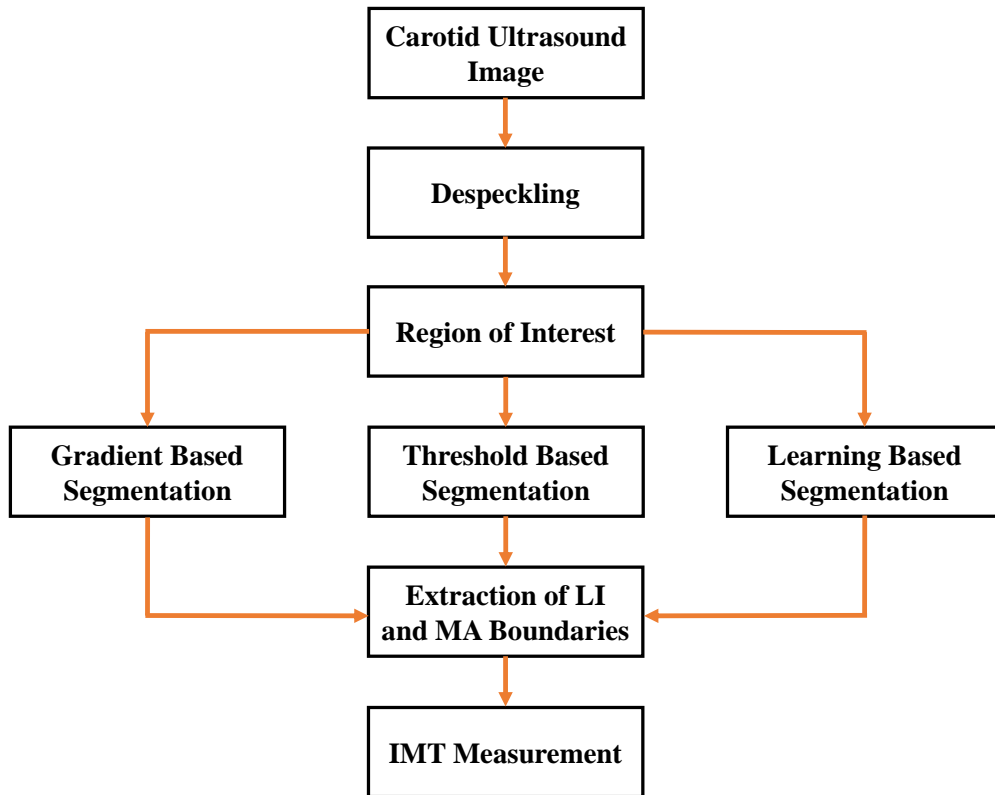
# COMMON CAROTID ARTERY SEGMENTATION APPROACHES

In this chapter, the theoretical background of despeckling filters and carotid artery segmentation methods for carotid ultrasound images are presented. Section 2.1 presents the general framework for carotid wall segmentation approaches, in which, we discuss the despeckling filters, ROI extraction methods and different types of segmentation approaches which are used for quantifying the IMT. The challenges during carotid wall segmentation are explored in the Section 2.2. Finally, A few important evaluation metrics for evaluating the despeckling and segmentation methods are presented in section 2.3.

### 2.1 General frame work for carotid wall segmentation

The IMT of CCA measured from B-mode ultrasound images can be considered as a surrogate marker for risk of CVDs. The carotid ultrasound images allow for easy visualization and quantification of anatomical structures. The ultrasound images can be acquired in real time, thus providing instantaneous visual guidance for many interventional procedures. A large number of image segmentation studies have used high resolution ultrasonography to investigate the determinants of atherosclerosis disease, because of its ability to identify atherosclerosis lesions at all stages of developments. Usually, delineation of the CCA is performed manually by medical experts using calipers (Nicolaidis *et al.* (2003)), but it was shown that this process is tedious, prone to error and has large observer variability. To address this issue, semi or fully automated ROI extraction, gradient-based segmentation, threshold-based segmentation, and learning-based segmentation algorithms for the mea-

surement of IMT in ultrasound images have been introduced. However, automated methods are required for accurate and reliable delineation of the CCA from ultrasound images. Figure 2.1 shows the general flow diagram for segmentation of IMT of the CCA. Each block in this flow diagram is explained below in detail;



**Figure 2.1:** General flow diagram for segmentation of IMT of the CCA.

### 2.1.1 Despeckling filters

The pre-processing stage helps in improving the quality of image in ways that increase the accuracy of segmentation. Speckle noise and artefacts cause image degradation in several ultrasound image modalities. Different image modalities exhibit distinct types of degradation. Image degradation can have a significant impact on image quality and thus affect human interpretation and the accuracy of computer-assisted methods. Poor image quality often makes feature extraction, analysis, recognition, and quantitative measurements problematic and unreliable. In literature, several methods have been developed for reducing the speckle noise in the ultrasound image (Solbo and Eltoft (2004)). The overview of despeck-

ling filters are tabulated in the Table.2.1. In a carotid ultrasound image, speckle noise is a multiplicative noise that degrades the image quality by concealing the fine structures. Using Gaussian filters, the amount of smoothing is usually controlled by the standard deviation ( $\sigma$ ), which must be large enough to reduce the noise. However, if the  $\sigma$  is too large, the CCA walls may be completely blurred.

### **2.1.2 Region of Interest (ROI)**

Usually, ROI extraction involves edge detection from an image. Commonly, the far wall of the CCA is considered as the reference boundary for cropping the ROI. Hence, once the ROI is extracted, we have limited search area for the measurement of IMT. Since, the lumen region can be considered as the dark region that is located between the two bright adventitia layers of the CCA, this might be the best approximation for the ROI. In the most of the literature, pre-processing stage is done prior to the ROI selection. This is to increase the effectiveness of the segmentation algorithm and to avoid false measurement of IMT. Segmentation is the next step after ROI extraction. In the literature, several algorithms involving the use of gradient-based segmentation, threshold-based segmentation, and learning-based segmentation techniques have been presented for segmenting the IMC of the carotid ultrasound images. The overview of ultrasound IMT segmentation techniques is tabulated in the Table 2.2. Further, the advantages and limitations of the segmentation algorithms are listed in Table 2.3. Each of the segmentation techniques is explained below.

### **2.1.3 Gradient-based Segmentation**

In the past two decades, several algorithms have been presented to segment the IMC in ultrasound images. The dynamic programming has been introduced for the automatic identification of echo interfaces, which are used for measuring the boundary continuity, intensity of echo, and gradient (Wendelhag *et al.* (1997)). Li *et al.* (2014) presented the improved and efficient measurement of the IMT of CCA by adjusting the LI and MA boundaries using the dynamic programming technique. Faita *et al.* (2008) presented a maximum-gradient technique for detecting the relative variation of the gray levels in an image. Rafati *et al.* (2015) introduced the combination of the dynamic programming and maximum-gradient methods for detecting instantaneous changes in the distribution of the IMT in the carotid ultrasound images. The Hough transform was introduced for determining the dominant lines and circles corresponding to the LI and MA interfaces in the longitudinal carotid ul-



**Table 2.1:** Overview of despeckle filtering Techniques

| <b>Author</b>             | <b>Speckle Reduction methods</b>                      | <b>Description</b>   |
|---------------------------|---|--|
| Frost et al. (1982)       | Frost filter  | It is based on the coefficient of variation of the adaptive averaging filter, which is the ratio of local standard deviation to local mean of the degraded image.  |
| Lee (1986)                | Lee filter  | It performs noise filtering using first order local statistics from the neighborhood of a specified pixel and it smooths the area having lower variances.  |
| Kuan et al. (1987)        | Kuan filter   | It is a local linear minimum square error filter based on multiplicative model.  |
| Hu and Hu (1994)          | Median filter   | It removes the spike value by replacing the middle pixel value with the median value of neighborhood window.   |
| Yu and Acton (2002)       | Speckle Reduction Anisotropic Diffusion (SRAD) filter | It is used for preserving the edges by suppressing the speckle noise.  |
| (Pižurica et al. (2003))  | Wavelet based filter                                  | It is a multi resolution decomposition based on wavelet coefficients, which exploits the correlation of significant feature of the image.  |
| Vese and Osher (2003)     | Total Variation                                       | It is effective for preserving the edges and smooths in the flat regions.  |
| Buades et al. (2005)      | Non Local Mean (NLM) filter                           | It performs nonlocal averaging of all pixels in the image. The pixels in the image are highly correlated and noise is identically distributed then averaging of these pixels results a noise suppression thereby yields a pixel similar to original value. |
| (Coupé et al. (2009))     | Optimised Bayesian Non Local Mean (OBNLM) filter      | It is an adaptation of non-local mean filter and amount of image smoothing is determined directly by noise variance.   |
| Chao and Tsai (2010)      | Detail Preserving Anisotropic Diffusion (DPAD) filter | It simultaneously preserves fine details and edges while noise filtering in the diffusion process.   |
| Zhang et al. (2015)       | Wavelet based bilateral filter                        | For the noise free signal, the wavelet coefficients are modeled as generalized Laplace distribution and speckle noise takes the form of Gaussian distribution.   |
| Li et al. (2016b)         | Curvelet based orientation selective filter           | It processes the curvelet coefficients by orientations unlike the conventional methods based on curvelet transform which considers only magnitude.   |
| Sagheer and George (2017) | Noise reduction based on low rank approximation       | The low rank approximation is used to reduce the speckle noise based on weighted nuclear norm minimization.  |
| Farouj et al. (2017)      | Hyperbolic wavelet Fisz transformation                | This method computes the hyperbolic wavelet transform of the image, before applying a multi scale variance stabilization technique based on Fisz transformation  |

trasound images (Golemati *et al.* (2007) Golemati *et al.* (2004)). Loizou *et al.* introduced the snake energy function for segmenting the IMT of CCA by integrating the internal and external forces (Loizou *et al.* (2007), Loizou *et al.* (2009), Loizou *et al.* (2013), Loizou *et al.* (2015)). The majority of the active contour algorithm adopted the traditional formulation of the snake as presented by Williams and Shah (1992). The combination of the dynamic programming and geometric snakes methods is used for the segmentation of the IMC in the carotid wall (Rocha *et al.* (2010)). Molinari *et al.* proposed the use of automatic multi-resolution edge snapper for the quantification of the IMT of CCA (Molinari *et al.* (2012)). The frequency-domain-based active contours have been proposed for providing soft final contours, which are computationally faster than other contour methods (Bastida-Jumilla *et al.* (2015)). The ROI is composed of plaque, the vessel lumen, and adventitia of the artery wall in carotid ultrasound images modelled by mixture of Nakagami distributions, which yielded the likelihood of a Bayesian segmentation model (Destrempe *et al.* (2009)). The model-based approach has been used for the automated segmentation of the IMC, and it deals with the irregularity in presence of the IMC over the cardiac cycle (Ilea *et al.* (2009), Ilea *et al.* (2013a)).

#### **2.1.4 Threshold-based Segmentation**

The edge based techniques make use of function values and derivatives (Yang (2014)) but do not perform effectively for smooth unimodal problems. In addition, the edge based methods show poor performance due to inconsistencies in the function values. Hence, the non-gradient-based algorithms are preferred because they depend only on function values not the derivatives. The non-gradient techniques include mainly the thresholding methods which are used for segmentation of images (Akay (2013)). Essentially, thresholding utilizes distribution of gray levels to distinguish object from image background. Both the bi-level and multi-level thresholding techniques require an optimum threshold value to segment the object of interest from their background (Huang and Wang (2009)). Threshold-based segmentation is the simplest method of image segmentation and is an effective method for partitioning the foreground and background regions. The objective function presented for the threshold-based segmentation in the literature was a non-convex optimization problem. The use of gradient-based methods might result in a local minimum or a local maximum. Hence, nongradient-based methods, such as particle swarm optimization (Eberhart and Kennedy (1995)), cuckoo search (Yang (2014)), and wind driven optimization (Bayraktar *et al.* (2013)) are preferred for solving the objective function. Li *et al.* proposed an

ant colony method combined with Otsu thresholding for the segmentation of IMT, and the snake model is employed for smoothing the boundaries (Li *et al.* (2016a)).

**Table 2.2:** Overview of ultrasound IMT segmentation techniques

| <b>Author</b>                | <b>IMT segmentation Techniques</b>                  | <b>Still/Video</b> | <b>Patients/Images</b> | <b>IMT<sub>mean</sub> mm</b> | <b>Processing time</b> |
|------------------------------|---|--------------------|------------------------|------------------------------|------------------------|
| Cohen (1991)                 | Balloon snake segmentation                          | Still              | 3 Patients             | -                            | -                      |
| Gustavsson et al. (1997)     | Dynamic programming                                 | Still              | 1 Patients             | -                            | -                      |
| Wendelhag et al. (1997)      | Dynamic programming with cost function optimization | Still              | 50 Patients            | 0.92                         | -                      |
| Mojsilović et al. (1997)     | Texture based approach                              | Still              | 29 Patients            | 0.68                         | -                      |
| Sonka and Fitzpatrick (2000) | Optical graph searching                             | Still              | 1 Patients             | -                            | -                      |
| Abolmaesumi et al. (2000)    | Star Kalman filter                                  | Still              | -                      | -                            | -                      |
| Liang et al. (2000)          | Multiscale dynamic programming                      | Still              | 50 Images              | 0.92                         | 42sec                  |
| Mao et al. (2000)            | Discrete dynamic contour                            | Still              | 7 Patients             | -                            | -                      |
| Ladak et al. (2001)          | Discrete dynamic Contour                            | Video              | 4 Patients             | 0.75                         | -                      |
| Liguori et al. (2001)        | Pattern recognition and edge detection              | Still              | 30 Images              | -                            | -                      |
| Selzer et al. (2001)         | Dynamic edge detection segmentation                 | Video              | 24 Patients            | 0.78                         | 15sec                  |
| Xiao et al. (2002)           | Morphology operators                                | Still              | 2 Patients             | -                            | -                      |
| Cheng et al. (2002)          | Snakes based segmentation                           | Still              | 32 Patients            | 0.65                         | -                      |
| Gutierrez et al. (2002)      | Multiresolution active contours                     | Still              | 30 Patients            | 0.72                         | 31sec                  |

|                         |  |       |             |      |         |
|-------------------------|--|-------|-------------|------|---------|
| Stein et al. (2005)     | Gradient based approach                                | Still | 50 Patients | 0.67 | -       |
| Faita et al. (2008)     | First order absolute moment edge detector              | Still | 42 Patients | 0.56 | -       |
| Golemati et al. (2007)  | Hough Transform  | Still | 10 Patients | 0.61 | -       |
| Delsanto et al. (2007)  | Fuzzy C means and snakes                               | Still | 120 Images  | 0.71 | -       |
| Ilea et al. (2009)      | Spatially continuous vascular model                    | Still | 49 Images   | -    | 8sec    |
| Destrempe et al. (2009) | Mixture of Nakagami distribution                       | Video | 30 Images   | 0.81 | 24sec   |
| Loizou et al. (2009)    | Snake based segmentation                               | Still | 100 Images  | 0.68 | 27sec   |
| Freire et al. (2009)    | Gradient based approach                                | Still | 43 Patients | 0.53 | 2.52sec |
| Rocha et al. (2010)     | Hybrid dynamic programming based active contour        | Still | 24 Patients | -    | -       |
| Molinari et al. (2010b) | Integrated approach using fuzzy K means classification | Still | 200 Images  | -    | -       |
| Molinari et al. (2012)  | Multi resolution edge detection segmentation           | Still | 365 Images  | 0.91 | 15sec   |
| Ilea et al. (2013a)     | Adaptive Normalized Correlation                        | Video | 40Sequences | 0.60 | 80sec   |
| Loizou et al. (2013)    | Snake segmentation                                     | Still | 20 Patients | 0.93 | 28sec   |
| Li et al. (2014)        | Dynamic programming                                    | Still | 100 images  | -    | -       |
| Rafati et al. (2015)    | Maximum gradient and Dynamic programming               | Video | 30 Patients | 0.57 | -       |
| Loizou et al. (2015)    | Snake segmentation                                     | Still | 300 Images  | -    | 35sec   |

|                   |                         |       |            |   |   |
|-------------------|-------------------------|-------|------------|---|---|
| Li et al. (2016a) | Ant colony optimization | Still | 224 Images | - | - |
|-------------------|-------------------------|-------|------------|---|---|

### 2.1.5 Learning-based Segmentation

Recently, fast edge detection using a learning-based classifier has been receiving increasing attention. In the past few years, several methods have been implemented using a learning-based technique for the detection of edges (Mairal *et al.* (2008)). The boosted classifier is used to label each pixel independently based on its neighbourhood image patch as an input (Dollar *et al.* (2006a)). Arbelaez *et al.* (2011) improved this result by computing the gradient across the learned sparse codes of the patch gradients (Xiaofeng and Bo (2012)). Zheng *et al.* (2010) proposed the use of a learning-based approach for the detection of object boundaries and demonstrated results of specific object detection. Lim et al. proposed the use of sketch tokens using supervised mid-level information for edge detection in the form of hand-labeled images (Lim *et al.* (2013)). A robust spatial c-means method has been proposed by Hassan et al. for the segmentation of the IMT in carotid ultrasound images based on the information gain (Hassan *et al.* (2014) Hassan *et al.* (2012)). Menchón-Lara *et al.* (2014) used the neural network algorithm for performing a binary classification for estimating the IMC contours based on multi-layer perceptrons. Araki et al. proposed the use of a stroke risk stratification using ultrasonic echolucent carotid plaque morphology based on machine learning (Araki *et al.* (2017)).

**Table 2.3:** Advantages and limitation of carotid wall segmentation methods

| Author   | Segmentation Techniques                          | Advantages  | Limitations  |
|--|--|---|--|
| Pignoli and Longo (1987), Touboul <i>et al.</i> (1992), Liguori <i>et al.</i> (2001), Stein <i>et al.</i> (2005), Faita <i>et al.</i> (2008) | Edge detection and gradient based method         | <ul style="list-style-type: none"> <li>• Suited for real time implementation.</li> <li>• Operator can have immediate feedback on the quality of the image.</li> </ul> | <ul style="list-style-type: none"> <li>• Lack of automation.</li> <li>• No robustness with noise.</li> </ul>   |
| Wendelhag <i>et al.</i> (1997), Liang <i>et al.</i> (2000), Liu (2008), Holdfeldt <i>et al.</i> (2008), Cheng <i>et al.</i> (2002)           | Dynamic Programming based on multiscale analysis | <ul style="list-style-type: none"> <li>• Fully Automated.</li> <li>• Low computation complexity.</li> <li>• Suitable for clinical purposes.</li> </ul>                | <ul style="list-style-type: none"> <li>• Initial human setting and training required.</li> <li>• Fails for slanting IMC with weak boundaries.</li> </ul> |

|   |   |   |  |
|---|---|---|--|
| Golemati <i>et al.</i> (2007)<br>Stoitsis <i>et al.</i> (2008),<br>Xu <i>et al.</i> (2012)<br>Petroudi <i>et al.</i> (2010)<br>Matsakou <i>et al.</i> (2011)  | Segmentation based on Hough Transform   | <ul style="list-style-type: none"> <li>• It is less likely to be effected by noise.</li> <li>• Compensate the holes or missing boundaries.</li> </ul> | <ul style="list-style-type: none"> <li>• The method work fine for early thickening of IMC but fails for irregular boundaries in the presence of plaques and eliminates minor details.</li> </ul> |
| Williams and Shah (1992), Cheng <i>et al.</i> (2002), Delsanto <i>et al.</i> (2007), Molinari <i>et al.</i> (2010a), Loizou <i>et al.</i> (2007), Loizou <i>et al.</i> (2013), Loizou (2014), Loizou <i>et al.</i> (2015) | Active contours (Snake ) based segmentation   | <ul style="list-style-type: none"> <li>• It works well for noisy images</li> <li>• doesn't require any user interaction</li> </ul>                    | <ul style="list-style-type: none"> <li>• Dependence on the initialization of the snake points.</li> <li>• Need for optimization of the parameter</li> <li>• Sensitivity to noise</li> </ul>      |
| Destrempes <i>et al.</i> (2009)   | Segmentation based on mixture of nakagami distributions and Stochastic Optimization | <ul style="list-style-type: none"> <li>• Lowest tracing error for LI and MA.</li> <li>• Method is not sensitive to the degree of stenosis.</li> </ul> | <ul style="list-style-type: none"> <li>• Method suitable for healthy arteries.</li> <li>• Extensive tuning and training so computational cost is high.</li> </ul>                                |
| Ilea <i>et al.</i> (2013a), Kanber <i>et al.</i> (2013) , Destrempes <i>et al.</i> (2009)   | Model based, Adaptive Normalised Correlation algorithm, Block Matching.             | <ul style="list-style-type: none"> <li>• Robust to the estimation procedure..</li> </ul>  | <ul style="list-style-type: none"> <li>• Computation time is high.</li> </ul>  |
| Li <i>et al.</i> (2016b)  | Ant colony optimization technique   | <ul style="list-style-type: none"> <li>• Can estimate the missing LI interface boundaries.</li> </ul>   | <ul style="list-style-type: none"> <li>• This method is intended for segmenting nearly parallel boundaries, which may limit its use for plaque.</li> </ul>                                       |

## 2.2 Challenges during Segmentation

The segmentation of IMC of the CCA is a challenging process, whereas developing a fully automated system is even harder in practice. One must take advantage of the knowledge in ultrasound image reconstruction in the segmentation process. The images may have scanned with different hardware settings (frequency, depth, gain etc.) and different positioning of the probe. The challenges for segmentation vary with quality of image data and view due to the anisotropy of ultrasound image acquisition. There are several challenges for the automated carotid wall segmentation from ultrasound images. The shape and size of the carotid artery, presence of plaque and curvature in arteries make the segmentation process harder (Nicolaidis *et al.* (2003)). Characteristics of artefacts such as attenuation, speckle noise, acoustic shadowing and signal drop-out may complicate the segmentation task (Golemati *et al.* (2007)). Sensitivity to ultrasound vibrations at each depth of the body

is different due to which the imaging suffer from signal loss. In the ultrasound image, attenuation is the amplitude of ultrasound beam as a function of distance through the imaging medium. Accounting for the attenuation effects in ultrasound is important as reduced signal amplitude can affect the quality of image produced. Acoustic shadowing in an ultrasound image is characterised by a signal void behind structures that strongly absorb or reflect ultrasonic waves. This happens most frequently with solid structures, as sound conducts most rapidly in areas where molecules are closely packed, as in bone or stones. The direct effect of acoustic shadowing or echo attenuations in the segmentation task is that some boundary segments may be missing which may lead to edge leaking at the far LI interfaces. The major issue related to the segmentation is poor visibility of the carotid ultrasound image owing to the patient variation with respect to the structure and mechanical properties of the arterial wall, speckle noise and irregularity associated with the LI and MA boundaries caused by variation of the ultrasound probe during the image acquisition. To address these problems which are common in the analysis of CCA ultrasound data, we propose novel segmentation approaches for quantification of IMT in longitudinal ultrasound images.

## 2.3 Performance metrics for despeckling and IMT measurement

### 2.3.1 Performance metrics for despeckling filters

The performance metrics for a carotid ultrasound image of size  $R \times C$  are defined as follows:

- **Signal to noise ratio (SNR)**

SNR is the ratio between signal power to noise power and is expressed as (Srivastava *et al.* (2010)) ,

$$SNR = 10 \log_{10} \left( \frac{\sigma_s^2}{\sigma_n^2} \right), \quad (2.1)$$

where  $\sigma_s^2$  is the signal variance and  $\sigma_n^2$  is the noise variance of the image.

- **Peak signal to noise ratio (PSNR)**

PSNR is computed as the ratio of maximum power of signal to the noise level and is

described as (Srivastava *et al.* (2010)) ,

$$PSNR = 10 \log_{10} \left( \frac{255}{\sqrt{MSE}} \right), \quad (2.2)$$

where  $MSE = \frac{1}{RC} \sum_{i=1}^R \sum_{j=1}^C (U_{i,j} - U'_{i,j})^2$  is the mean square error.

- **Root mean square error (RMSE)**

RMSE is used to measure the differences between original value and the filtered value, and is defined as the square root of mean square error (Srivastava *et al.* (2010)),

$$RMSE = \sqrt{\frac{1}{RC} \sum_{i=1}^R \sum_{j=1}^C (U_{i,j} - U'_{i,j})^2}, \quad (2.3)$$

where  $U_{i,j}$  is the original image without speckle noise and  $U'_{i,j}$  is the filtered image of size  $R \times C$ .

- **Structure similarity map (SSIM)**

SSIM are mainly used to compare contrast, luminance and structure of two different images. The SSIM value must be closer to unity for optimal measure of similarity and is expressed as (Srivastava *et al.* (2010)) ,

$$SSIM(U, U') = \frac{(2\mu_U \mu_{U'} + k_1)(2\sigma_{UU'}) + k_2}{(\mu_U^2 + \mu_{U'}^2 + k_1)(\sigma_U^2 + \sigma_{U'}^2 + k_2)}, \quad (2.4)$$

where  $\mu_U$  is the mean intensity of original image,  $\mu_{U'}$  is the mean intensity of filtered image,  $\sigma_U^2$  is variance of the original image,  $\sigma_{U'}^2$  is variance of the filtered image,  $k_i$  ( $i=1$  or  $2$ ) is the constant to avoid instability when  $\mu_U^2 + \mu_{U'}^2$  is very close to zero and is defined as  $k_i = (c_i \cdot L^2)$  in which  $c_i < 1$  (By default,  $c_1=0.01$  and  $c_2=0.03$ ) and  $L$  is the dynamic range of pixel values.  $\mu_U \mu_{U'}$  is covariance of the original image and filtered image.

- **Coefficient of correlation (CoC)**

CoC measures the edge preservation in the denoised image and it has the value between 0 and 1 for uncorrelated and identical images respectively. The CoC is defined as (Sivakumar *et al.* (2010)) ,



$$CoC = \frac{\sum_{i=1}^R \sum_{j=1}^C (U'_{i,j} - \bar{U}'_{i,j})(U_{i,j} - \bar{U}_{i,j})}{\sqrt{\sum_{i=1}^R \sum_{j=1}^C (U'_{i,j} - \bar{U}'_{i,j})^2 \sum_{i=1}^R \sum_{j=1}^C (U_{i,j} - \bar{U}_{i,j})^2}} \quad (2.5)$$

where  $U_{i,j}$  is the original image without speckle noise and  $U'_{i,j}$  is the filtered image of size  $R \times C$ .

- **Image quality index (IQI)**

IQI measures the degree of distortion in terms of loss of correlation, variance distortion and mean distortion. The dynamic range of IQI lies between -1 to 1 and IQI is expressed as (Wang *et al.* (2004)),

$$IQI = \frac{4\sigma_{UU'} \cdot \overline{UU'}}{[\sigma_U^2 + \sigma_{U'}^2][\overline{U^2} + \overline{U'^2}]} \quad (2.6)$$

where  $U_{i,j}$  is the original image without speckle noise and  $U'_{i,j}$  is the filtered image,  $\sigma_U^2$  is variance of the original image, and  $\sigma_{U'}^2$  is variance of the filtered image.

### 2.3.2 Validation metrics for IMT measurement

An automated carotid artery segmentation system can be evaluated in two ways. They include simple visual inspection and computer aided measurement. However, computer measurements are used to analyse the system quantitatively using metrics and compared against the manual expert tracings which are considered as ground truth (GT). Further, it is mandatory for an automated medical system to compare and validate against manual tracings in order to be accepted in the clinical domain. Different evaluation metrics are used for evaluating the performance of carotid artery segmentation algorithms. The following are some popular performance metrics found in the literature.;

- **Mean Absolute Distance (MAD) metric:**

The IMC lies horizontally in the carotid ultrasound images. The detected boundaries of the LI and MA interfaces of the IMC have same number of points. The IMT is estimated by measuring the MAD between the detected LI and the MA boundaries and it is defined as (Molinari *et al.* (2010b)):

$$IMT_{mean} = \frac{1}{N} \sum_{u=1}^N |MA_u - LI_u| \quad (2.7)$$

where,  $N$  represents the number of points present in the LI and MA boundaries. The variable  $u$  represents the index spanning the columns of image. The minimum and maximum values of  $|MA_u - LI_u|$ , for  $1 < u < N$  can be used to check whether the detected IMT is reasonable. Generally, this evaluation metric is more effective when the artery wall is straight and horizontal in the image. In our experiments, MAD evaluation metrics is used (as in Eq.(2.7)) to estimate the IMT as most of the ultrasound images in our database have horizontal carotid wall boundaries.

• **Polyline Distance (PD) Metric:**

PD metric is used to measure the IMT mean of the CCA. It measures the changes of the contours of the LI and MA interfaces. The first contour used is the LI interface and denoted by  $B_1$ . A point on the first contour  $B_1$  is chosen as the reference point  $(x_0, y_0)$ . The nearest point at the second contour (MA interface),  $B_2$  was found using the Euclidean distance. This is the 1<sup>st</sup> point  $(x_1, y_1)$  to be evaluated and the 2<sup>nd</sup> point  $(x_2, y_2)$  is established as the point next to the 1<sup>st</sup> point on the second contour. The two points actually form a line segment  $l$ . The distance  $d(v, l)$  was obtained which is the distance between the reference point,  $v(x_0, y_0)$  and the line segment formed by the 1<sup>st</sup> point and 2<sup>nd</sup> point.

The distance between the 1<sup>st</sup> point to the reference point is called  $d_1$  whereas the 2<sup>nd</sup> point to the reference point is called  $d_2$ . Another term used in the process towards finding  $d(v, s)$  is  $\lambda$  which is the distance along the vector of the segment  $s$ . The perpendicular distance between the line segment and the reference point  $v$ , is given by  $d^\perp$ . The formulas to calculate  $\lambda$  and  $d^\perp$  are given below (Molinari *et al.* (2010b));

$$\lambda = \frac{(y_2 - y_1)(y_0 - y_1) + (x_2 - x_1)(x_0 - x_1)}{(x_2 - x_1)^2 + (y_2 - y_1)^2}$$

$$d^\perp = \frac{(y_2 - y_1)(y_0 - y_1) + (x_2 - x_1)(x_0 - x_1)}{\sqrt{(x_2 - x_1)^2 + (y_2 - y_1)^2}}$$

Therefore,  $d(v, s)$  is obtained using the following equation (Molinari *et al.* (2010b));

$$d(v, s) = \begin{cases} \min(d_1, d_2), & \lambda < 0 \text{ or } \lambda > 1 \\ |d^\perp|, & 0 \leq \lambda \leq 1 \end{cases}$$

The process to obtain  $d(v, s)$  is repeated for the rest of the contour  $B_1$  and is given by:

$$d(B_1, B_2) = \sum_{i=1}^n d(v_i, S_{B_2}),$$

where  $n$  is the number of points in contour  $B_1$  and  $S_{B_2}$  is the segment on contour  $B_2$ . Secondly, the algorithm above is repeated, where  $B_2$  now becomes the reference contour and  $B_1$  becomes the segment contour  $S_{B_1}$ . The reverse can be represented by  $d(B_2, B_1)$ . Lastly, combining both  $d(B_1, B_2)$  and  $d(B_2, B_1)$  will yield the equation below which is the PD metric (Zahalka and Fenster (2001));

$$D_s(B_1 : B_2) = \frac{d(B_1, B_2) + d(B_2, B_1)}{(\#vertices \in B_1 + \#vertices \in B_2)} \quad (2.8)$$

- **Correlation coefficient ( $R$ ):**

The correlation coefficient  $R$  for two sets of IMT values is given by the expression (Garren (1998)):

$$R = \frac{\sum_{k=1}^s (AS(k) - as_{mean})(GT(k) - gt_{mean})}{\sqrt{(AS(k) - as_{mean})^2} \sqrt{(GT(k) - gt_{mean})^2}}, \quad (2.9)$$

where  $s$  is the number of data pairs for the IMT measurement,  $AS(k)$  and  $GT(k)$  are the automated and the ground truth IMT values for the  $k^{th}$  case, respectively; and  $as_{mean}$  and  $gt_{mean}$  are the mean IMT values of the two sets respectively.

- **Co-efficient of Variation(CV):**

The co-efficient of variation(CV) can be estimated from the expression as (Huang *et al.* (2004)):

$$CV = \frac{IOE}{IMT_{mean}} \times 100, \quad (2.10)$$

where, inter observer error(IOE) with standard deviation was calculated for each image measurement as (Delsanto *et al.* (2007)):

$$IOE = \frac{\sigma_{IMT}}{\sqrt{2}} \quad (2.11)$$

## 2.4 Summary

We have presented recent literature on different methods for despeckling and segmentation of CCA of ultrasound images. The general framework for the segmentation of IMC of the CCA has been presented and the various challenges during segmentation have been discussed. A few important evaluation metrics are shortlisted from the literature and used for assessing the performance of despeckling filters and segmentation techniques. The global trend is now towards the complete automation of the segmentation and measurement pro-

cess, which can assist the clinician. The use of computer aided measurement techniques has potential benefit of increased accuracy with less computational complexity and less subjectivity. However, more validation studies will be required to establish the state-of-the-art on performance of the segmentation.



## **Chapter 3**

# **DENOISING AND EDGE DETECTION OF COMMON CAROTID ARTERY IMAGES**

CCA ultrasound with estimation of IMT is a safe and non-invasive technique for prediction of cardiovascular risks. Precise quantification of IMT is useful for evaluating the risk of cardiovascular disease. The presence of speckle noise in carotid ultrasound image reduces the quality of image and automatic human interpretation. Carotid ultrasound images have multiplicative speckle noise and it is difficult to reduce as compared to the additive noises. The speckle removal filters have a greater restriction in edges and characteristics preservation. This chapter starts with a related work on despeckling filters and edge detection techniques. In Section 3.2, we propose the use of Bayesian least square estimation (BLSE) filter for despeckling carotid ultrasound images in logarithmic space based on conditional posterior sampling approach. The proposed algorithm is tested with 50 B-mode carotid ultrasound images and compared with the state-of-the-art despeckling filters. Further, the work is extended with automatic ROI extraction of despeckled carotid ultrasound images. Later, edge detection techniques are applied to the extracted ROI of despeckled image. The results of the extracted edges of the ROI are compared with the result of original image, which is discussed in Section 3.3.

### 3.1 Related work on despeckling filters and edge detection methods

The IMT of carotid arteries is a significant index of the presence of atherosclerosis (Baldassarre *et al.* (2000)). Precise quantification of the IMT is useful for assessing the risk of stroke and its progress (Molinari *et al.* (2010b)). To accomplish the best possible diagnosis, the carotid ultrasound images required to be free of noise and artefacts. The measurement of IMT in the carotid wall is complex because of speckle noise in the carotid ultrasound images, the contrast of the image is reduced (Kang *et al.* (2016)). To address this problem, several enhancements and speckle denoising methods have been proposed in carotid ultrasound images. Hassan et.al used a sigmoid function in spatial domain for the process of image contrast enhancement (Hassan1&2 and Akamatsu (2009)). Zuo et.al introduced a spatially weighted histogram equalization for enhancement of contrast in the image (Zuo *et al.* (2014)). An NLM based approach for speckle reduction was introduced by Coupé *et al.* (2009) which called Optimal Bayesian NLM. This exploits the data redundancy in the image and smooths the image very well. Pandit et.al uses Lee filter which performs smoothing only in lower variance regions (Pandit *et al.* (2014)). Li and Zhang proposed SRAD filter to utilize the instantaneous coefficient of variation, which is the function of Laplacian operators and local gradient magnitude Li and Zhang (2017). The noise and edges represent high frequency component in an image; hence, detection of the edge is very difficult in noisy images. The noisy images use operators in larger scope to average enough data to localize noisy pixels. Generally, the edge is detected using algorithms such as Canny, Sobel, Prewitt, Robert and LoG operators (Maini and Aggarwal (2009)). Canny operator (Canny (1986)) smooths the data by means of Gaussian convolution and then performs the edge detection operation. Sobel operator is used to find the approximate absolute gradient magnitude at each point in an input grayscale image (Muthukrishnan and Radha (2011)). Prewitt operator (Haider *et al.* (2012)) is a desirable approach for estimating the magnitude and orientation of an edge in an image. Robert operator (Heath *et al.* (1996)) performs a simple calculation of spatial gradients and is used for grayscale images. LoG operator (Srivastava *et al.* (2010)) is used for an image to highlight the regions of abrupt change in the intensity value. The objective of this work is to compare different edge detection techniques with different denoising filter in carotid ultrasound images for optimal reduction of speckle noise and detail preservation of edges. The proposed framework presents speckle reduction using BLSE method and Canny operators to preserve the edges in carotid ultrasound

images.

### 3.2 Proposed Methodology for despeckling using BLSE

A granular noise called speckle noise exists in ultrasound images, which is signal dependent. The major reason for the speckle is constructive or destructive interference of ultrasound waves which produce the light and dark pixels in the image. Speckle degrades the image quality and reduces the contrast which affects the texture based analysis and segmentation. The presence of speckle noise in carotid ultrasound images adversely affect the individual interpretation and diagnosis. Carotid ultrasound images have multiplicative speckle noise which reduces the ability of the manual observer (Kaur *et al.* (2011)). The multiplicative speckle noise is expressed as:

$$m(s) = g(s) * k(s) \quad (3.1)$$

where  $s$  represents the spatial location that belongs to the 2-dimensional space of real numbers  $s \in \mathbb{R}^2$ ,  $g(s)$  is noiseless data,  $k(s)$  denotes the speckle noise of unknown distribution and  $m(s)$  is measured data with respect to  $g(s)$  and  $k(s)$ . To reduce the speckle noise in the ultrasound images, we proposed the use of optimized BLSE filter for estimation of noiseless data in logarithmic domain. The BLSE filter suppress multiplicative noise by effective utilization of optimally tuned parameters of gray scale images. The statistics of speckle noise are affected from the logarithmic component such that local mean and local variance are proportional to each other rather than standard deviation. As a result, the speckle noise in the carotid ultrasound image turns in to Gaussian noise. The Gaussian noise is preferred because because it corresponds to quadratic data term, which is linear and easy to solve. Therefore, the measured data projected in to logarithmic space in such a way that distribution of noise is approximately close to the white Gaussian noise. The expanded logarithmic component of the measured data is expressed from the Eq.(3.1):

$$m_L(s) = g_L(s) + k_L(s) \quad (3.2)$$

In the logarithmic domain, the BLSE of  $g_L(s)$  can be defined by the expression ( Wong *et al.* (2010)):

$$\widehat{g}_L(s) = \arg \underbrace{\min}_{g_L(s)} \int p(g_L(s)|m_L(n))(g_L(s) - \widehat{g}_L(s))^2 dg_L(n) \quad (3.3)$$

The BLSE filter minimizes the average squared error of noise free data  $\widehat{g}_L(s)$  based on



the measured data  $m_L(s)$ . Minimizing the expression in Eq.(3.3) gives:

$$\widehat{g}_L(s) = \int p(g_L(s)|m_L(s))g_L(s)dg_L(s) \quad (3.4)$$

The Eq.(3.4) represents the optimized BLSE of the noiseless data  $g_L(s)$  based on the measured data  $m_L(s)$ . The distributed probability of noiseless data  $g_L(s)$  based on the measured data  $m_L(s)$  is non linear and it is complicated due to the posterior distribution  $p(g_L(s)|m_L(s))$ ; hence  $\widehat{g}_L(s)$  using Eq.(3.4) is difficult to solve. To overcome this problem, we proposed to use posterior conditional approach to estimate  $p(g_L(s)|m_L(s))$ . The posterior probability distribution is determined based on initial probability distribution  $q(s'|s)$  and  $q(s'|s)$  is defined as a Gaussian distribution centred at  $s$  ( Wong *et al.* (2010)):

$$q(s'|s) = \frac{1}{2\pi\sigma} e^{-\left(\frac{\|s'-s\|^2}{2\sigma^2}\right)} \quad (3.5)$$

where  $\|s' - s\|^2$  represents Euclidean distance of site  $s'$  from  $s$ , and  $\sigma$  refers to the spatial variance. The posterior distribution  $p(g_L(s)|m_L(s))$  is estimated based on the condition from a given location  $s'$  expressed as ( Wong *et al.* (2010)):

$$|a(s) - a(s')| < 2\sigma_n \quad (3.6)$$

where  $\sigma_n$  is the estimated noise variance and  $a(s)$  indicates the local average of neighbourhood pixels centred at  $s$ . This condition is iterated to get maximum number of locations which are used to estimate the original signal. The associated location  $s'$  of each weight for estimating  $g_L(s)$  can be represented by  $w(s'_i|s)$  which is defined as ( Wong *et al.* (2010)):

$$w(s'_i|s) = e^{-\left(\frac{\|a(s'_i)-a(s)\|^2}{2\sigma^2}\right)} \quad (3.7)$$

This weight is more reliable to estimate probability distribution by weighting locations with local means. Using associated set of locations  $t = (s'_1, s'_2, \dots, s'_\gamma)$  and given set of weights  $(w(s'_1, s), w(s'_2, s), \dots, w(s'_\gamma, s))$ , the posterior probability is estimated based on histogram weighted approach. Consider the weighted histogram where  $h(r_k)$  is the  $k^{th}$  noiseless possible data value. For each location  $s'_i$ , the weight  $w(s'_i|s)$  is accumulated in the histogram bin of the weighted histogram that corresponds to  $h(r_k = m_L(s'_i))$ . From the weighted histogram approach, posterior distribution  $p(g_L(s)|m_L(s))$  is estimated and expressed as ( Wong

et al. (2010)),

$$\widehat{p}(g_L(s)|m_L(s)) = \frac{\sum_{k=t} w(s'_k|s)\delta(g_L - m_L(s'_k))}{M} \quad (3.8)$$

where  $\delta(\cdot)$  represents the delta function and normalized factor  $M$  is defined as  $\sum_{g_L} \widehat{p}(g_L(s)|m_L(s)) = 1$ . Finally, the estimate of noiseless data  $g(s)$  can be calculated by projecting back the Bayesian estimate  $\widehat{g}_L(s)$  from the logarithmic domain using the exponential function,  $\widehat{g}(s) = \exp(\widehat{g}_L(s))$ .

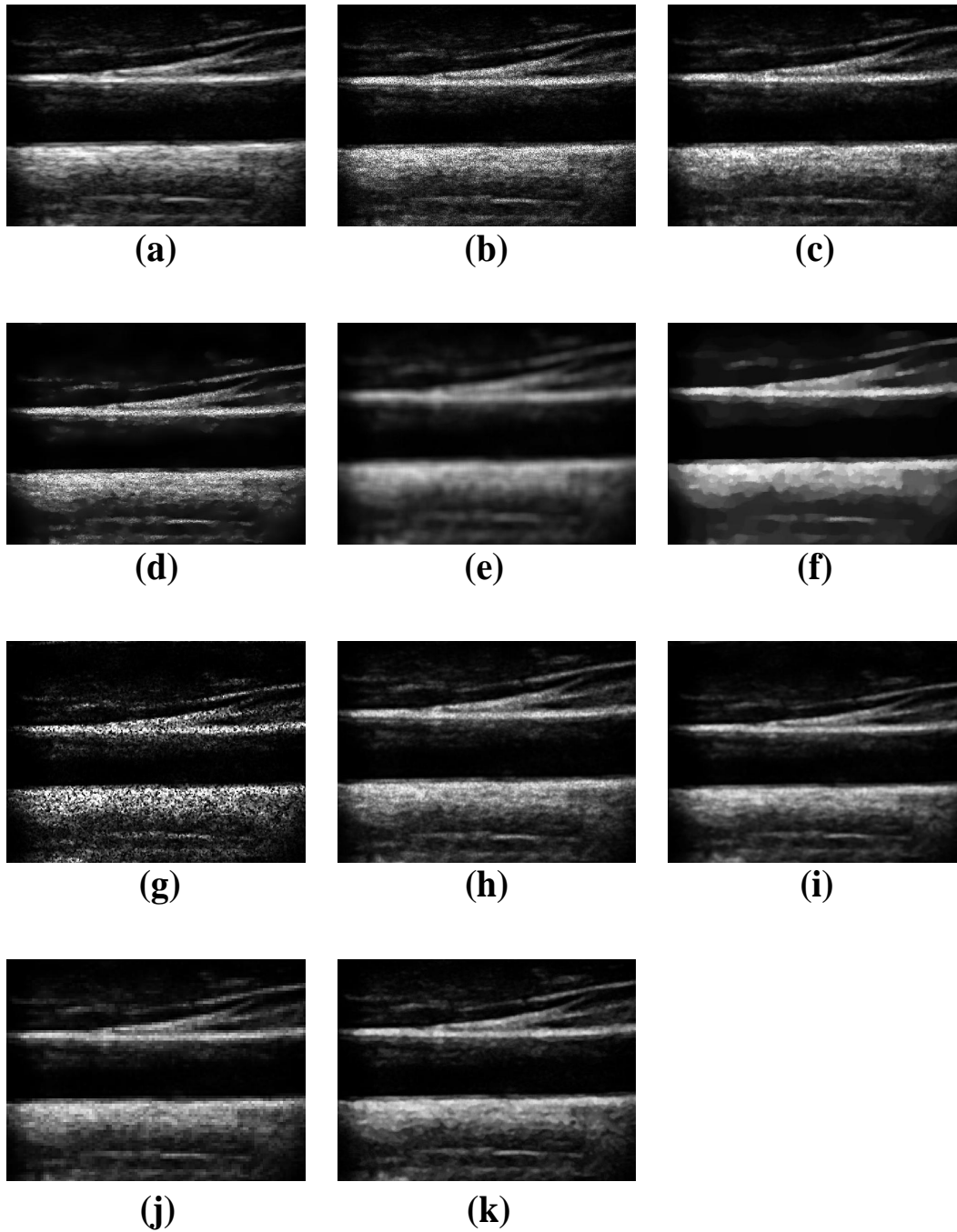
### 3.2.1 Results

In this section, we discuss the experimental results obtained from the state-of-the-art denoising filters on carotid ultrasound images. For our experiment, 50 ultrasound carotid images of several subjects have been obtained from Cyprus Institute Nicosia (C.Loizou (2002)).

**Table 3.1:** The quality metrics evaluated with variance of 0.1

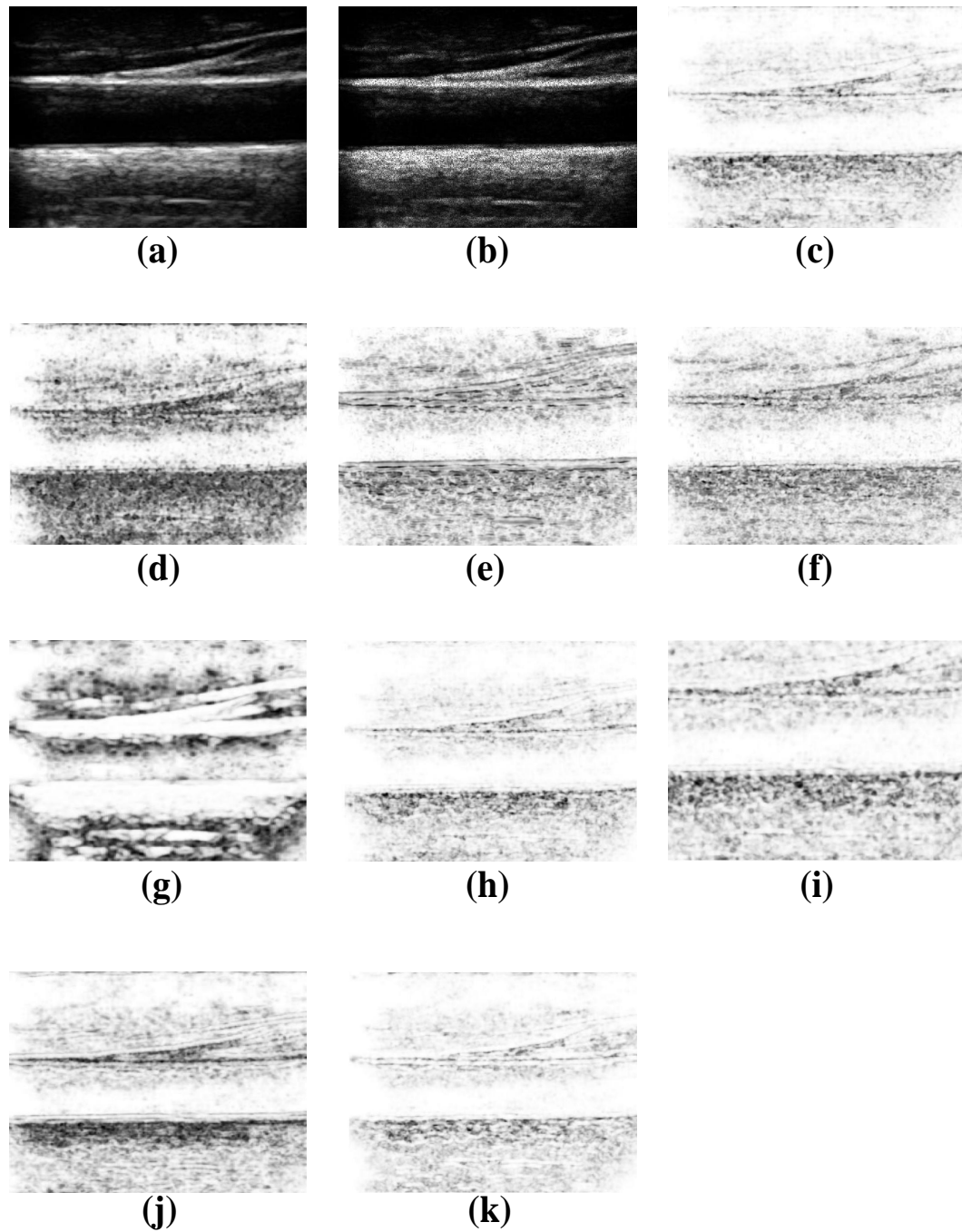
| <i>Filters</i>    | <i>PSNR<sub>mean</sub></i> | <i>SNR<sub>mean</sub></i> | <i>RMS E<sub>mean</sub></i> | <i>IQI</i> | <i>SSIM</i> | <i>CoC</i> | <i>Execution Time(s)</i> |
|-------------------|----------------------------|---------------------------|-----------------------------|------------|-------------|------------|--------------------------|
| Median            | 30.304                     | 15.298                    | 3.119                       | 0.7754     | 0.8611      | 0.9736     | 11.31                    |
| SRAD              | 27.746                     | 15.76                     | 2.167                       | 0.5528     | 0.8385      | 0.9734     | 20.32                    |
| NLM               | 27.702                     | 12.695                    | 4.401                       | 0.3172     | 0.6840      | 0.9585     | 84.60                    |
| Total-Variation   | 29.596                     | 14.583                    | 3.381                       | 0.3499     | 0.7160      | 0.9803     | 37.44                    |
| DPAD              | 25.374                     | 10.519                    | 3.940                       | 0.2907     | 0.6506      | 0.8356     | 25.36                    |
| Lee               | 33.320                     | 18.313                    | 2.103                       | 0.7798     | 0.8694      | 0.9862     | 23.95                    |
| Frost             | 29.904                     | 17.458                    | 2.213                       | 0.6978     | 0.7790      | 0.9782     | 24.95                    |
| Wavelet Filtering | 31.692                     | 20.303                    | 3.130                       | 0.6098     | 0.6211      | 0.9634     | 26.13                    |
| Proposed Method   | 34.090                     | 18.983                    | 1.966                       | 0.8270     | 0.9023      | 0.9884     | 21.74                    |

Speckle reduction algorithms constituting different kinds of filters have been implemented using MATLAB 2015a and tested on Intel Core i7 machine with 2GB of RAM. In all these images, speckle reduction algorithm is applied and results are measured with the statistical metrics of the respective filters. Performance of all the filters have been compared and tested using various ultrasound carotid images in terms of visual inspection of enlarged/zoomed region of interest of despeckling images. To exemplify the performance of the proposed techniques, we added ultrasound carotid images with variances of speckle noise 0.1 and 0.5. Figure (3.1) illustrates the complete results of the ultrasound carotid



**Figure 3.1:** Carotid ultrasound images with speckle noise variance ( $\sigma^2$ ) 0.1. (a) Noise-free image. (b) Noisy image. (c) Median. (d) SRAD. (e) NLM. (f) Total-Variation. (g) DPAD. (h) Lee. (i) Frost. (j) Wavelet filter. (k) Proposed filter.

images with a noise variance of 0.1 and the corresponding SSIM images of the carotid images in the test run are shown in Figure (3.2). We can qualitatively analyse that the proposed



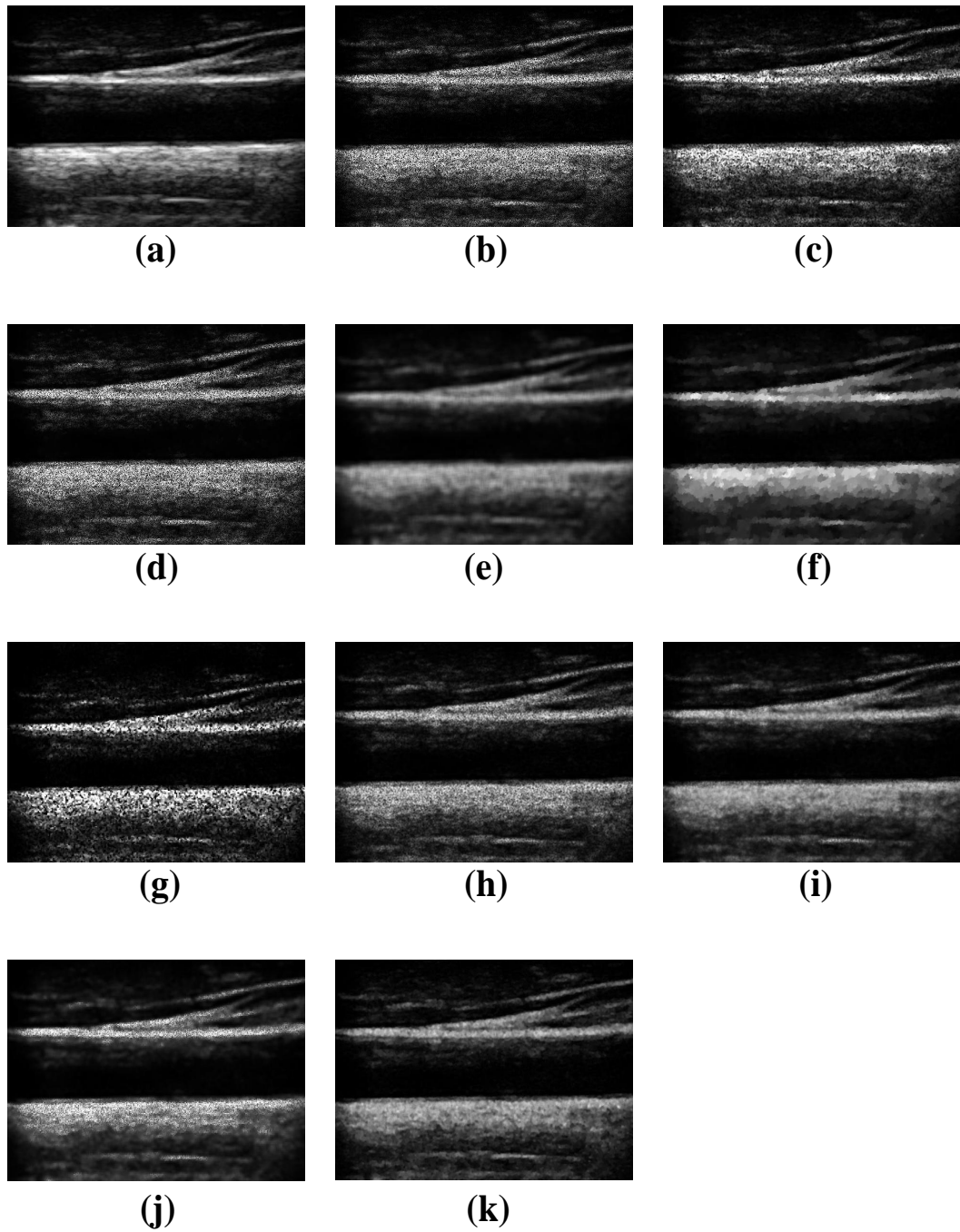
**Figure 3.2:** SSIM factor of carotid ultrasound images with variance ( $\sigma^2$ ) 0.1 (Brighter indicates better SSIM value). (a) Noise-free image. (b) Noisy image. (c) Median. (d) SRAD. (e) NLM. (f) Total-Variation. (g) DPAD. (h) Lee. (i) Frost. (j) Wavelet filter. (k) Proposed filter.

method demonstrates a superior edge preserving behaviour as compared to other techniques. Further, the various performance metrics are calculated for the filtered images and shown

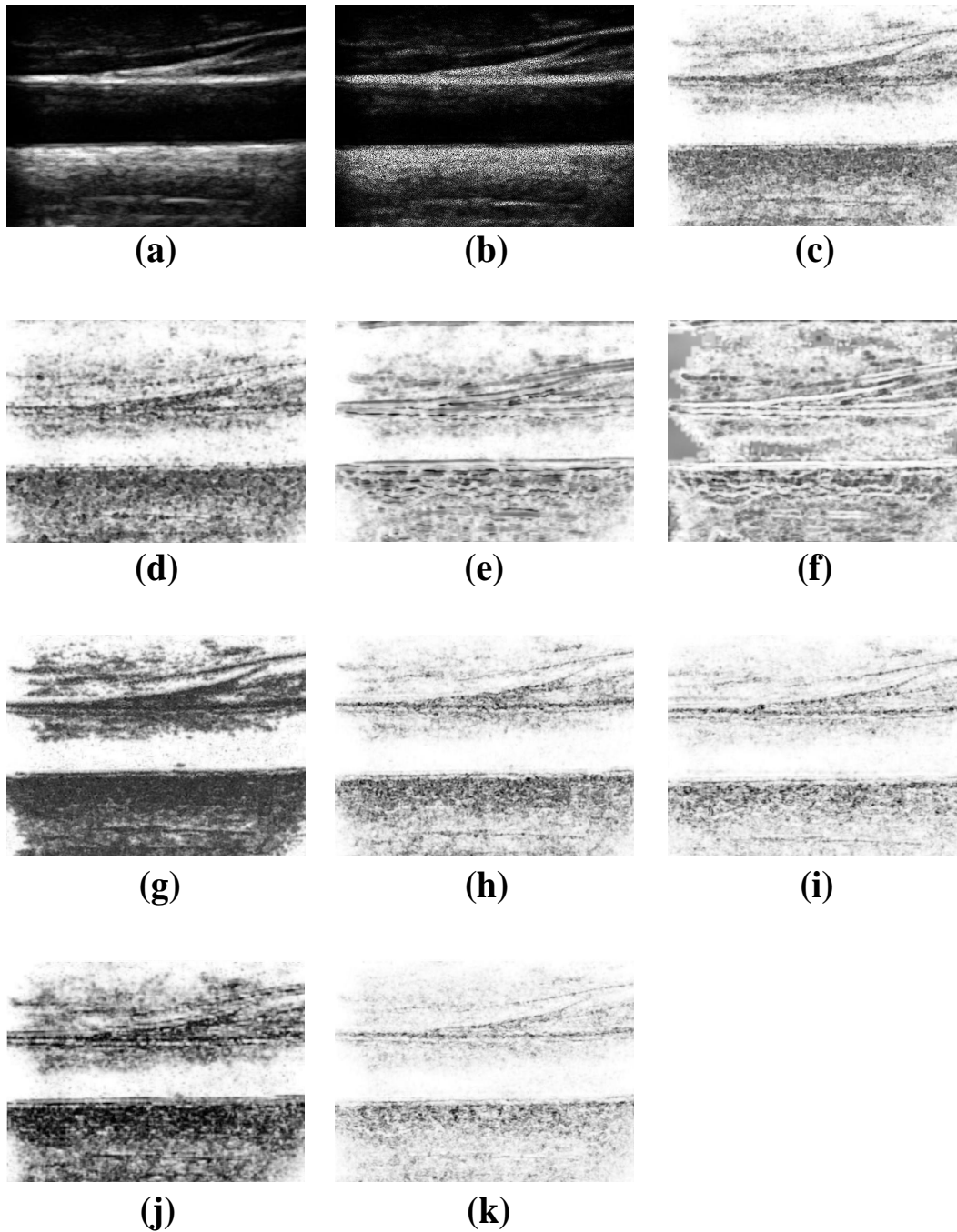
**Table 3.2:** The quality metrics evaluated with variance of 0.5

| <i>Filters</i>    | <i>PSNR<sub>mean</sub></i> | <i>SNR<sub>mean</sub></i> | <i>RMS E<sub>mean</sub></i> | <i>IQI</i> | <i>SSIM</i> | <i>CoC</i> | <i>Execution Time(s)</i> |
|-------------------|----------------------------|---------------------------|-----------------------------|------------|-------------|------------|--------------------------|
| Median            | 27.463                     | 12.326                    | 5.531                       | 0.5783     | 0.6519      | 0.9132     | 11.32                    |
| SRAD              | 26.814                     | 14.811                    | 5.533                       | 0.5768     | 0.6432      | 0.9559     | 20.34                    |
| NLM               | 26.923                     | 12.112                    | 4.181                       | 0.3173     | 0.6512      | 0.9493     | 80.26                    |
| Total-Variation   | 28.815                     | 13.878                    | 3.169                       | 0.3427     | 0.6647      | 0.9521     | 37.50                    |
| DPAD              | 23.639                     | 8.245                     | 6.224                       | 0.2977     | 0.5818      | 0.7518     | 25.39                    |
| Lee               | 27.489                     | 12.482                    | 4.339                       | 0.6347     | 0.7390      | 0.9436     | 23.96                    |
| Frost             | 26.702                     | 14.929                    | 5.923                       | 0.6210     | 0.7338      | 0.9419     | 24.57                    |
| Wavelet Filtering | 28.933                     | 13.681                    | 6.158                       | 0.3972     | 0.6654      | 0.9589     | 26.14                    |
| Proposed Method   | 30.089                     | 14.98                     | 3.357                       | 0.6574     | 0.7907      | 0.9675     | 21.62                    |

in Table 3.1. The median, Lee, and Frost filters reduce the speckle noise and improve the edge information. These filters are spatially adaptive, which uses a sliding window filter and measures the statistical data of all pixel values such as local mean and variance. Total Variation and wavelet filters often suffer from the staircase effect and the loss of fine details. NLM filter preserves the details but it takes more execution time. SRAD filter tends to burden thin linear features and point features which needs to be corrected. DPAD filter do not give significant differences in despeckling compared with existing filters. From the Table 3.1, we can quantitatively analyse that the proposed filter has a larger value in terms of the PSNR, SNR, CoC, IQI and SSIM than the other filter techniques and a smaller value of RMSE than the other filters. The CPU runtime of the proposed method is better than most of the tested techniques except for median and SRAD methods, however it outperforms in other metrics. Similarly, Figure (3.3) illustrates the complete results of ultrasound carotid images with a variance of 0.5 and their SSIM images of the carotid images in the test run are given Figure (3.4). The various performance metrics are calculated for filtered images shown in Table 3.2. Thus, from the qualitative and quantitative analysis, it is found that proposed method gives better performance compared to the other filters by exhibiting optimal filtering operation for speckle removal in carotid ultrasound images.



**Figure 3.3:** Carotid ultrasound images with speckle noise variance ( $\sigma^2$ ) 0.5. (a) Noise-free image. (b) Noisy image. (c) Median. (d) SRAD. (e) NLM. (f) Total-Variation. (g) DPAD. (h) Lee. (i) Frost. (j) Wavelet filter. (k) Proposed filter.



**Figure 3.4:** SSIM factor of carotid ultrasound images with variance  $(\sigma^2) 0.5$  (Brighter indicates better SSIM value). (a) Noise-free image. (b) Noisy image. (c) Median. (d) SRAD. (e) NLM. (f) Total-Variation. (g) DPAD. (h) Lee. (i) Frost. (j) Wavelet filter. (k) Proposed filter.

### **3.3 Comparison of edge detection and despeckling on carotid ultrasound images**

Edge detection is a very important step in the digital image segmentation and analysis. Edge detection works like a boundary detection between the two regions having different intensity values. Edge may appear in horizontal as well as vertical direction. The carotid ultrasound image is convolved with small size kernels to estimate the image brightness distribution of first-order directional derivatives. Kernels are predefined groups of edge models that match each image segment of a fixed size. The brief description of each operator is explained below.

#### **Sobel Operator:**

Sobel operator is a discrete operator used to estimate the gradient of image intensity for edge detection (Muthukrishnan and Radha (2011)). The input image convolves with the kernel to measure gradient component in each orientation. The kernels are designed such way that edges run vertically and horizontally relative to the pixel grid.

#### **Prewitt Operator:**

The prewitt operator is based on convolving the image with a small, separable and integer value filter in horizontal and vertical direction and is therefore relatively expensive in terms of computation (Haider *et al.* (2012)).

#### **Roberts Operator:**

Robert operator method is a fast and simple structure (Muthukrishnan and Radha (2011)). The region of high spatial frequency is highlighted which correspond to the edges. Pixel value at each point in the output represents the estimated absolute magnitude of the input image at that point.

#### **Laplacian of Gaussian (LoG) Operator:**

LoG operator is used for an image to highlight the regions of abrupt change in the intensity values (Brosnan and Sun (2004)). The advantage of LoG operator is easy to detect edges and their orientations.

#### **Canny Operator:**

Canny Operator is considered as an optimal edge detection method (Canny (1986)). The edge detection is performed by using a critical threshold value and helps in reducing noise in the image.



### 3.3.1 Automatic ROI extraction

In ultrasound images, due to speckle noise, the image contrast get reduced. The speckle present in the ultrasound image is reduced using an optimized BLSE filter. The image is then enhanced by Total Variation  $L^1$  (TV-  $L^1$ ) norm based on histogram equalization technique (Ghita *et al.* (2013)). The overall block diagram of automatic ROI extraction is shown in Figure 3.5 and each block is explained below.

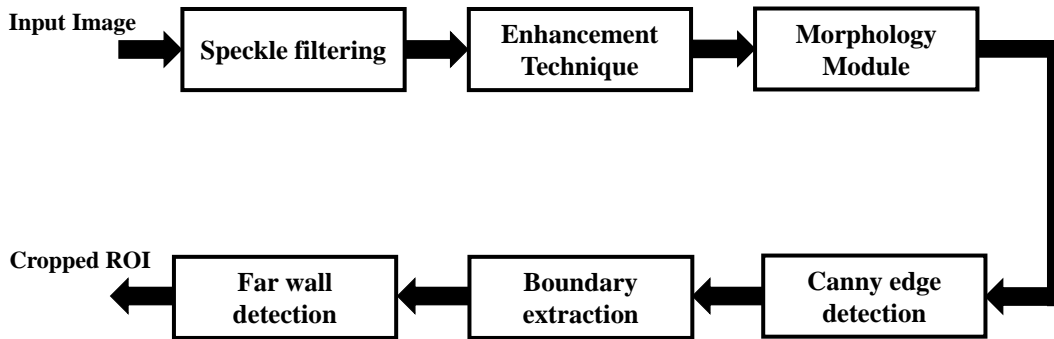
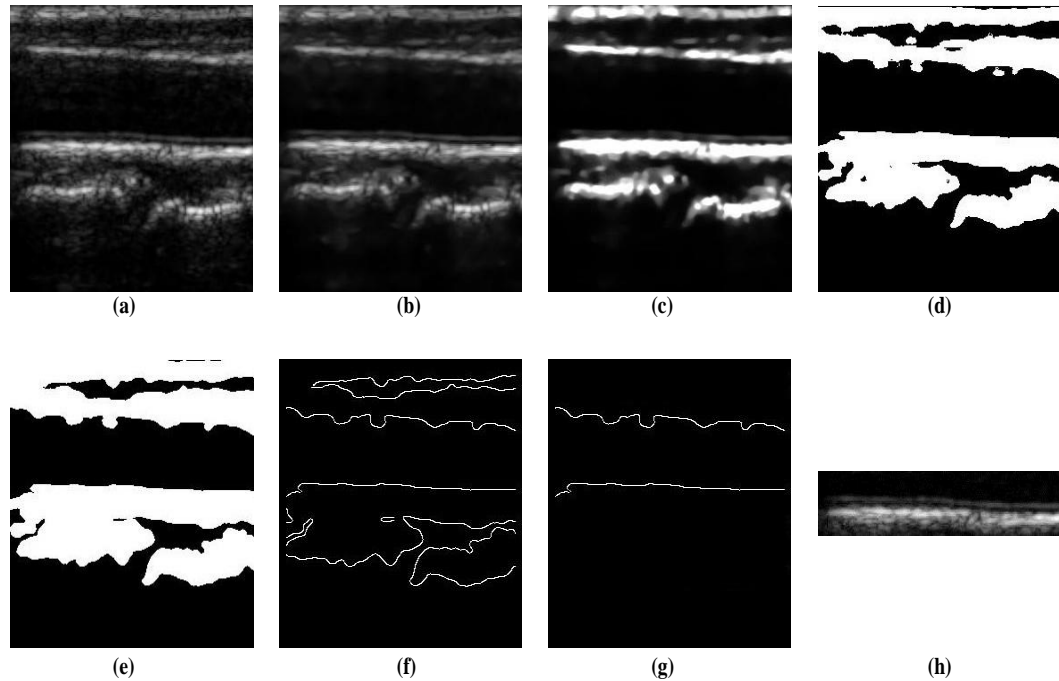


Figure 3.5: Outline of ROI extraction.

**Speckle Filtering Technique:** Carotid ultrasound images are affected by speckle noise that degrades the quality of the image. To improve the quality of the image, the optimized bayesian least square estimation (BLSE) (Wong *et al.* (2010)) despeckling filter is used. The BLSE filter method suppress multiplicative noise by effective utilization of optimally tuned parameters of gray scale images. The despeckled image is shown in the Figure 3.6(b) and detailed explanation of BLSE algorithm is already discussed in section 3.2.

**Image Enhancement:** The contrast enhancement (Zhang *et al.* (2014)) technique improves the visual appearance of the image by changing the pixel intensity of original image. The main objective of the enhancement is to process an image so that the resultant image contains more relevant information than the original image. In this work, TV-  $L^1$  norm (Ghita *et al.* (2013)) model is used for enhancement by applying a histogram warping process. Figure (3.6(c)) shows the enhanced image using TV- $L^1$  norm.

**Morphology Operation:** Morphological functions are used to clean the edges which are generated by the binary process (see Figure (3.6(d))). Morphological opening function is applied to eliminate gaps and fill the holes in plaque contour of the image (Gonzalez and Woods (2004)). In this experiment, morphological area opening followed by dilation is performed to remove the outliers near the boundaries. A structuring element of size 2 pixels is used to seal the plaque contour of carotid ultrasound images. As seen in Figure 3.6(e),



**Figure 3.6:** Automatic extraction of ROI. (a) Original carotid longitudinal ultrasound image. (b) De-speckled image using BLSE filter. (c) Enhancement using TV-  $L^1$  norm. (d) Conversion to the binary image with automatic thresholding procedure. (e) Morphological operation on the binary image. (f) Canny edge detection. (g) Extraction of the near and Far wall. (h) Automatic ROI extraction.

the outliers are removed and gaps are filled along with the edges.

**Canny Edge Detection:** Canny operators (Bao *et al.* (2005)) smooth the data by means of Gaussian convolution and then performs the edge detection operation. It gives an accurate representation of the true edges of the artery while helping to eliminate the creation of false edges due to speckle noise in the image. The Canny operator uses an input gray scale image and creates an output image showing the position of tracked intensity discontinuities. Figure (3.6(f)) shows the detection of edges using Canny operator.

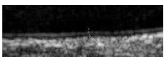
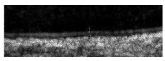

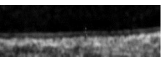
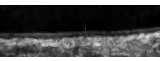












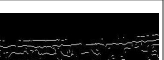





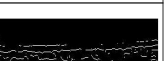












**Boundary Extraction:** The near wall and far wall boundaries are extracted by searching the random point in the lumen region using the minimum sum of column spanning index. The random point is moved upward and downward till the high-intensity gray scale value(255) is found. Using the high-intensity gray scale value, near wall and far wall are extracted based on the region-prop properties (Regionprop (2002)). The extracted near wall and far wall are shown in Figure (3.6(g)).

**Far Wall Detection:** In the longitudinal view, the line above lumen is known as near

wall and bottom is far wall (as seen from Figure 3.6(g)). Usually, the thickness of IMT is estimated in the far wall region because measuring the IMT of the far wall is more reliable than the measurement performed in near wall. The random point is considered on the far wall line and corresponding to that point a region 30 pixels upward and 30 pixels downward are extracted. Finally, the cropped ROI is shown in the Figure (3.6(h)).

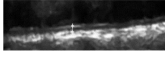
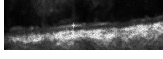
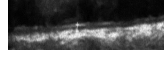

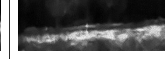










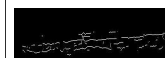


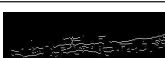


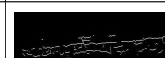

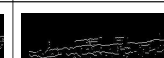












### 3.3.2 Results

In this section, we discuss the results of different edge detection operators on the framework of despeckling filters. The purpose of edge detection is to retain the structural properties of the image for further image processing. For our experiment, we used two different datasets, namely dataset 1 and dataset 2. Dataset 1 consists of 25 images collected from Cyprus Institute of Neurology of Nicosia (Cyprus (2007)). Dataset 2 consist of 25 images collected from the Father Muller Medical Hospital, Mangalore, India. The performance of the proposed method is evaluated by adding speckle noise with variance of 0.05 and 0.1 to the carotid ultrasound images.

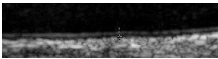
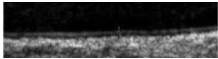
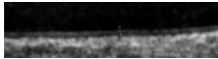
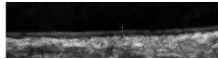














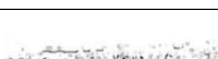
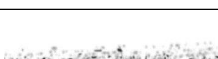



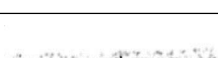

| Edge Detection Methods | Ground Truth Image  | Noisy Image   | Denoised with LEE filter  | Denoised with SRAD filter  | Denoised with OBFLM filter  | Denoised with BLSE filter   |
|------------------------|---|---|---|--|---|---|
|                        |  |  |  |  |  |  |
| Canny Edge Detection   |  |  |  |  |  |  |
| Sobel Edge Detection   |  |  |  |  |  |  |
| Prewitt Edge Detection |  |  |  |  |  |  |
| Roberts Edge Detection |  |  |  |  |  |  |
| LOG Edge Detection     |  |  |  |  |  |  |

**Figure 3.7:** Edge detection techniques for carotid ultrasound images of Dataset 1 with noise variance of 0.05.

Figure (3.7) and Figure (3.8) depict the carotid ultrasound images of Dataset 1 and Dataset 2, on which we added speckle noise with variance of 0.05 and applied different denoising filters. Subsequently, edges are extracted from the denoising filters using edge

| Edge Detection Methods | Ground Truth Image  | Noisy Image   | Denoised with LEE filter  | Denoised with SRAD filter  | Denoised with OBNLM filter  | Denoised with BLSE filter   |
|------------------------|---|---|---|--|---|---|
|                        |  |  |  |  |  |  |
| Canny Edge Detection   |  |  |  |  |  |  |
| Sobel Edge Detection   |  |  |  |  |  |  |
| Prewitt Edge Detection |  |  |  |  |  |  |
| Roberts Edge Detection |  |  |  |  |  |  |
| LOG Edge Detection     |  |  |  |  |  |  |

**Figure 3.8:** Edge detection techniques for carotid ultrasound images of Dataset 2 with noise variance of 0.05.

| Ground Truth Image  | Denoised with LEE filter  | Denoised with SRAD filter  | Denoised with OBNLM filter  | Denoised with BLSE filter   |
|---|---|--|---|---|
|  |  |  |  |  |
| Canny Edge Detection  |  |  |  |  |
| Sobel Edge Detection  |  |  |  |  |
| Prewitt Edge Detection  |  |  |  |  |
| Robert Edge Detection   |  |  |  |  |
| LOG Edge Detection  |  |  |  |  |

**Figure 3.9:** Structural similarity index (Brighter indicates better SSIM value) of carotid ultrasound images of Dataset 1 with variance of 0.05.

operators and compared with the results of edges extracted by edge operators of the original image. SSIM is used to measure the similarity of the edges between denoised image and original image as shown in Figure (3.9) and Figure (3.10). From visual inspection,

| Ground Truth Image     | Denoised with LEE filter | Denoised with SRAD filter | Denoised with OBNLM filter | Denoised with BLSE filter |
|------------------------|--------------------------|---------------------------|----------------------------|---------------------------|
|                        |                          |                           |                            |                           |
| Canny Edge Detection   |                          |                           |                            |                           |
| Sobel Edge Detection   |                          |                           |                            |                           |
| Prewitt Edge Detection |                          |                           |                            |                           |
| Robert Edge Detection  |                          |                           |                            |                           |
| LOG Edge Detection     |                          |                           |                            |                           |


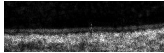
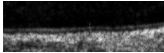

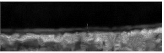






















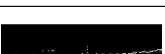



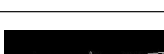

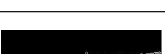
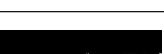
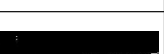
**Figure 3.10:** Structural similarity index (Brighter indicates better SSIM value) of carotid ultrasound images of Dataset 2 with variance of 0.05.

**Table 3.3:** Mean PSNR, Mean MSE, Mean CoC and Mean SSIM of Lee denoising filter with different edge detection techniques for 50 carotid ultrasound images.

| Dataset 1 with Lee filter |                    |                    |                    |                    |                    |
|---------------------------|--------------------|--------------------|--------------------|--------------------|--------------------|
| Metric                    | Canny              | Sobel              | Prewitt            | Robert             | LoG                |
| $PSNR_{mean} \pm std$     | 64.2808±<br>0.2462 | 63.6296±<br>0.2666 | 63.6850±<br>0.2538 | 62.5048±<br>0.5915 | 63.2677±<br>0.5608 |
| $MSE_{mean} \pm std$      | 0.0385±<br>0.0022  | 0.0355±<br>0.0021  | 0.0351±<br>0.0020  | 0.0583±<br>0.0079  | 0.0488±<br>0.0063  |
| $CoC_{mean}$              | 0.6562             | 0.4748             | 0.4757             | 0.2172             | 0.6558             |
| $SSIM_{mean}$             | 0.9993             | 0.9991             | 0.9992             | 0.9986             | 0.9990             |
| Dataset 2 with Lee filter |                    |                    |                    |                    |                    |
| Metric                    | Canny              | Sobel              | Prewitt            | Robert             | LoG                |
| $PSNR_{mean} \pm std$     | 65.5473±<br>0.8673 | 64.3143±<br>1.0513 | 64.9427±<br>1.0346 | 62.3705±<br>0.6478 | 63.4591±<br>0.6227 |
| $MSE_{mean} \pm std$      | 0.0272±<br>0.0047  | 0.0246±<br>0.0054  | 0.0244±<br>0.0053  | 0.0616±<br>0.0096  | 0.0457±<br>0.0063  |
| $CoC_{mean}$              | 0.5045             | 0.3970             | 0.4183             | 0.3378             | 0.5013             |
| $SSIM_{mean}$             | 0.9993             | 0.9992             | 0.9993             | 0.9985             | 0.9989             |

**Table 3.4:** Mean PSNR, Mean MSE, Mean CoC and Mean SSIM of SRAD denoising filter with different edge detection techniques for 50 carotid ultrasound images.

| <b>Dataset 1 with SRAD filter</b> |                    |                    |                    |                    |                    |
|-----------------------------------|--------------------|--------------------|--------------------|--------------------|--------------------|
| <b>Metric</b>                     | <b>Canny</b>       | <b>Sobel</b>       | <b>Prewitt</b>     | <b>Robert</b>      | <b>LoG</b>         |
| $PSNR_{mean} \pm std$             | 64.1425±<br>0.7999 | 63.6798±<br>0.6089 | 63.7140±<br>0.6074 | 60.4831±<br>0.4385 | 62.5281±<br>0.7766 |
| $MSE_{mean} \pm std$              | 0.0317±<br>0.0044  | 0.0353±<br>0.0049  | 0.0351±<br>0.0049  | 0.0735±<br>0.0074  | 0.0733±<br>0.0125  |
| $CoC_{mean}$                      | 0.5407             | 0.4645             | 0.4748             | 0.4907             | 0.5860             |
| $SSIM_{mean}$                     | 0.9988             | 0.9986             | 0.9982             | 0.9980             | 0.9964             |
| <b>Dataset 2 with SRAD filter</b> |                    |                    |                    |                    |                    |
| <b>Metric</b>                     | <b>Canny</b>       | <b>Sobel</b>       | <b>Prewitt</b>     | <b>Robert</b>      | <b>LoG</b>         |
| $PSNR_{mean} \pm std$             | 64.8027±<br>1.4865 | 64.0302±<br>0.9437 | 63.8864±<br>0.9721 | 61.8838±<br>0.3237 | 63.2194±<br>0.6539 |
| $MSE_{mean} \pm std$              | 0.0278±<br>0.0058  | 0.0274±<br>0.0057  | 0.0271±<br>0.0059  | 0.0669±<br>0.0049  | 0.0495±<br>0.0070  |
| $CoC_{mean}$                      | 0.5130             | 0.3820             | 0.3902             | 0.4099             | 0.5150             |
| $SSIM_{mean}$                     | 0.9994             | 0.9994             | 0.9991             | 0.9986             | 0.9988             |

| <b>Edge Detection Methods</b> | <b>Ground Truth Image</b>   | <b>Noisy Image</b>  | <b>Denosed with LEE filter</b>  | <b>Denosed with SRAD filter</b>  | <b>Denosed with OBNLM filter</b>  | <b>Denosed with BLSE filter</b>   |
|-------------------------------|---|---|---|--|---|---|
|                               |  |  |  |  |  |  |
| <b>Canny Edge Detection</b>   |  |  |  |  |  |  |
| <b>Sobel Edge Detection</b>   |  |  |  |  |  |  |
| <b>Prewitt Edge Detection</b> |  |  |  |  |  |  |
| <b>Roberts Edge Detection</b> |  |  |  |  |  |  |
| <b>LOG Edge Detection</b>     |  |  |  |  |  |  |

**Figure 3.11:** Edge detection techniques for carotid ultrasound images of Dataset 1 with noise variance of 0.1.

**Table 3.5:** Mean PSNR, Mean MSE, Mean CoC and Mean SSIM of OBNLM denoising filter with different edge detection techniques for 50 carotid ultrasound images.

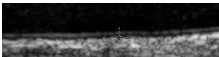

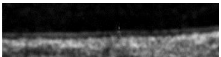
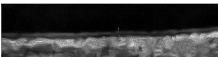

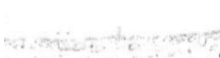
















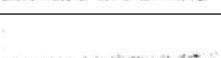
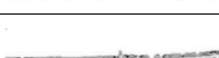
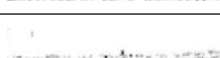
| Dataset 1 with OBNLM filter |                    |                    |                    |                    |                    |
|-----------------------------|--------------------|--------------------|--------------------|--------------------|--------------------|
| Metric                      | Canny              | Sobel              | Prewitt            | Robert             | LoG                |
| $PSNR_{mean} \pm std$       | 64.8556±<br>0.7654 | 63.7264±<br>0.3482 | 62.7900±<br>0.4226 | 60.6984±<br>0.7315 | 63.3933±<br>0.7514 |
| $MSE_{mean} \pm std$        | 0.0340±<br>0.0055  | 0.0438±<br>0.0033  | 61.7900±<br>0.4226 | 59.6984±<br>0.7315 | 60.3938±<br>0.7514 |
| $CoC_{mean}$                | 0.6173             | 0.3898             | 0.3954             | 0.3596             | 0.6078             |
| $SSIM_{mean}$               | 0.9990             | 0.9989             | 0.9986             | 0.9984             | 0.9988             |
| Dataset 2 with OBNLM filter |                    |                    |                    |                    |                    |
| Metric                      | Canny              | Sobel              | Prewitt            | Robert             | LoG                |
| $PSNR_{mean} \pm std$       | 65.2727±<br>0.6500 | 64.7631±<br>0.7348 | 63.8424±<br>0.7720 | 61.3422±<br>1.1954 | 64.5376±<br>1.2255 |
| $MSE_{mean} \pm std$        | 0.0308±<br>0.0047  | 0.0348±<br>0.0065  | 0.0342±<br>0.0067  | 0.0780±<br>0.0222  | 0.0592±<br>0.0166  |
| $CoC_{mean}$                | 0.4966             | 0.3666             | 0.3707             | 0.2286             | 0.4963             |
| $SSIM_{mean}$               | 0.9992             | 0.9991             | 0.9990             | 0.9986             | 0.9988             |

| Edge Detection Methods | Ground Truth Image | Noisy Image | Denoised with LEE filter | Denoised with SRAD filter | Denoised with OBNLM filter | Denoised with BLSE filter |
|------------------------|--------------------|-------------|--------------------------|---------------------------|----------------------------|---------------------------|
| Canny Edge Detection   |                    |             |                          |                           |                            |                           |
| Sobel Edge Detection   |                    |             |                          |                           |                            |                           |
| Prewitt Edge Detection |                    |             |                          |                           |                            |                           |
| Roberts Edge Detection |                    |             |                          |                           |                            |                           |
| LOG Edge Detection     |                    |             |                          |                           |                            |                           |

**Figure 3.12:** Edge detection techniques for carotid ultrasound images of Dataset 2 with noise variance of 0.1..

**Table 3.6:** Mean PSNR, Mean MSE, Mean CoC and Mean SSIM of Proposed denoising filter with different edge detection techniques for 50 carotid ultrasound images.

| <b>Dataset 1 with BLSE filter</b> |                    |                    |                    |                    |                    |
|-----------------------------------|--------------------|--------------------|--------------------|--------------------|--------------------|
| <b>Metric</b>                     | <b>Canny</b>       | <b>Sobel</b>       | <b>Prewitt</b>     | <b>Robert</b>      | <b>LoG</b>         |
| $PSNR_{mean} \pm std$             | 65.1218±<br>0.4996 | 63.3395±<br>0.4526 | 63.4135±<br>0.4670 | 61.2674±<br>0.5506 | 63.0588±<br>0.5644 |
| $MSE_{mean} \pm std$              | 0.0255±<br>0.0037  | 0.0381±<br>0.0040  | 0.0374±<br>0.0040  | 0.0615±<br>0.0078  | 0.0513±<br>0.0069  |
| $CoC_{mean}$                      | 0.6611             | 0.4379             | 0.4695             | 0.4735             | 0.6362             |
| $SSIM_{mean}$                     | 0.9994             | 0.9989             | 0.9991             | 0.9986             | 0.9990             |
| <b>Dataset 2 with BLSE filter</b> |                    |                    |                    |                    |                    |
| <b>Metric</b>                     | <b>Canny</b>       | <b>Sobel</b>       | <b>Prewitt</b>     | <b>Robert</b>      | <b>LoG</b>         |
| $PSNR_{mean} \pm std$             | 65.7955±<br>1.2014 | 64.4227±<br>1.0722 | 64.4337±<br>1.0216 | 63.1044±<br>0.5869 | 64.5946±<br>0.5137 |
| $MSE_{mean} \pm std$              | 0.0209±<br>0.0065  | 0.0302±<br>0.0069  | 0.0301±<br>0.0067  | 0.0639±<br>0.0090  | 0.0452±<br>0.0050  |
| $CoC_{mean}$                      | 0.5281             | 0.3707             | 0.3603             | 0.3773             | 0.5244             |
| $SSIM_{mean}$                     | 0.9995             | 0.9987             | 0.9992             | 0.9991             | 0.9989             |

| <b>Ground Truth Image</b>   | <b>Denoised with LEE filter</b>   | <b>Denoised with SRAD filter</b>   | <b>Denoised with OBNLM filter</b>   | <b>Denoised with BLSE filter</b>  |
|---|---|--|---|---|
|  |  |  |  |  |
| <b>Canny Edge Detection</b>   |  |  |  |  |
| <b>Sobel Edge Detection</b>   |  |  |  |  |
| <b>Prewitt Edge Detection</b>   |  |  |  |  |
| <b>Robert Edge Detection</b>  |  |  |  |  |
| <b>LOG Edge Detection</b>   |  |  |  |  |

**Figure 3.13:** Structural similarity index (Brighter indicates better SSIM value) of carotid ultrasound images of Dataset 1 with variance of 0.1.



| Ground Truth Image     | Denoised with LEE filter | Denoised with SRAD filter | Denoised with OBNLM filter | Denoised with BLSE filter |
|------------------------|--------------------------|---------------------------|----------------------------|---------------------------|
|                        |                          |                           |                            |                           |
| Canny Edge Detection   |                          |                           |                            |                           |
| Sobel Edge Detection   |                          |                           |                            |                           |
| Prewitt Edge Detection |                          |                           |                            |                           |
| Robert Edge Detection  |                          |                           |                            |                           |
| LOG Edge Detection     |                          |                           |                            |                           |

**Figure 3.14:** Structural similarity index (Brighter indicates better SSIM value) of carotid ultrasound images of Dataset 2 with variance of 0.1.

the BLSE filter with Canny edge detection of SSIM factor in carotid images shows lesser difference between edges of ground truth image and denoised image as compared to the other denoising techniques. Therefore, Canny edge detection is superior in terms of detail preservation in carotid images compared to other edge detection techniques. Similarly, Figure (3.11) and Figure (3.12) depict the carotid ultrasound images of Dataset 1 and Dataset 2, on which we added speckle noise with variance of 0.1 and applied different denoising filters. Subsequently, edges are extracted from the denoising filters using edge operators and compared with the results of edges extracted by edge operators of the original image. SSIM is used to measure the similarity of the edges between denoised image and original image as shown in Figure (3.13) and Figure (3.14). From the qualitative analysis, the proposed work demonstrates a better edge preserving behaviour with the help of BLSE filter and also achieves better results in terms of the visual inspection. Further, various performance metrics are evaluated for each denoising filter and tabulated in Table 3.3,3.4,3.5, and 3.6. The PSNR value of BLSE filter with Canny edge detector (Dataset1 ( $65.12 \pm 0.49$ ), Dataset2 ( $65.79 \pm 1.20$ )) gives higher value than the Lee filter (Dataset1 ( $64.28 \pm 0.24$ ), Dataset2 ( $65.54 \pm 0.86$ )), SRAD filter (Dataset1 ( $64.14 \pm 0.1425$ ), Dataset2( $64.80 \pm 1.48$ )) and optimized Bayesian non local mean (OBNLM) filter (Dataset1 ( $64.85 \pm 0.76$ ), Dataset2( $65.27 \pm 0.65$ )). Likewise, CoC (Dataset1 (0.66), Dataset2 (0.52))

and SSIM (Dataset1 (0.9994), Dataset2 (0.9995)) values of the BLSE filter with Canny edge detector gives larger value than Lee filter, SRAD filter and OBNLN filter. The lowest values of MSE (Dataset1 (0.025±0.003), Dataset2(0.020±0.006)) are obtained from Canny edge detector with BLSE denoising filter compared to the Lee filter (Dataset1 (0.038±0.002), Dataset2 (0.027±0.004)), SRAD filter (Dataset1 (0.031±0.004), Dataset2 (0.027±0.005)) and Optimised Bayesian Non Local Mean (OBNLN) filter (Dataset1 (0.034±0.005), Dataset2 (0.030±0.004)). From these results, Canny edge detection with BLSE filter achieved the highest value of PSNR, CoC, SSIM and lowest value of MSE for the 50 carotid ultrasound images.

### 3.4 Summary

We have proposed the use of BLSE filter in logarithmic space based on conditional posterior sampling approach. The BLSE filter was compared with the state-of-the-art denoising filters, and experimental results showed that BLSE filter gives better results as compared to the other filter techniques. Based on the despeckling outputs, BLSE method gives better results in terms of all performance matrices and exhibits efficient noise reduction and preserves the edges as compared to other filters. Further, we have presented an automatic ROI extraction for detection of carotid wall and applied different denoising filters to the extracted ROI. Subsequently, the edges are extracted from the ROI using different edge detection operators and compared with the results of edges extracted by edge operators of the original image. The measured parameters PSNR, MSE, CoC and SSIM of BLSE denoising filter with Canny edge detection achieves better performance as compared to the other denoising methods.

---



## Chapter 4

# AUTOMATIC SEGMENTATION OF INTIMA MEDIA COMPLEX OF THE COMMON CAROTID ARTERY

This chapter focuses on carotid wall segmentation of longitudinal carotid ultrasound images. The speckle noise in carotid ultrasound images is reduced by making use of the state-of-the-art denoising techniques, followed by the application of enhancement techniques to increase the contrast. For better segmentation, we present novel ROI extraction approaches for detection of the carotid wall boundaries. Subsequently, the techniques based on support vector machine, wind driven optimisation and structured random forest classifier are applied on ROI for segmentation of IMT of the CCA. The proposed methods are compared with gradient-based methods such as model-based (MB), dynamic programming (DP), snake segmentation (SS) algorithms, and classifier based segmentation using a neural network (NN) algorithm.

### 4.1 Proposed method based on Support Vector Machine

In this Section, the speckle noise present in the carotid ultrasound images is reduced using optimized BLSE filter which is proposed in the section 3.2, and enhancement is based on  $TV-L_1$  norm to improve the robustness. Section 4.1.1 presents the automatic ROI extraction for segmentation of the IMT of the CCA. The support vector machine (SVM) algorithm is applied to the extracted ROI for measuring the IMT in the carotid ultrasound images which is described in section 4.1.2. Finally, the quantitative evaluation for measurement of IMT is

discussed in Section 4.1.3.

### 4.1.1 Automatic Extraction of the ROI

The ROI extraction is an important step for detection of boundaries of the image. In this stage, the far wall is detected in the image and the area surrounding the far wall is considered as our ROI. Initially, the original image of the CCA is cropped manually such way that no

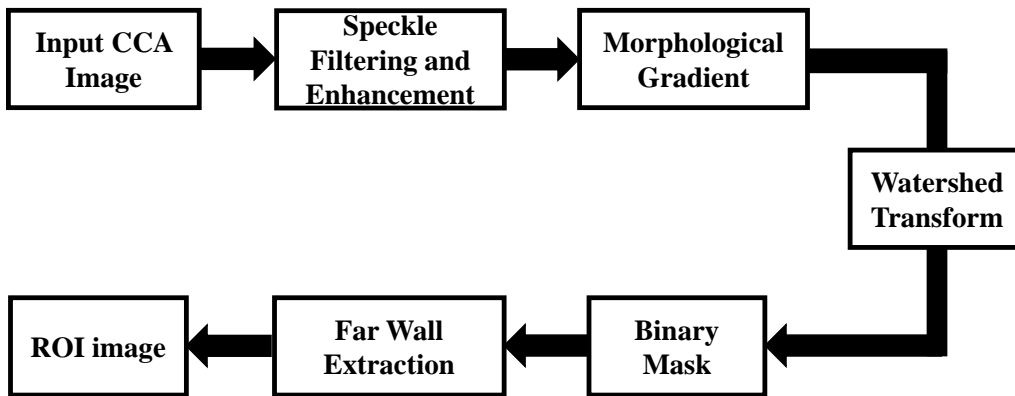
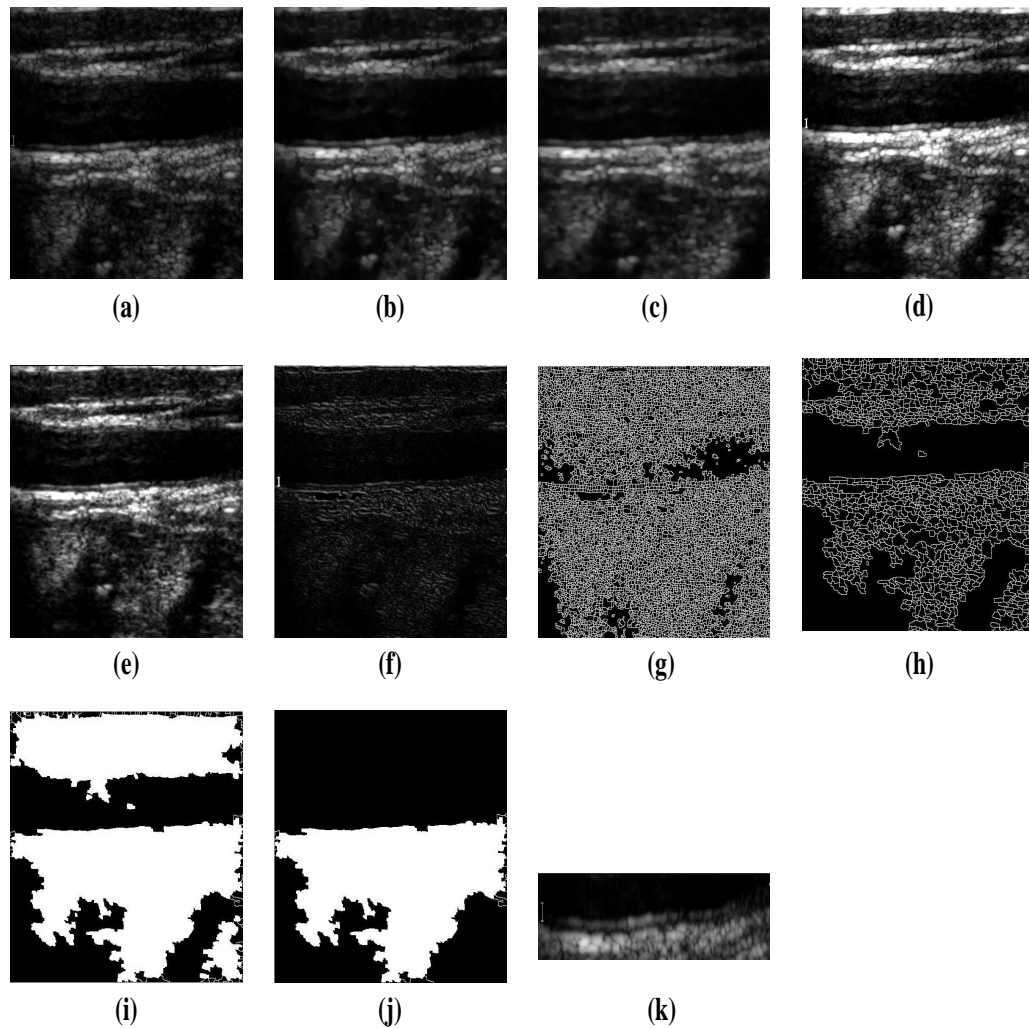


Figure 4.1: Outline of ROI extraction.

information about the image is lost. The contrast adjustment is to be made to the image so that the low and high-intensity value pixels can be visualized much better. The overall block diagram of automatic ROI extraction is shown in Figure 4.1 and each block is explained below.

- **Speckle Filtering and Enhancement Technique:** Normally, carotid ultrasound images are affected by the random granular pattern of speckle, which occurs due to the coherent nature of acquisition system. A speckle is a form of multiplicative noise which affects the interpretability of the image by experts and automated tool. To reduce the speckle noise, we estimate the noise free data in logarithmic domain based on BLSE approach using conditional posterior distribution. Figure 4.2(b) shows the despeckling image of the carotid artery. The contrast enhancement technique improves the visual appearance of the image by changing the pixel intensity of original image (Zhang *et al.* (2014)Kim (1997)). The main objective of the enhancement is to process an image so that the resultant image contains more relevant information than the original image. In this work, TV- $L^1$  norm (Ghita *et al.* (2013)) model is used



**Figure 4.2:** Automatic extraction of ROI. (a) Original carotid longitudinal ultrasound image. (b) Despeckle image using BLSE filter. (c) Enhancement using TV-  $L^1$  norm. (d) Dilation of the image. (e) Erosion of the image. (f) Morphological gradient of the image. (g) Boundaries of the watershed regions of the morphological gradient image over segmentation. (h) Boundaries of the watershed regions of the morphological gradient image over segmentation resolved. (i) Morphologically reconstructed image. (j) Largest Object in the lower half of the image. (k) ROI cropped image.

for enhancement by applying a histogram warping process. Figure 4.2(c) shows the enhanced image using TV- $L^1$  norm.

- **Morphological Gradient:**

The morphological dilation followed by erosion is performed on the denoised image.

For dilation and erosion, the structuring element as 'line' with the length of 4 pixels is used. The morphological gradient is calculated by taking the difference between the dilation and erosion of a given image. In morphological gradient image, each pixel value indicates the contrast intensity in the close neighborhood of the pixel. The dilation, erosion and morphological gradient of the cropped image are shown in Figure 4.2(d), 4.2e and 4.2f respectively. As we can observe in the Figure 4.2(f), the morphological gradient of the image contains only the edges in the image.

- **Watershed Transform:**

The next step in the process after getting the morphological gradient is the application of watershed transformation (Meyer (1994)). The watershed transformation is applied to the morphological gradient image and the resultant image gives many watershed regions as shown in Figure 4.2(g), leading to over segmentation. To overcome this problem, the sharp edges in the form of noise resulted in the lumen part of the morphological gradient is reduced using Gaussian low pass filter. The over segmentation of morphological gradient image is decreased but not entirely. The only way is to suppress all the pixels in the intensity image whose depth is less than a particular height. All the intensity pixels below certain height must be suppressed which depends on the pixel values of the entire image. Hence, the height is changed adaptively with the variance of the pixel values of the entire image. A binary image is built as same dimension as the input carotid ultrasound image using the border lines of the obtained watershed regions (see Figure 4.2(h)), which results in resolving the over segmentation of morphological gradient image. Hence, we obtain the primary mask in which only the boundaries of the watershed regions are white pixels.

- **Binary mask:**

To get the morphologically reconstructed image, the closed region in the primary mask is filled using mathematical operation based on morphological reconstruction algorithm (Gonzalez *et al.* (2004)). The obtained objects with larger areas are retained in the mask and other objects are removed.

- **Far wall extraction:**

To identify the far wall, the reconstructed image of two largest objects as shown in Figure 4.2(i) are to be identified first. After identifying the two largest objects, consider the one which is in the lower half of the image as shown in Figure 4.2(j). The

far wall can be easily detected by extracting the first non-zero pixel in each column of the Figure 4.2(j) which is a binary image.

- **Final ROI Image:**

After detecting the far-wall, the boundaries of the ROI can be easily established. The upper boundary is considered at 0.6mm above the uppermost point of far wall and the bottom boundary is considered at 1.5mm below the lowest point. The spatial density of the image 16.66 pixels/mm is multiplied to upper point and the lower point to get the approximate number of pixels in boundaries. Thus, the size of ROI relies upon the appearance of the carotid ultrasound image. Finally, the ROI is cropped based on the obtained pixels, which is shown in Figure 4.2(k) and further processed to obtain the final LI and MA interfaces to estimate the IMT.

#### 4.1.2 Segmentation using SVM

Segmentation using SVM is also considered as a pattern identification problem. The classification of a pixel into IMT boundary pixel or non-IMT boundary pixel is carried out on the basis of the pixel intensities in the neighbourhood of the pixel to be classified. SVM is used for the boundary detection in the ultrasound images of Common Carotid Artery. The MATLAB library that includes SVM, LIBSVM (Chang and Lin (2011)), is used to build the model and predict the results. Radial Basis Function(RBF) is used as kernel for segmentation of IMT in the carotid ultrasound images. The RBF kernel on two samples  $s$  and  $s'$ , representing the feature vectors in some input space, is defined as (Vert *et al.* (2004)):

$$K(s, s') = \exp\left(\frac{-\|s - s'\|^2}{2\sigma^2}\right) \quad (4.1)$$

where  $\|s - s'\|^2$  is recognized as the squared Euclidean distance between the two feature vectors  $s$  and  $s'$ . The  $\sigma$  is recognized as a free parameter. The Eq.4.1 is simplified by involving a parameter  $\gamma = \frac{1}{2\sigma^2}$  and it is expressed as,

$$K(s, s') = \exp(-\gamma \cdot \|s - s'\|^2) \quad (4.2)$$

In this case, the value of  $\gamma$  is considered as the number of features in the space. The square window of size 9×9 is moved around the ROI image pixel by pixel. The square



**Table 4.1:** Cross Validation of 49 ultrasound carotid images.

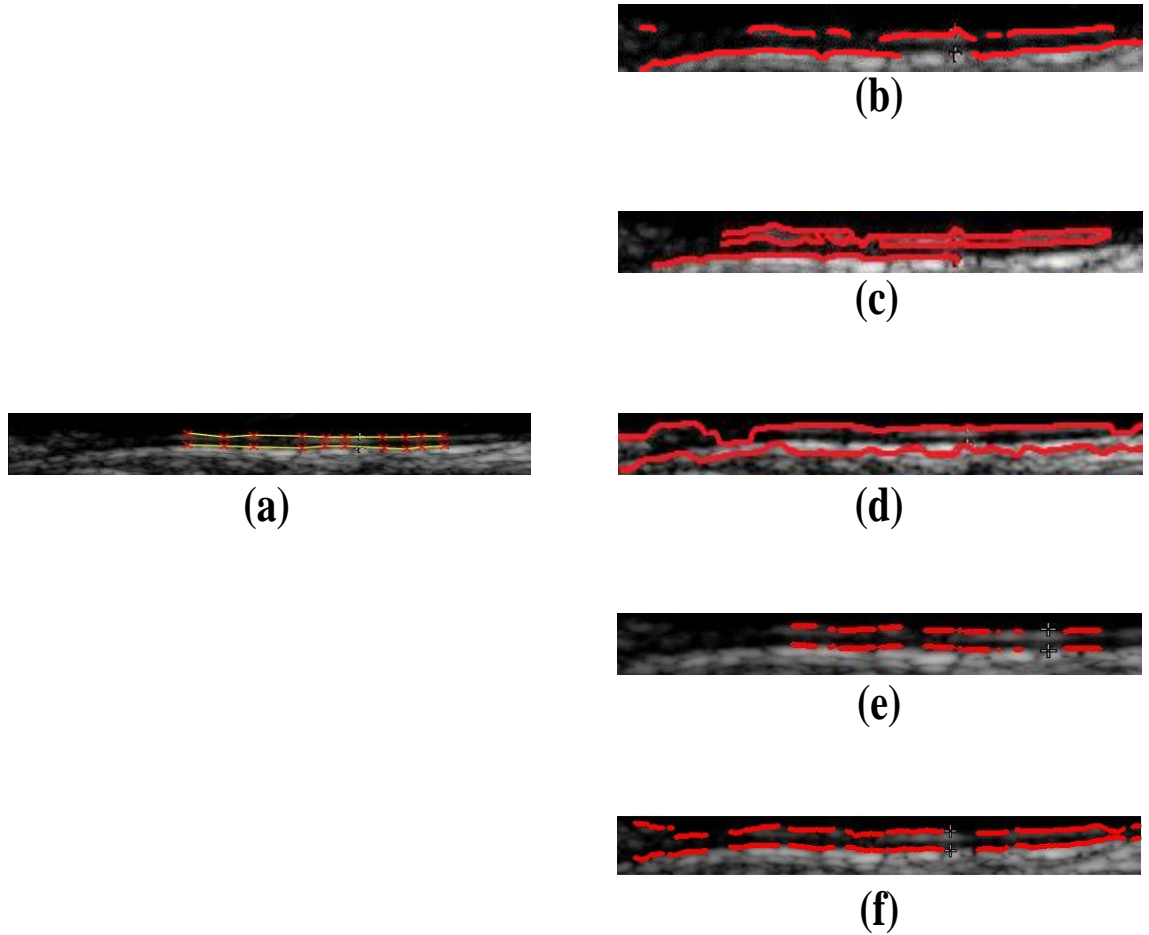
| Cross Validation | Training  | Testing   | Mean IMT  |
|------------------|-----------|-----------|-----------|
| D1               | 25 Images | 24 Images | 0.72 (mm) |
| D2               | 24 Images | 25 Images | 0.60 (mm) |

window gives selective information about the intensity values in the neighborhood central pixel. Using the window, class of the centre pixel is defined on the basis of intensity values of both centre pixel and all neighborhood pixels. The ROI is extracted for all the training and testing images. A large dataset is formed by moving the 9x9 window over all the training images. This dataset is highly imbalanced and can not be used for training purpose. Therefore, a balanced dataset is formed from this huge dataset by randomly selecting 7000 samples from all the IMT boundary pixels samples and by randomly selecting another 7000 samples from all the non-IMT boundary pixels. Finally, a balanced dataset of 14000 samples is formed. For learning process, the balanced dataset is further divided into training data(50%) and testing data(50%). The test samples are used in order to infer the model behaviour for unseen samples. The proposed method has been evaluated on the dataset using 2-fold cross validation. The dataset contains 49 images which are split into 25 training images and 24 testing images. We randomly assigned images into two sets with one set containing 25 images, named as D1 and another set containing 24 images, represented as D2. Then, we train the classifier on D1 and test it on D2, followed by training on D2 and testing on D1. The results of mean IMT of the proposed method for automatic segmentation are tabulated in the Table.4.1 and final result is obtained by taking the average of mean IMT value (D1 and D2). We can observe that every image in a total of 49 images is tested only once and the mean IMT value across two fold cross validation is found to be 0.66. Finally, the obtained IMT boundary pixels classified using the SVM model are overlapped over the ROI image and boundary pixels which joined with each other.

### 4.1.3 Results

In this section, the quantitative evaluation of the achieved segmentation results is conducted by comparing different state-of-art techniques with the proposed method. For our experiment, we used 49 carotid ultrasound images which have been taken from the Cyprus Institute Nicosia (CyprusUniversity (2007)). The state-of-art algorithms have been implemented in the MATLAB 2015a and simulated on Intel Core i7 processor with 4GB of RAM. The experimental results of the proposed technique and recent techniques are tabulated in the

Table. 4.2. The  $IMT_{mean}$  is measured from (Eq.(2.7) using mean absolute distance metrics. The proposed algorithm is compared with the existing algorithms such as DP (Li *et al.* (2014)), MB (Ilea *et al.* (2013a)), SS (Loizou *et al.* (2015)) and NN (Menchón-Lara *et al.* (2014)).



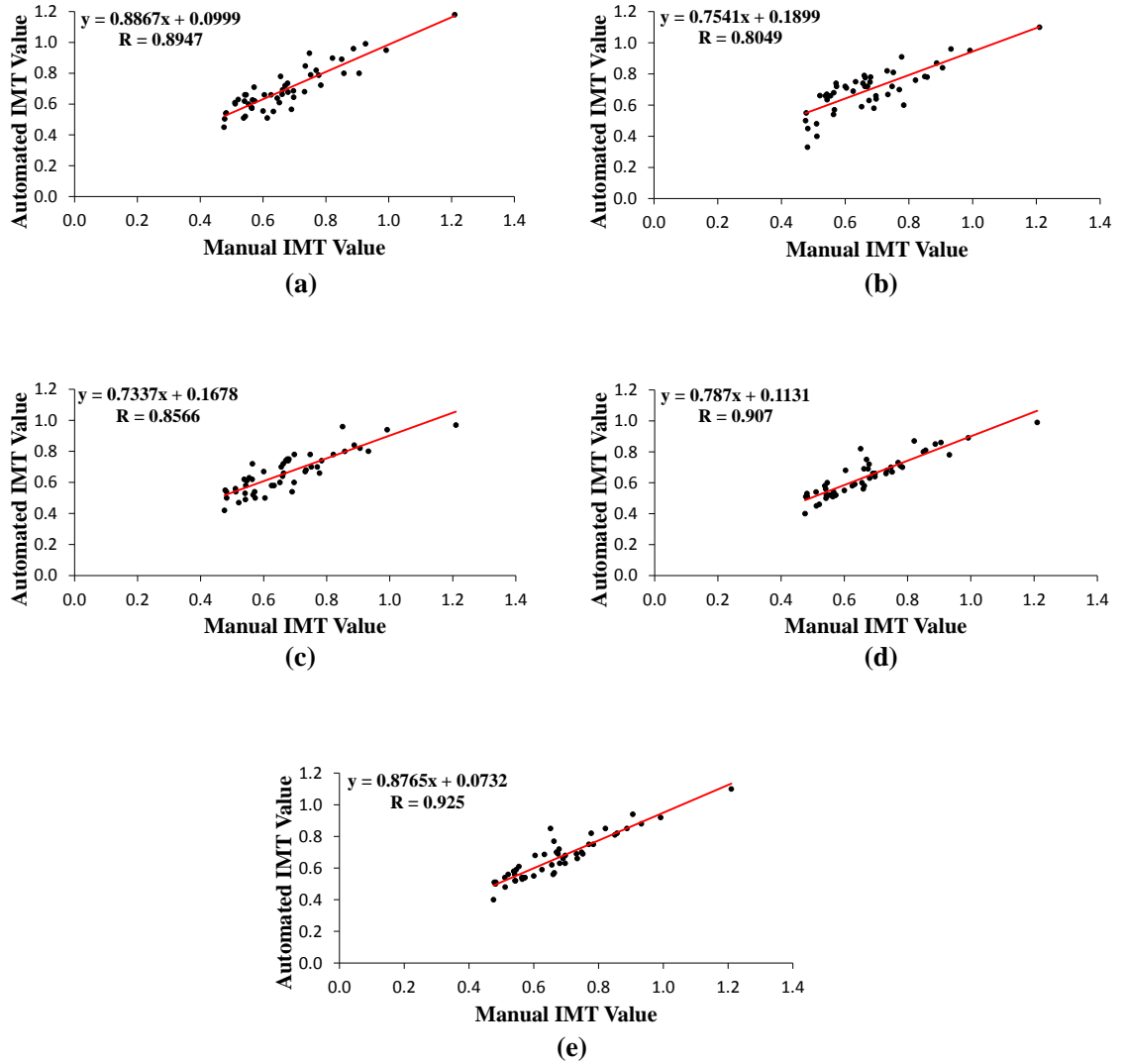
**Figure 4.3:** (a) Original longitudinal carotid ultrasound sample image with manual delineation from an expert. (b) Automated delineation using DP. (c) Automated delineation using MB. (d) Automated delineation using SS. (e) Automatic segmentation using NN. (f) Automated delineation using proposed method.

From the Table.4.2, the  $IMT_{mean} \pm std$  of proposed SVM method ( $0.69 \pm 0.19$  (mm)) is closer to the ground truth data ( $0.7068 \pm 0.1837$  (mm)) and shows superior performance in terms of accuracy compared to the DP ( $0.68 \pm 0.12$  (mm)), MB ( $0.67 \pm 0.11$  (mm)), SS ( $0.68 \pm 0.10$  (mm)) and NN ( $0.64 \pm 0.16$  (mm)). Figure 4.3 shows automated segmentation of IMT on sample images of our dataset. Figure 4.3(a) depicts the original longitudinal carotid

**Table 4.2:** Mean IMT values of automated segmentation (AS) method and the ground truth (GT) for 49 carotid ultrasound images.

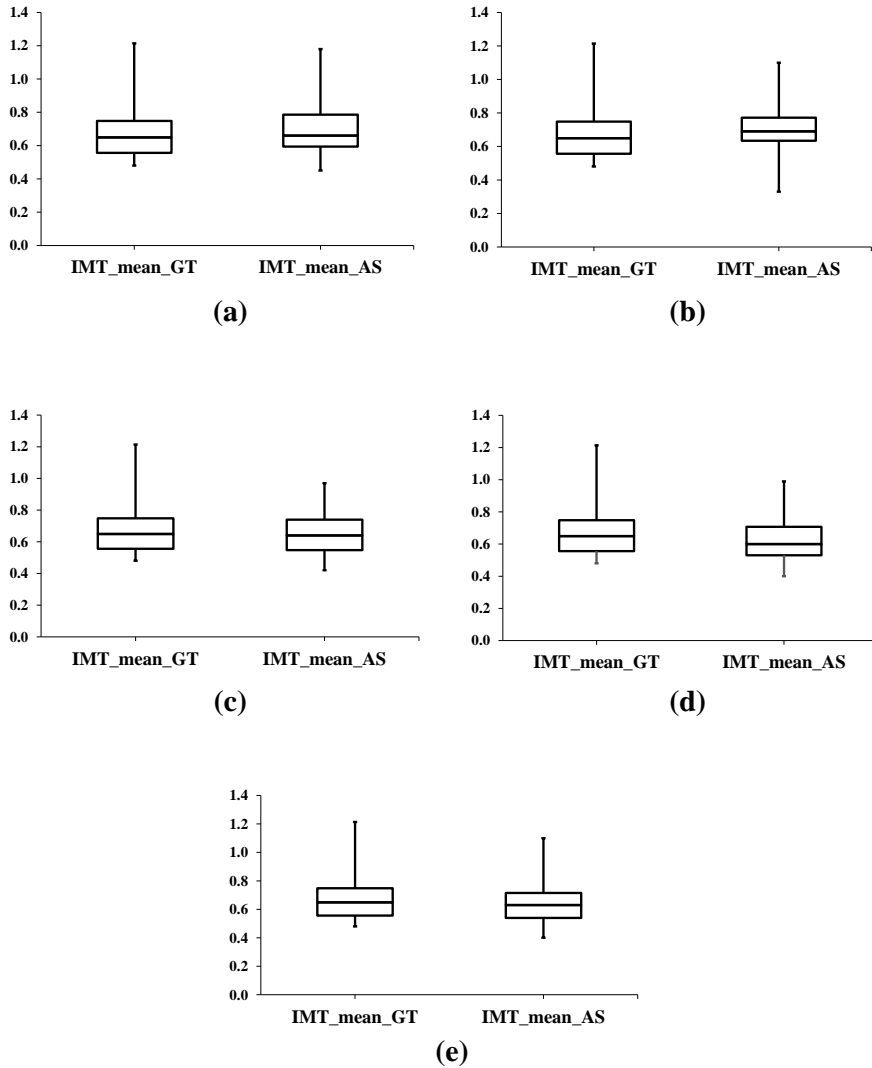
| Evaluation Metrics             | DP              | MB              | SS              | NN              | Proposed Method |
|--------------------------------|-----------------|-----------------|-----------------|-----------------|-----------------|
| $IMT_{mean} \pm std$ (mm) (GT) | $0.67 \pm 0.17$ | $0.67 \pm 0.17$ | $0.67 \pm 0.17$ | $0.67 \pm 0.17$ | $0.67 \pm 0.17$ |
| $IMT_{mean} \pm std$ (mm) (AS) | $0.69 \pm 0.13$ | $0.70 \pm 0.14$ | $0.65 \pm 0.10$ | $0.64 \pm 0.16$ | $0.66 \pm 0.12$ |
| R (refer Figure 4.4)           | 0.89            | 0.80            | 0.85            | 0.90            | 0.92            |

ultrasound sample image with manual delineation by the expert. Figure 4.3(b) illustrates the automatic detection of LI and MA boundaries based on DP and we can observe that boundaries of LI and MA are not detected properly owing to the variation in the pixel intensities. Figure 4.3(c) illustrates the detection of boundaries using MB algorithm in which the edges are not seen properly owing to the irregularities in the LI and MA borders. Similarly, Figure 4.3(d) shows the automatic detection of LI and MA boundaries based on SS method and it is observed that boundaries are not identified properly owing to the evolution of parametric curve that leads to self-interaction of the boundaries. Figure 4.3(e) presents the automatic detection of LI and MA boundaries using the Neural Network. The major limitation of the neural network is that it takes more computational time compared to the other methods. Figure 4.3(f) shows the automatic detection of LI and MA boundaries using the proposed algorithm and it is observed that segmented IMT retains the boundaries. For comparison with the proposed method, we implemented the MB algorithm, it uses  $S_{max}$ , is a parameter that sets the model variation above and below to allow the inclusion of additional information in the ROI that will be necessary in the process of IMT reconstruction. In MB (Ilea *et al.* (2013a)), for estimation of the height of ROI  $S_{max}$  is set to 15 and Gaussian kernel  $\sigma$  is set to 1.5 for adjusting the size of the Gaussian filter. In our work, we set  $S_{max}$  value as 30 and the Gaussian kernel is set to  $\sigma=1$ . In DP, the LI and MA boundaries are estimated using the histogram approach using morphological operation. The threshold  $T$ , divides the pixels in the ROI into two clusters according to the intensity of each point. In our experiment, the threshold value is set to 0.1. The morphological operations of dilation followed by erosion have been used to fill the gaps and holes in the images. The structuring element as "line", with the length of 10 pixels is used. The boundary is adjusted by DP using curve evolution formula. The weights of curvature  $\lambda$  is recommended as -0.2 but in our study we adopt -0.1. The ROI is convolved with a vertical direction first order derivative of Gaussian kernel to get the edge map, where experimental results recommended a setting of



**Figure 4.4:** Regression analysis plots comparing automated segmentation measurements with manual measurement. (a) DP (b) MB (c) SS (d) NN (e) Proposed Method.

window size  $10 \times 10$  with a standard deviation of 1 in both horizontal and vertical directions. The  $7 \times 7$  Gaussian kernel is used to achieve better results when trial and error with different sizes of kernels are performed. The SS algorithm minimizes the energy function by using external and internal energy forces. Experimental results recommend settings for the initial values  $\alpha = 0.6$ ,  $\beta = 0.4$ ,  $\gamma = 2$ . In our work, the initial values  $\alpha = 0.4$ ,  $\beta = 0.3$ ,  $\gamma = 1.5$  are chosen to start the snake deformation because these values proved to be robust in all experiments conducted in our study. For a neural network, a large imbalanced dataset is formed by moving the  $11 \times 11$  window over the training ROI images. The patterns are emphasized for



**Figure 4.5:** Box plots comparing automated segmentation measurements with manual measurement. (a) DP (b) MB (c) SS (d) NN (e) Proposed Method.

training since the dataset is large and highly imbalanced. Hence, a balanced dataset is to be formed and it consists of 8,000 samples, out of which, 4000 samples belong to the class of IMT boundary and other 4000 samples belong to the class of non-IMT boundary. For the learning purpose, the data were randomly divided into three subsets, namely, training data(50%), validation data(25%) and testing data(25%). The validation data is used for network size selection and to stop criteria. The testing data is used to infer the network behavior for new carotid ultrasound images. The prior probabilities are same for both the classes in training and testing data. The hidden layer in the network used for the training purpose consists of 20 neurons. In all these images, the segmentation algorithms are applied

**Table 4.3:** Validation(out of 5) of ultrasound carotid images from the radiology expert.

| Dataset | Manual measure | DP  | MB | SS | NN | Proposed method |
|---------|----------------|-----|----|----|----|-----------------|
| Image   | 4.5            | 3.5 | 3  | 4  | 4  | 4.75            |

and measured with the validation metrics.

Radiology expert (with experience of 5 years) evaluated the segmented IMT for the images as shown in Figure 4.3 by giving a score out of 5 and the score are depicted in Table.4.3 (0-worst,5-best). Figure 4.4 presents the regression analysis of the manual IMT values versus automated IMT values. The equation "y"(see Figure 4.4) predicts the automated segmented value based on manually measured value. The Pearson correlation coefficient (R) is calculated from Eq.(2.9), which is used to determine the strength of the relationship between automatic segmentation and ground truth measurement data. The achieved results further confirm the better performance of the proposed method over existing methods. Figure 4.5 illustrates the box plot of automatically segmented and ground truth data for 49 carotid ultrasound images. The spacing of the points between boxes shows the degree of dispersion and skewness of the data. To estimate the non-parametric significance test between the automatic and manually measured IMT values, Wilcoxon rank sum test (P-value) is applied for 49 measured images. The calculated P-value for the proposed method is 0.21, which shows that no significant difference between the automated and ground truth data measurements. Finally, we conclude that the segmentation based on SVM is desirable for clinical diagnosis of IMT, because of high agreement between automatic and manual segmentation.

## 4.2 Proposed method based on Wind Driven Optimization technique

Section 4.2 starts with a brief background of wind driven optimisation (WDO) algorithm for segmentation of IMC of the CCA. The speckle noise is reduced using OBNLM filter and  $TV - L_1$  norm is used to increase the contrast. Section 4.2.2 explores the novel automatic ROI extraction for detection of IMC boundaries in the carotid wall. In section 4.2.3, we apply a multi level otsu thresholding objective function to the extracted ROI for segmentation of IMT based on WDO algorithm. Section 4.2.4 presents the results of proposed method

and are compared with the results of state-of-the-art methods. Finally, in section 4.2.5, the experimental analysis of the proposed method and state-of-the-art methods is discussed.

### 4.2.1 Background of Wind Driven Optimization Technique

WDO is a modern algorithm inspired from nature. The word wind pertains to movement of the air in the horizontal direction, especially in the lower layer of the earth atmosphere. WDO is a populace based iterative heuristic global optimization algorithm (Bayraktar *et al.*,2013) that can be applied for multi-modal and multi-dimensional problems. The WDO algorithm employs terms that are based on gravitation, pressure gradient, friction and Coriolis forces. The four forces provide robustness, extra degrees of freedom to fine tune and ability to impose constraints on search space. In the atmosphere, temperature variations at different locations create different air pressures and densities at different locations (Thompson,1998). The variation in the temperature horizontal deviation in air pressure cause the air to moves from a high-pressure area to a low-pressure area at a velocity, which is relative to a pressure gradient. The WDO algorithm is formulated with some assumption and simplification. The starting point of WDO is influenced by Newtons second law of motion, which gives proper results when applied to atmospheric motion analysis (Ahrens,2012). The law of motion states that the total force applied on it causes the air parcel to accelerate with an acceleration of  $\alpha$  and the direction of acceleration is same as that of force applied as given by (Bayraktar *et al.*,2013):

$$\rho\alpha = \sum F_{ind} \quad (4.3)$$

Here  $\rho$  denotes the density of the infinitesimally small air parcel and  $F_{ind}$  denotes individual forces acting on the air parcel. Ideal gas law provides the relation between density ( $\rho$ ) and the Pressure ( $P$ ) as follows(Bayraktar *et al.*,2013):

$$P = \rho RT \quad (4.4)$$

where  $P$  denotes the pressure,  $R$  is ideal gas constant and  $T$  is the absolute temperature of the air. For simplicity,  $H$  is used as a product of  $R$  and  $T$ .

The total of four forces enclosed in Eq.(4.3) that initiates the air parcels motion in a specific direction at a certain velocity. The velocity with which the movement takes place is directly proportional to the pressure gradient. The pressure gradient ( $P$ ) is calculated as

the pressure difference between the two locations and is given by(Bayraktar *et al.*,2013):

$$F_{pressure} = -\Delta P\delta V \quad (4.5)$$

where  $\delta V$  represents the finite volume of the air parcel and  $F_{pressure}$  represents the force due to the pressure gradient. Here the negative sign signifies descending direction.

The wind is influenced by several forces out of which the friction force  $F_{friction}$  plays an important role. The magnitude of the force is directly proportional to the velocity of the parcel, but it opposes the motion of the particle. The frictional force is governed by the following equation:

$$F_{friction} = -\mu\rho u \quad (4.6)$$

where  $\mu$  is the coefficient of friction and  $u$  is the velocity of the particle. Another important force that acts on an air parcel is the gravitational force (Ahrens,2012). The gravitational force is proportional to the mass of the parcel which in turn is equal to the product of the density and the volume of the parcel. The gravitational force is given by:

$$F_{gravity} = \rho\delta Vg \quad (4.7)$$

where  $g$  is the acceleration due to gravity. A major force that affects the wind is the Coriolis force, which is caused due to the rotation of the earth and defined by the following equation:

$$F_{coriolis} = -2\Omega \times u \quad (4.8)$$

where  $\Omega$  represents the rotation of the earth and  $u$  velocity of the wind. According to the Newtons second law of motion given in Eq.(4.3), which can be rewritten as(Bayraktar *et al.*,2013):

$$\rho \frac{\Delta u}{\Delta t} = \rho\delta Vg - \Delta P\delta V - \mu\rho u - 2\Omega \times u \quad (4.9)$$

For simplicity acceleration term written as  $a = \frac{\Delta u}{\Delta t}$ , a time step  $\Delta t = 1$  and replace  $\rho$  with  $\frac{P}{H}$ . For an infinitesimally small, dimensionless air parcel, we set  $\delta V = 1$ , which simplifies the Eq.4.9 to (Bayraktar *et al.*,2013):

$$\Delta u = g - \Delta P \frac{H}{P_{curr}} - \mu u - \left( \frac{2\Omega \times uH}{P_{curr}} \right) \quad (4.10)$$

Consider  $\Delta u$  as  $u_{next} - u_{curr}$ , where  $u_{curr}$  is the velocity in the current iteration and  $u_{next}$  is the



velocity in the next iteration. The gravitational force is always directed towards the centre of the Earth. The force is directed towards the origin from the current position is taken as:

$$g = |g|(0 - l_{curr}) \quad (4.11)$$

Pressure gradient is calculated as the difference in the pressure at current location of an air parcel and the optimum pressure and the direction is from the current location to the optimum location ( $l_{opt}$ ). Hence, the pressure gradient is:

$$\Delta P = |P_{opt} - P_{curr}|(l_{opt} - l_{curr}) \quad (4.12)$$

where  $P_{opt}$  is the optimum pressure value,  $P_{curr}$  is pressure of the air parcel at the current location,  $l_{opt}$  is location of the air parcel and  $l_{curr}$  is the position of the air parcel with optimum pressure. The Eq.4.10 can be arranged as:

$$u_{next} = (1 - \mu)u_{curr} - gl_{curr} + (H)\left(\frac{P_{opt}}{P_{curr}} - 1\right)(l_{opt} - l_{curr}) + C\frac{u_{perp}}{P_{curr}} \quad (4.13)$$

where C is  $-2|\Omega|H$ ,  $u_{next}$  is the updated velocity,  $u_{curr}$  is current velocity of air parcel and  $u_{perp}$  is the velocity of the same air parcel but taken in another dimension which is chosen randomly. The values of the pressure are explicitly used in the Eq.4.13. This leads to a problem where the next velocity may become too high, because of the pressure values especially the objective function values in our context. In order to avoid that, this method follows a ranking system where air parcels with best pressure are given a rank ( $r$ ) = 1 and the air parcel with second best pressure is given a rank of 2 and so on. The Eq.4.13 when ranks are used can be written as (Bayraktar *et al.*,2013):

$$u_{next} = (1 - \mu)u_{curr} - gl_{curr} + (H)\left(\frac{1}{r} - 1\right)(l_{opt} - l_{curr}) + c\frac{u_{perp}}{r} \quad (4.14)$$

Here ranking system is used instead of directly using the pressure values,  $u_{next}$  obtained can sometimes go to very high or low values which results in some values being skipped out of the search space. To prevent that, the  $u_{next}$  velocities are limited to specific maximum ( $u_{max}$ ) and minimum ( $u_{min}$ ) values:

$$u_{next} = \begin{cases} u_{max}, & \text{if } u_{next} > u_{max} \\ -u_{max}, & \text{if } u_{next} < -u_{max} \end{cases} \quad (4.15)$$

The new position can be found as:

$$l_{next} = l_{curr} + u_{next} \quad (4.16)$$

Even when the velocities are limited, the positions of the particles may exceed the limits of search space. The new position of the particles prevented by limiting  $l_{next}$  between  $l_{max}$  and 0.

$$l_{next} = \begin{cases} l_{max}, & \text{if } l_{next} > l_{max} \\ 0, & \text{if } l_{next} < 0 \end{cases} \quad (4.17)$$

## 4.2.2 Proposed Methodology

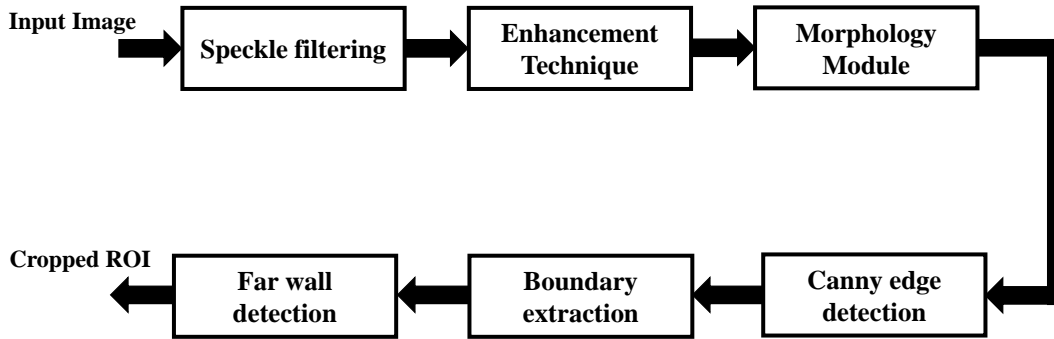
### (a) Ultrasound Image Data Acquisition

We used two different datasets: dataset 1 and dataset 2. Dataset 1 consisted of 100 images collected from the Cyprus Institute of Neurology of Nicosia (CyprusUniversity (2007)); of these images, 65 were used for this experiment and the remaining 35 were neglected because of their poor visual quality. The images were acquired using an ATL HDI-3000 ultrasound machine used with a linear probe with a frequency range of 4-7 MHz. The Dataset 2 consisted of 25 images collected from the Father Muller Medical College Hospital, Mangalore, India. These images were acquired using a Philips HD-11 XE ultrasound scanner covering a frequency range of 7-12 MHz. Total Ninety B-mode longitudinal images were used for the performance evaluation of the proposed and existing methods. The images from dataset 1 were captured with a resolution of  $768 \times 576$  pixels, whereas those of dataset 2 were recorded with a resolution of  $800 \times 564$  with 256 gray levels, and the images were re-sampled at a standard density of 16.62 pixels/mm. Textual marks were removed in order to facilitate the smooth processing, and the original ultrasound images were automatically cropped into a size of  $395 \times 295$  pixels.

### (b) Automatic Extraction of the ROI

In ultrasound images, because of the speckle noise, the quality of the images is degraded and the contrast is reduced. The speckle present in an ultrasound image is reduced using an OBNLM filter ( Coupé *et al.* (2009)). The image is then enhanced by the TV-  $L^1$  norm( Ghita *et al.* (2013)) using a histogram equalization technique. The overall block diagram of the automatic ROI extraction method is shown in Figure 4.6 and each block is explained as follows.

- **Speckle Filtering Technique:**



**Figure 4.6:** Outline of ROI extraction.

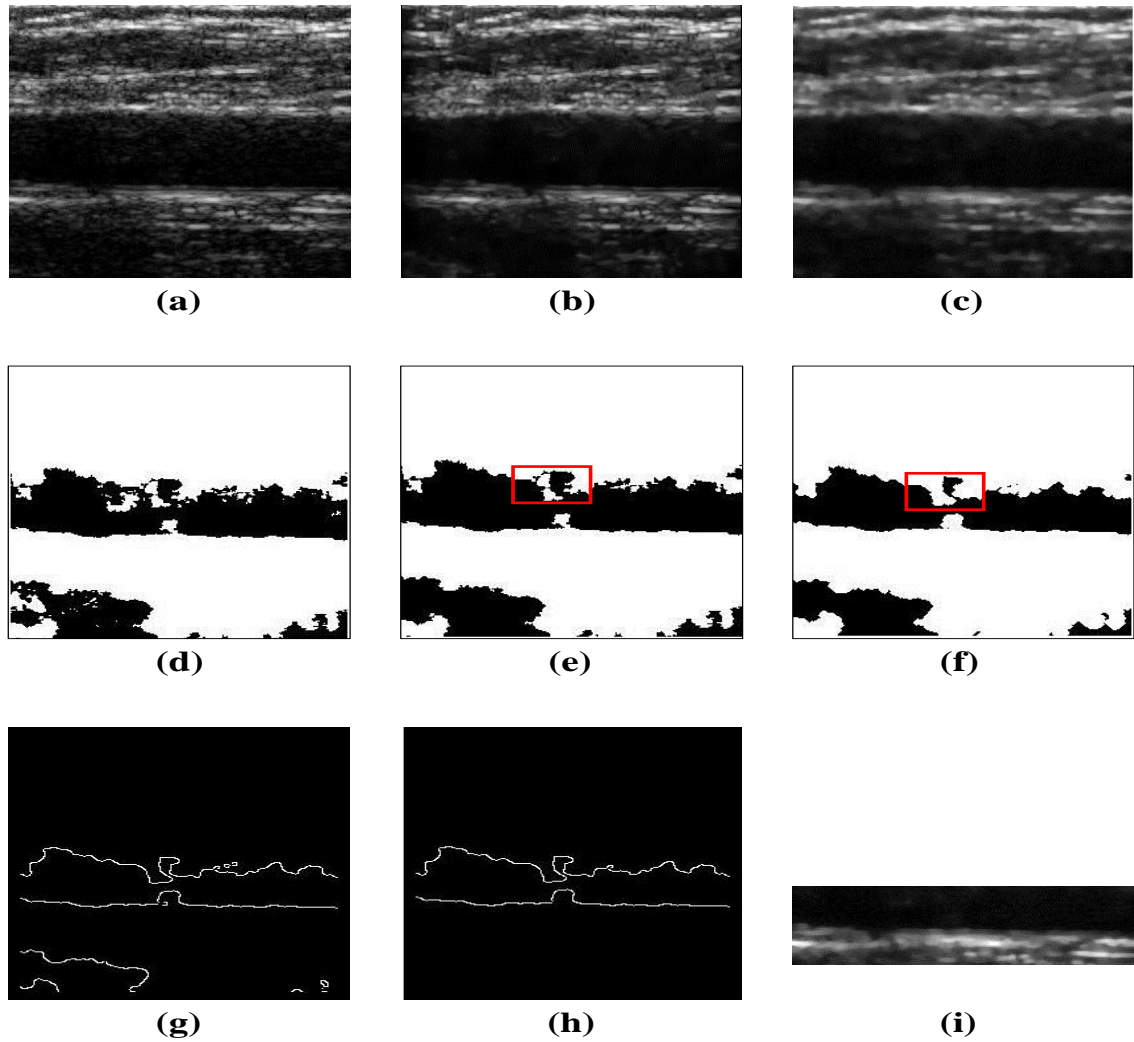
Carotid ultrasound images are affected by speckle noise, which degrades their quality. The OBNLM filter suppresses the multiplicative noise by the effective utilization of the optimally tuned parameters of grayscale images. This filter is an extension of the NLM filter, in which the image pixels are restored by a weighted average of the pixels of the non-local neighbourhood pixels. An example of a despeckling image is shown in Figure 4.7(b).

- **Image Enhancement:**

The contrast enhancement (Zhang *et al.* (2014)) technique improves the visual appearance of an image by changing the pixel intensity of the original image. The main objective of the enhancement is to process an image so that the resultant image contains more relevant information than that of the original image. In this work,  $TV-L^1$  norm (Ghita *et al.* (2013)) model was used for the enhancement by applying a histogram warping process. Figure 4.7(c) shows an enhanced image using this model.

- **Morphology Operation:**

Morphological functions are used to clean the edges which are generated by a binary process (see Figure 4.7(d)). A morphological opening function is applied to eliminate the gaps and fill the holes in the plaque contour, and various structuring elements can be used to close the contour (Gonzalez and Woods (2004)). In this experiment, a morphological area opening with a larger size was used to remove the smaller objects, which can be seen in Figure 4.7(e). Because of the area opening, there was a possibility of breakage in the plaque contour. To overcome this problem, we used dilation with a structuring element of disk size 2 to seal the plaque contour. As can be seen in the bounded box in Figure 4.7(f), the near wall of the carotid artery was



**Figure 4.7:** Automatic extraction of ROI. (a) Original carotid longitudinal ultrasound image. (b) De-speckled image using OBNLM filter. (c) Enhancement using TV-  $L^1$  norm. (d) Conversion of the binary image with automatic thresholding procedure. (e) Area opening for removing small objects. (f) Dilation for to seal the plaque contour. (g) Canny edge detection. (h) Extraction of the near and Far wall. (i) Automatic ROI extraction.

sealed because of the dilation operation. A similar sealing effect can be seen on the far wall; hence, we could easily extract the near wall and the far wall when we applied a Canny edge detector.

- **Canny Edge Detection:**

Canny operators (Bao *et al.* (2005)) smooth the data by means of Gaussian convolution and then perform the edge detection operation. This operation provides an

accurate representation of the true edges of the artery while helping to eliminate the creation of false lines due to speckle noise in the image. The Canny operator yields an input grayscale image and creates an output image showing the position of tracked intensity discontinuities. Figure 4.7(h) shows the detection of edges using the Canny operator.

- **Boundary Extraction:**

The near-wall and far-wall boundaries are extracted by searching for a random point in the lumen region using the minimum sum of the column spanning index. The random point is moved upward and downward until the high-intensity gray-scale value(255) is found. With this value, the near-wall and far-wall boundaries are extracted based on the region properties (Regionprop (2002)). The extracted boundaries are shown in Figure 4.7(g).

- **Far Wall Detection:**

In a carotid ultrasound image, the IMT is estimated at the far-wall region because measuring it at the far wall is more reliable than that performed at the near wall. Once we located the random point on the far-wall line, a region covering 30 pixels upward and 30 pixels downward was extracted. Finally, the ROI was cropped for further segmentation, as shown in Figure 4.7(i).

### (c) **Segmentation Based on Otsu Thresholding Method**

Threshold-based segmentation is the simplest method for image segmentation and is an effective way of partitioning the foreground and background regions. In this work study, we used the Otsu's objective function, which is a thresholding-based image segmentation method that uses the inter-class variance to identify the optimal threshold. In our experimental analysis, Otsu's objective function for multilevel thresholding was employed for the segmentation of the IMC using the WDO algorithm. Otsu's method enables easy computation and takes considerably less time compared to the existing thresholding methods. This threshold-based segmentation method was applied to the ROI. In our experiment, the carotid ultrasound images were segmented using three different thresholds ( $L = 3$ ), thereby segmenting the images into four classes. However, finding the threshold values was an exhaustive problem. The objective function (Otsu's function) had to be computed for each value of the threshold and the one that yielded the maximum objective function value had

to be considered as the optimum threshold. It was computationally inefficient as all values from 0 to L (255) had to be calculated. To overcome this problem, we used multilevel thresholding for the segmentation to measure the IMT using Otsu's function. Otsu's objective function for the multilevel thresholding problem is given as Otsu (1975):

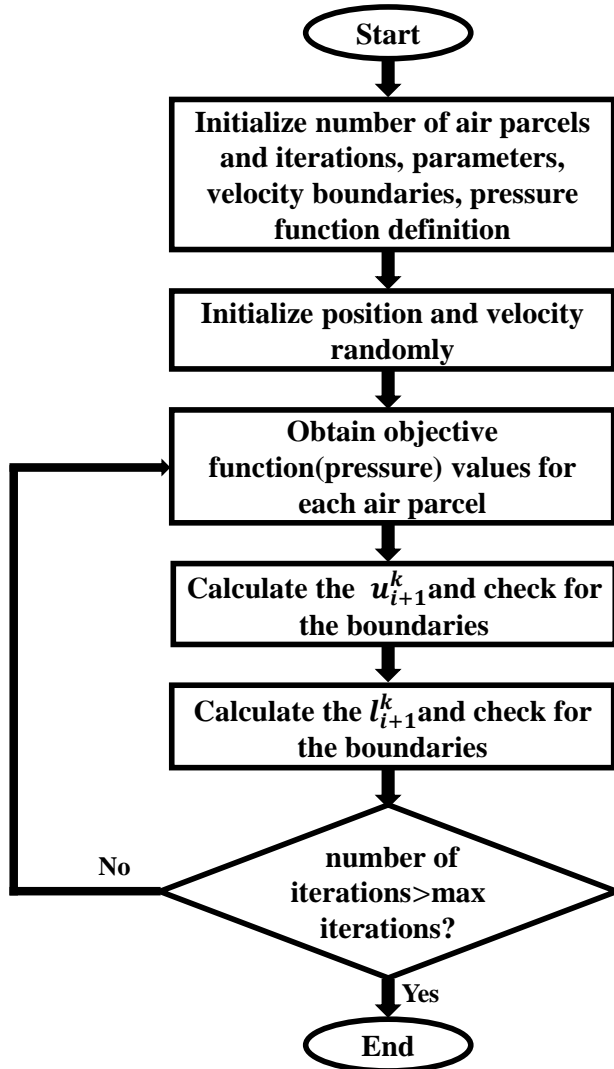
$$ot(t) = \sum_{i=0}^{L-1} \sigma_i \quad (4.18)$$

where, L represents the number of thresholds,  $\sigma_i = \omega_i(m_i - m_T)^2$  represents the multi class variance,  $\omega_i = \sum_{i=t_j}^{t_{j+1}} p(i)$  represents the probability of pixels in multi-classes,  $t_j$  is the  $j^{th}$  threshold value,  $m_T = \sum_{i=0}^{L-1} ip(i)$  is the mean intensity of the image, and  $m_i = \sum_{i=t_j}^{t_{j+1}} \frac{ip(i)}{\omega_i}$  is the mean intensity of the  $j^{th}$  class. The values of  $t_j$ , which maximizes  $ot(t)$  as in Eq.(4.18) were considered as optimum threshold values. Several optimization techniques are available that improve the computational efficiency of the problem of finding the optimum threshold values. Among all optimization techniques, the WDO algorithm was used in the experimental analysis as it provides better results compared to the existing optimization techniques.

### 4.2.3 WDO for the Optimization of Otsu's Function

This work proposes to use the WDO technique for the estimation of the IMT based on Otsu's thresholding technique. The WDO algorithm is an iterative heuristic algorithm, which has advantage such as reduction of the computational time required for the problem by limiting the maximum number of iterations and the size of each iteration and by setting boundaries for the solutions. The step-by-step process of the WDO algorithm is depicted in the flow chart shown in Figure 4.8. The WDO algorithm starts with the initialization of the parameters which are related to the optimization of the objective function (Eq.(4.18)) such as the number of air parcels, number of iterations, RT, g,  $\mu$ , C co-efficients, velocity boundaries, number of thresholds(L) and the parameters used in this experiment, which are tabulated in Table.4.4. The population of the air parcels and the velocities are assigned randomly after the optimization parameters are built up. In the next step, the pressure (objective) function values of each air parcel with its current position are evaluated. The population is ranked on the basis of the measured pressure values, and all the particle velocities are updated from Eq.(4.16), and these are restricted according to Eq.(4.17).

Each particle in the population is assigned a new position  $l_{i+1}^k$  in the next iteration according to Eq.(4.18), and the new positions are prevented from the search space by utilizing



**Figure 4.8:** Flowchart of WDO implementation.

Eq.(4.17). Pressures are calculated for the air parcels at their new positions after updating these positions. The above procedure is iterated until the maximum number of iterations is reached. In the final stage, the position of the parcel with the best(maximum) pressure at the end of the last iteration is noted as the best solution for the problem.

#### 4.2.4 Results

In this section, the experimental results obtained using the various segmentation algorithms on carotid ultrasound images are presented. In this experiment, 90 carotid ultrasound images

**Table 4.4:** Parameters used for the WDO:

| Parameter                          | Value |
|------------------------------------|-------|
| Population size                    | 20    |
| L - Number of threshold level      | 3     |
| Maximum number of iterations       | 200   |
| RT Coefficients                    | 3     |
| g - Gravitational Constant         | 0.2   |
| $\mu$ - Coefficient of friction    | 0.4   |
| C - Constant in Coriolis effect    | 0.4   |
| $u_{max}$ - maximum velocity       | 70    |
| $l_{max}$ - maximum position value | 255   |

were used for the IMT measurement. The segmentation algorithms were implemented in MATLAB version 2015a and tested on a machine with an Intel Core i7 processor and 2 GB of RAM. The performance of the proposed threshold-based segmentation using the WDO algorithm was compared with those of the existing algorithms such as MB algorithm (Ilea *et al.* (2013a)), DP algorithm (Li *et al.* (2014)), and SS (Loizou *et al.* (2014)) algorithm. From Table.4.5, we can see that the  $IMT_{mean} \pm std$  for WDO is  $(0.690 \pm 0.210 \text{ mm})$ , which is closer to the ground truth data  $(0.704 \pm 0.216 \text{ mm})$ . This shows the superior performance of the proposed method in terms of accuracy when compared with the MB  $(0.739 \pm 0.187 \text{ mm})$ , DP  $(0.728 \pm 0.189 \text{ mm})$ , and SS  $(0.713 \pm 0.206 \text{ mm})$  algorithms. The  $IMT_{mean}$  was measured from Eq.(2.7) using the MAD metrics. The IOE was estimated from Eq.(2.11) using the standard deviation of each measurement and provided the differences in the interpretation between the manual and the automated measurement. The Pearson R value was calculated from Eq.(2.9) which was used to determine the strength of the relationship between the automatic segmentation measurement data and the corresponding ground truth data. The R value (as seen in Figure 4.13) of the proposed method was 0.98 which was higher than that of the MB(0.90), DP (0.94), and SS (0.95) algorithms. The CV estimated from Eq.(2.10) and by the proposed method (21.4%) was very close to the manually measured CV (21.5%) and it shows the amount of variability relative to the mean for both cases are almost same. The CV of the MB(17.8%), DP(18.2%), and SS(20.3%) algorithms was not closer to the manual measurement. Hence, the amount of variability relative to the mean was far away from the ground truth. The  $IMT_{mean}$  values of the proposed method were closer to the ground truth data and R value was higher compared to that of the existing techniques.

Figure 4.9 shows the automated segmentation of the IMT on a sample image on dataset

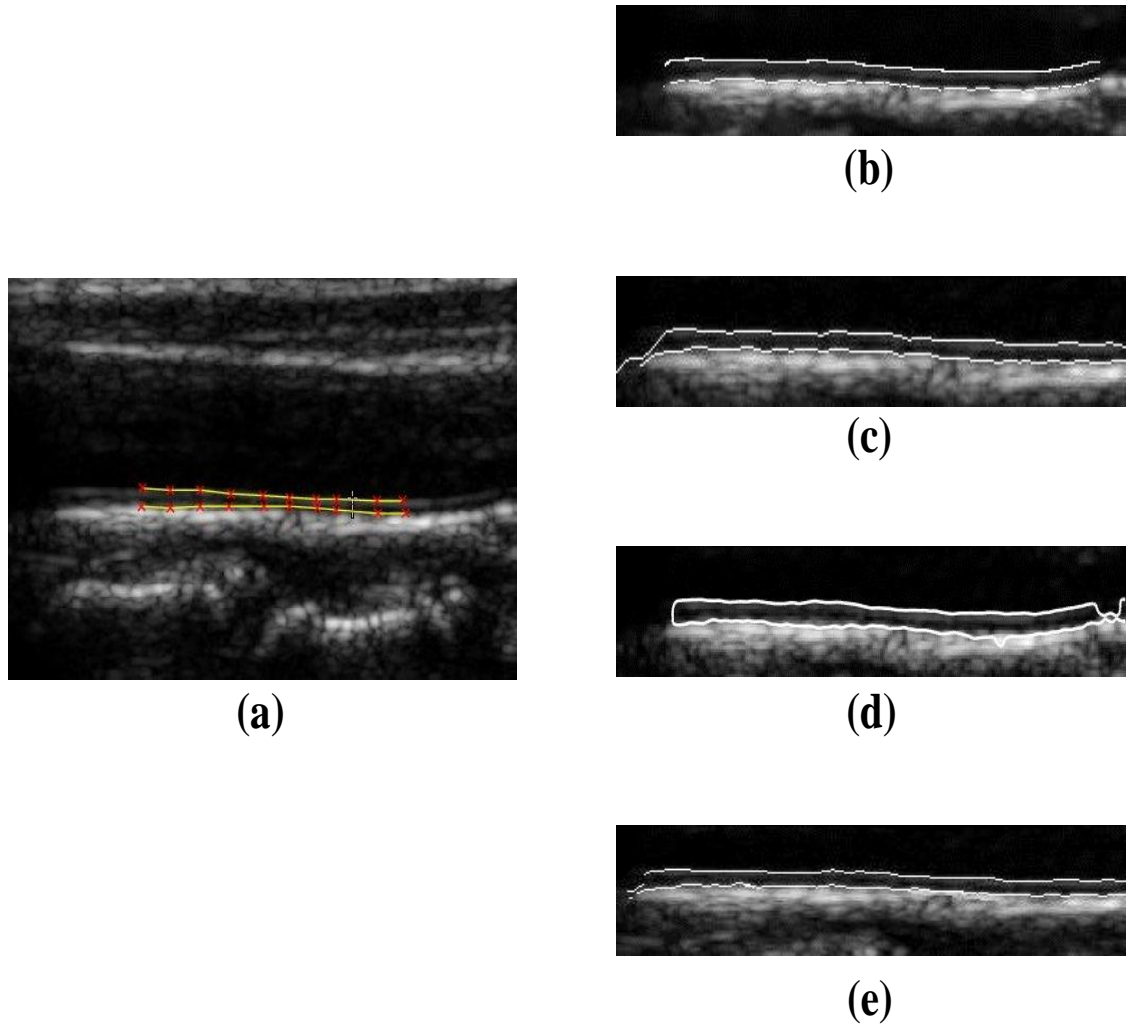


**Table 4.5:** Mean IMT values, R-correlation co-efficient, IOE-intra observer error, CV-coefficient variation and mean bias of automated method and the ground truth for 90 carotid ultrasound images.

| Validation Measures       | Ground Truth     | MB               | DP               | SS               | Proposed Method  |
|---------------------------|------------------|------------------|------------------|------------------|------------------|
| $IMT_{mean} \pm std$ (mm) | 0.704±0.216 (mm) | 0.739±0.187 (mm) | 0.728±0.189 (mm) | 0.713±0.206 (mm) | 0.690±0.210 (mm) |
| IOE                       | 0.152            | 0.132            | 0.133            | 0.145            | 0.148            |
| CV%                       | 21.5             | 17.8             | 18.2             | 20.3             | 21.4             |
| R(refer Fig.4.13)         | -                | 0.9075           | 0.9403           | 0.9571           | 0.9829           |
| Bias(refer Fig.4.11)      | -                | -0.03            | -0.02            | -0.01            | 0.01             |

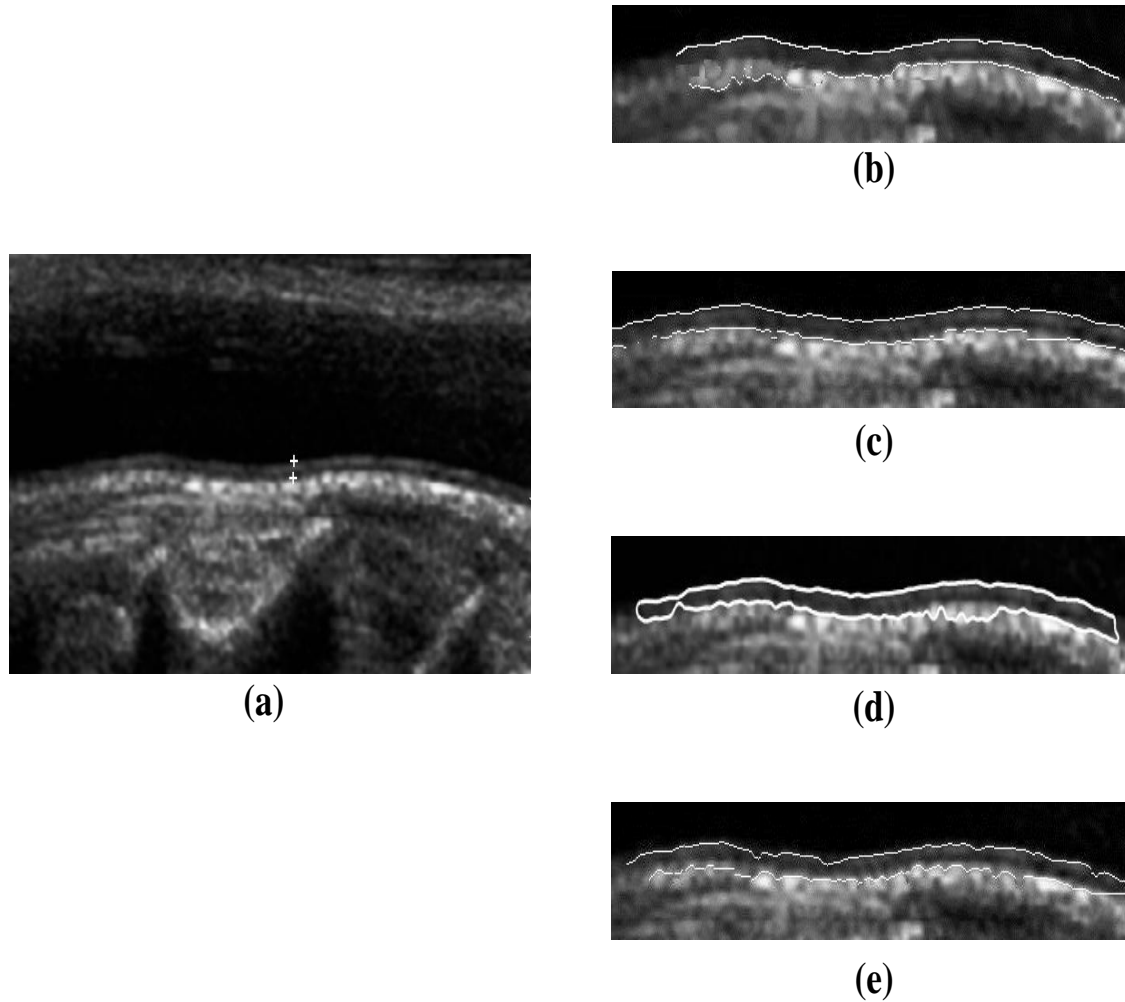
1. Figure (4.9(a)) depicts the original longitudinal carotid ultrasound sample image with manual delineation by an expert. The automatic detection of the LI and MA boundaries using the MB algorithm is illustrated in Figure (4.9(b)). It can be observed that, with the MB algorithm, the edges of the LI and MA boundaries were not properly detected owing to the irregularities in these boundaries. Similarly, Figure (4.9(c)) and Figure (4.9(d)) show the automatic detection of the LI and MA boundaries based on the DP and SS methods, respectively. In DP approach, owing to the variation in the pixel intensities, the detection of the LI and MA interfaces was not proper whereas in the SS owing to the evolution of the parametric curve, the detection leads to self-interaction and instabilities in the LI and MA boundaries. Figure (4.9(e)) presents the automatic detection of the LI and MA boundaries using the proposed algorithm. It was observed that the LI and MA boundaries preserved the edges and that the estimation of the IMT was robust. Similarly, the IMC was segmented automatically for the longitudinal carotid ultrasound sample image of dataset 2 using the proposed as well as the existing algorithms, as shown in Figure 4.10.

The Bland-Altman plot in Figure 4.11 shows the mean IMT versus the IMT difference values between the automatic segmentation and the ground truth, and it is recommended that 95% of the data points should lie within the  $\pm 2$  SD of the mean difference; otherwise, they are considered as outliers. The mean bias(0.01 mm; see Figure 4.11) of the proposed method was the smallest compared to that of the existing methods, which shows that the IMT computed by the existing techniques was more likely to be thicker than that manually measured by an expert. The negative IMT measurement bias of the MB (-0.03), DP(-0.02), and SS (-0.01) algorithms shows that the computer based methods underesti-



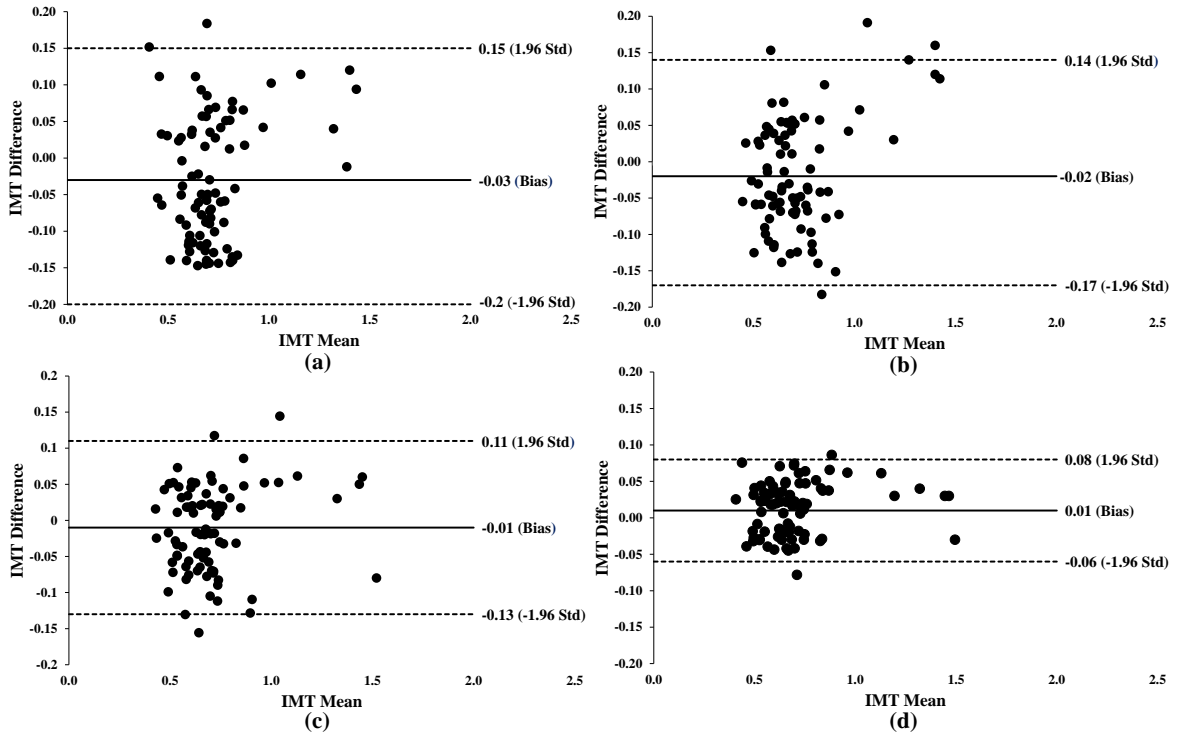
**Figure 4.9:** (a) Original longitudinal carotid ultrasound sample image of Dataset1 with manual delineation from an expert. (b) Automated delineation using Model-based approach. (c) Automated delineation using Dynamic programming. (d) Automated delineation using Snake contour. (e) Automated delineation using proposed method.

mated the IMT. Figure 4.12 illustrates the box plot of the mean values of the MB, DP, SS, and of the proposed method calculated for all 90 carotid ultrasound images for the automatically segmented and ground truth data. The interquartile range (IQR) was estimated in the box plot to measure the statistical dispersion based on the partition of the dataset into an upper quartile and a lower quartile. The calculated IQR values of the MB(0.14mm), DP (0.19mm), SS (0.17mm) and proposed method (0.17mm) with respect to the ground truth data(0.18mm) show that the proposed method achieved comparable results with the



**Figure 4.10:** (a) Original longitudinal carotid ultrasound sample image of Dataset2 with manual delineation from an expert. (b) Automated delineation using MB approach. (c) Automated delineation using DP. (d) Automated delineation using SS approach. (e) Automated delineation using proposed method.

state-of-the-art techniques. Figure 4.13 presents the regression analysis of the manual IMT values versus the automated IMT values. In the equation,  $y$  (see Figure 4.13) predicts the automated segmented value based on manually measured value and  $R$  measures the strength of the linear association between the two measurements. To estimate the non-parametric significance test between the automatic and the manually measured IMT values, we applied the Wilcoxon rank sum test (P-value) (Oyeka and Ebuh (2012)) to the 90 measured images. The calculated P-value for the proposed method was 0.28, which shows that there was no

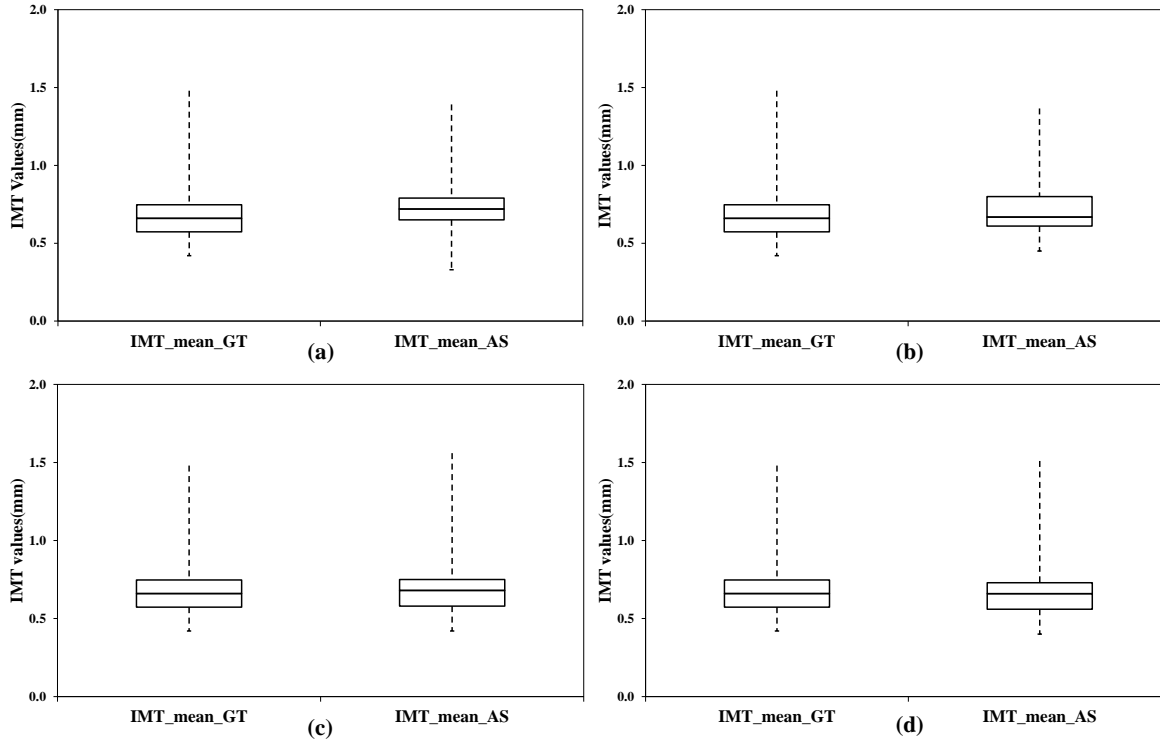


**Figure 4.11:** Bland Altman plots of the mean against the difference in the IMT mean values estimated for 90 carotid ultrasound images (automatic segmentation corresponding to the ground truth data). a) MB b) DP c) SS d) Proposed Method.

significant difference between the automated and the ground truth data measurement (any  $p > 0.05$  indicates that there was no significant deviation between the automated and the ground truth data measurement).

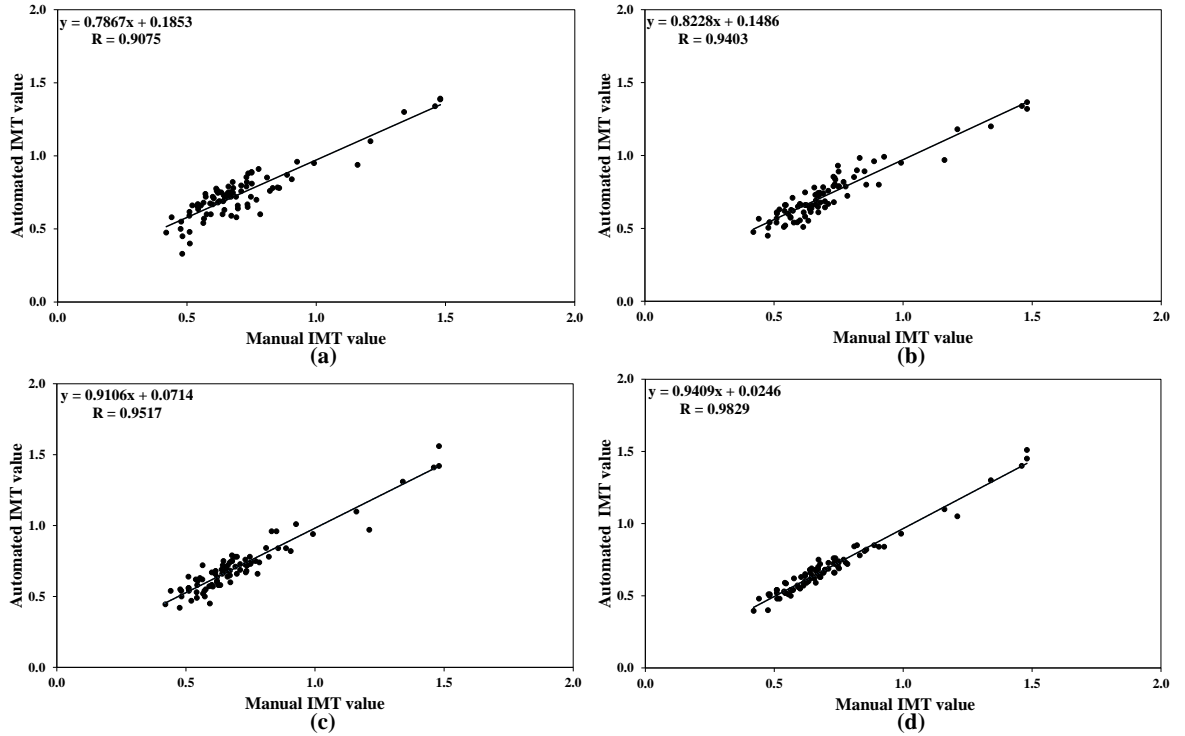
## 4.2.5 Discussion

The aim of this study was to automatically measure the IMT in carotid ultrasound images by the effective utilization of threshold-based segmentation using the WDO method. The experimental analysis described in the previous section shows that the proposed automatic IMT segmentation yielded better results compared to other existing techniques. Our approach was compared with some of the existing methods such as MB method, DP method, and SS method. The MB algorithm used the statistical vascular model to estimate the LI and MA boundaries from which the IMT was measured without any user interaction. In the MB approach, for the height of the ROI estimation,  $S_{max}$  was set to 15 and the scale  $\sigma$  was used to adjust the size of the Gaussian filter. The initial edge detection was executed when the



**Figure 4.12:** The mean intima-media thickness calculated for the database of 90 carotid ultrasound images for the automatic segmentation (IMT\_mean\_AS) and ground truth data (IMT\_mean\_GT). a) MB b) DP c) SS d) Proposed Method.

scale of the Gaussian kernel was set to  $\sigma=1.5$ . In our experiment, the  $S_{max}$  value was set to 30 and the Gaussian kernel  $\sigma=1$  was chosen for better measurement of the IMT interfaces. The ROI was extracted using the proposed method before applying the DP algorithm. The LI and MA boundaries were estimated using the histogram approach employing a morphological operation. In our experiment, the  $T_1$  threshold was taken as the first valley point of the histogram of the respective image, as recommended. The morphological operations include dilation followed by erosion which were used to fill the gaps and holes in the images. In our experiment, a structuring element of line type was chosen, which had a length of 10, although the experimental result recommended the size of the structuring element to be 15. The boundary was adjusted by DP using a curve evolution formula and the recommended value of the weight of curvature ( $\lambda$ ) was -0.2. However, in our study, -0.1 was used for better accuracy. The ROI was convolved with a vertical directional first order derivative of the Gaussian kernel to obtain the edge map, where experimental results recommended a setting of  $10 \times 10$  with a standard deviation of 1 in both the horizontal and the vertical directions. The Gaussian kernel of size  $7 \times 7$  was found to offer better results after trial and error with



**Figure 4.13:** Regression analysis plots comparing automated segmentation measurements with manual measurement. a) MB b) DP c) SS d) Proposed Method.

different sizes of the kernels. The SS algorithm minimizes the energy function by using external forces and has a number of visual problems such as edge detection, lines, and subjective contours. For the measurement of the snake parameters  $\alpha$  and  $\beta$ , we considered the irregular spacing between the snake contour points. Experimental results recommended the following settings for the initial values  $\alpha = 0.6$ ,  $\beta = 0.4$ , and  $\gamma = 2$ . In our work, the initial values of  $\alpha = 0.4$ ,  $\beta = 0.3$ ,  $\gamma = 1.5$ , step size = 1, and iterations = 100 were chosen to start the snake deformation because these values proved robust in all experiments conducted in our study. The optimal performance of WDO was achieved by properly choosing the values of various coefficients: RT, g, C and  $\mu$ . In Eq.(4.14), the friction co-efficient( $\mu$ ) and the gravitational force co-efficient(g) were varied in the range [0, 1]. However, RT and C could be varied to a larger extent and were allowed to vary in the range [0, 5] during the observation. The friction co-efficient  $\mu$  was set to 0.4, whereas the RT and C values were chosen as 3 and 0.4, respectively, for the experiment. For each trial, a population size of 20 air parcels was optimized for a maximum of 200 iterations, and  $u_{max}$  was set to 70. Because, the next velocity ( $u_{next}$ ) was directly dependent on the product of the gravitational force constant(g) and the

**Table 4.6:** Validation(out of 5) of ultrasound carotid images from the radiology expert.

| Images    | Manual measure | MB  | DP   | SS   | Proposed method |
|-----------|----------------|-----|------|------|-----------------|
| Dataset 1 | 4.5            | 4   | 3.75 | 4.25 | 4.75            |
| Dataset 2 | 4.5            | 3.5 | 4.25 | 4    | 4.75            |

current position ( $l_{next}$ ), as shown in the Eq.(4.17), the gravitational force constant was set to 0.2, which was smaller than the other coefficients. In our experiment, 8-bit grayscale images were used, and, therefore, the maximum position allowed for each parcel( $l_{max}$ ) was set to be 255. The Bland-Altman plot is useful for highlighting the possible bias in the IMT measurement. As shown in Figure 4.11, the data points (IMT values) of the proposed method lie within the  $\pm 2$  SD of the mean difference compared to those of the existing approaches. The implemented techniques showed a negative IMT measurement bias, which means that the computer-based methods underestimated the IMT. The box plot shown in Figure 4.12 is useful for illustrating the data distribution and for identifying outliers. The spacing between the points in the box shows the degree of dispersion and skewness of the data. Figure 4.13 presents the regression analysis of the ground truth IMT mean values versus the measured IMT values. Most of the points in the proposed method fit into the linear line as compared to the those of the existing methods. It shows that the measurements of the automatically segmented data were highly correlated to the ground truth data. A radiology expert (with experience of 5 years) evaluated the segmented IMT as shown in Figure 4.9 and Figure 4.10 by giving a score out of 5, and the scores are shown in Table.4.6 (0-worst,5-best). These results further confirmed the better performance of the proposed method over the existing methods. The existing segmentation algorithms have some limitations. In the SS algorithm, the existence of acoustic shadowing with strong speckle noise impeded the visual and automatic analysis of the ultrasound images. Dynamic programming includes boundary features such as intensity gradient, echo intensity, and boundary continuity that are dependent on the ultrasound scanner used and on its settings. Therefore, training is needed when the scanner is changed. The MB technique does not allow the improvement of robust mechanism that implements a reliable measurement of the LI and MA boundaries. The key contribution of this work is a novel approach for a fully automatic ROI extraction in carotid ultrasound images. In previous works (Yang (2014)), edge-based segmentation was commonly used for evaluating the IMT; in this study, however, we used a threshold-based segmentation method

for a robust measurement of the IMT using the WDO algorithm.

## 4.3 Proposed method based on Structured Random Forest

Edge detection is a primary image processing technique used for object detection, data extraction, and image segmentation. Recently, edge-based segmentation using structured classifiers is receiving increasing attention. The speckle present in the ultrasound images is reduced using a Weiner filter in the wavelet domain; followed by an enhancement technique based on adaptive gamma correction (AGC), which is applied to improve the robustness before segmentation. Section 4.3.1 briefly discuss about the related work on edge based segmentation based on structured random forest (SRF). In section 4.3.2, we present a novel ROI extraction for segmentation IMT of the CCA and applied pre-trained SRF classifier to the extracted ROI for quantifying the IMT. Finally, section 4.3.3 explains the comprehensive results of the proposed method with respect to the state-of-the-art methods and discussion with an experimental analysis is presented in section 4.3.4.

### 4.3.1 Related Work on Structured Random Forest

Edge detection is the primary component of several types of tasks such as object detection, image segmentation, and active contouring (Malik *et al.* (2001)). Traditional approaches for edge detection make use of a variety of features such as brightness, contrast, texture gradient, and color (Xiaofeng and Bo (2012)). In the past decades, edge-detection methods have made use of several learning techniques for image segmentation (Zheng *et al.* (2010)). The learning approaches involve the consideration of an image patch and estimation of the likelihood that the center pixel will contain an edge (Arbelaez *et al.* (2011)). The edges in the image patch are more interdependent and are designed in the form of straight and parallel lines. Recently, the structured learning approach has been applied to the problem existing similar characteristics (Nowozin *et al.* (2011)). The fast edge detection using a learning-based classifier has been receiving increasing attention. In the past few years, several methods have been implemented using a learning-based technique for the detection of edges (Mairal *et al.* (2008)). The boosted classifier is used to label each pixel independently based on its neighborhood image patch as an input (Dollar *et al.* (2006a)). Ren et al. in Arbelaez *et al.* (2011) improved this result by computing the gradient across the learned sparse codes of the patch gradients (Xiaofeng and Bo (2012)). Zheng *et al.* (2010) proposed the use



of a learning-based approach for the detection of object boundaries and demonstrated results of specific object detection. Lim et al. proposed the use of sketch tokens using supervised mid-level information for edge detection in the form of hand-labeled images (Lim *et al.* (2013)). Among all, structured learning prediction deal with the problem of mapping learning approach to input or output spaces randomly representing bounding boxes, sequences, and object pose (Taskar *et al.* (2005), Blaschko and Lampert (2008)). Kotschieder et al. in (Kotschieder *et al.* (2011)) introduced structured class labels for learning random forest and semantic labels for an image patch referred to as the output label. The structure information evaluates the split function in each branch of the tree using decision tree class labels. The information gain measures are evaluated by mapping structured labels to a discrete space. The classification problem is addressed by using a supervised SRF.

### 4.3.2 Proposed Methodology

#### (a) Dataset description

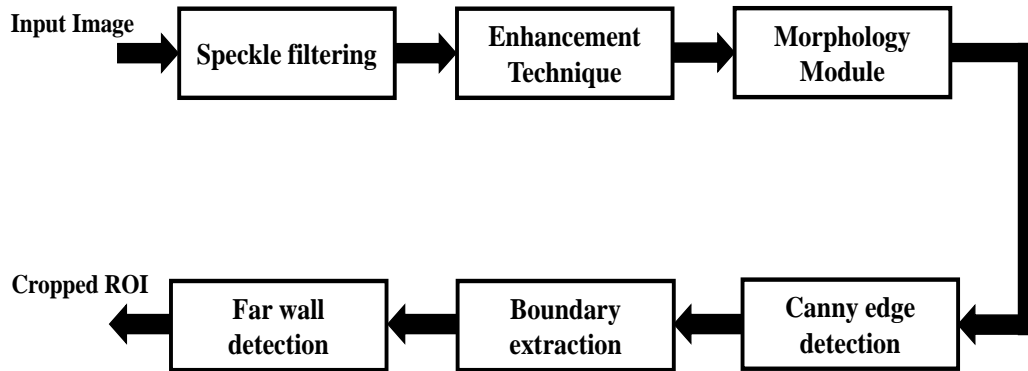
The images were acquired using the ATL HDI 3000 ultrasound machine, which has a frequency range of 4–7 MHz. The frames were captured at a resolution of 564 x 800 pixels and resampled at a standard density of 16.66 pixels/mm. Textual marks were eliminated, and the images were cropped to a size of 395 × 295 pixels. For our experiment, we used a dataset from the Cyprus Institute of Neurology of Nicosia (CyprusUniversity (2007)). The dataset consists of 100 images, of which 70 images are used to evaluate the performance of the proposed and existing methods. The remaining 30 images were ignored because of their poor visual quality.

#### (b) Automatic Extraction of the ROI

The block diagram of the automatic ROI extraction is shown in Figure 4.14, and each block is explained below.

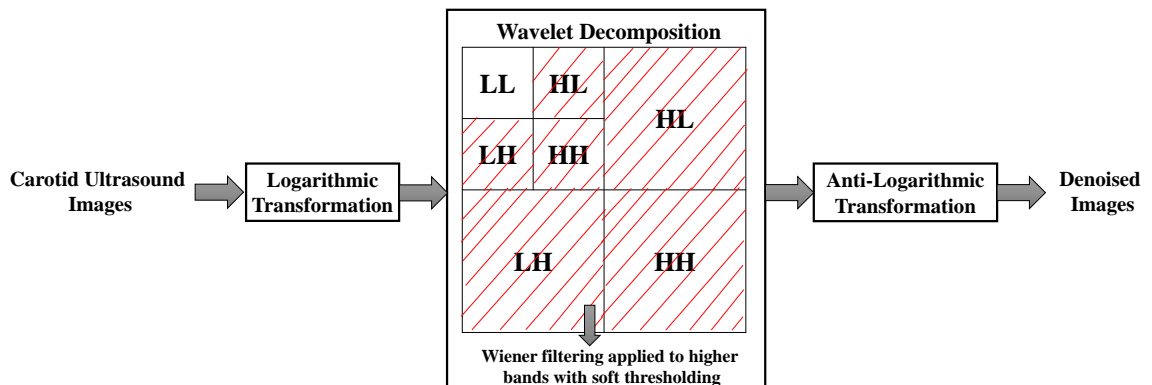
- **Speckle Filtering**

In carotid ultrasound images, speckle noise and artefacts cause image degradation in several medical image modalities. The degradation of the image has a significant impact on human interpretation and the accuracy of the computer-assisted methods. In literature, several methods have been developed for reducing the speckle noise in the ultrasound image. In a carotid ultrasound image, speckle noise is a multiplicative noise that degrades the image quality by concealing the fine structures. In our experiments, the multiplicative noise is converted into additive noise by using a logarithmic



**Figure 4.14:** Outline of ROI extraction.

transformation. It is assumed that the distribution of additive noise is very close to Gaussian noise distribution. Usually, the Gaussian noise is preferred because it corresponds to quadratic data term, which is linear and easy to solve. The quadratic data terms are convex and lead to the global minima. The traditional denoising techniques require a significant amount of execution time because of the iterative processes involved. To solve this problem, we propose the use of Wiener filtering in the wavelet domain (Zong *et al.* (1998)). The Wiener filter smoothens the image while retaining the edges, and performs ROI extraction significantly faster than other similar techniques. A detailed explanation is provided in Algorithm 1. A block diagram of the despeckling filter is illustrated in Figure 4.15, and an example of a despeckling image are shown in Figure 4.16(b).



**Figure 4.15:** Block diagram of denoising method.

- **Image Enhancement:**

---

**Algorithm 1 The steps for despeckling.**

---

**Input:** Carotid noisy image.

**Output:** Denoised image.

*Initialization:*

- 1: The ultrasound carotid image has a multiplicative speckle noise that is converted into an additive noise by using a logarithmic transformation.
- 2: Orthogonal two-level wavelet decomposition is performed on the Gaussian noise distribution.
- 3: The Wiener filter is applied to each high sub-band as shown in the highlighted red line in Figure 4.15, and it is defined as (Zong *et al.* (1998));

$$I_s(u, v) = m + \frac{\sigma^2 - n^2}{\sigma^2}(I(u, v) - m)$$

where  $m$  and  $\sigma^2$  are the local mean and variance of each pixel of the image  $I(u, v)$ , and  $n^2$  is the noise variance.  $I_s(u, v)$  represents the high sub-bands LH, HL, and HH.

- 4: For each of the sub-bands, the soft thresholding is calculated based on the following formula (Zong *et al.* (1998));

$$I_o(u, v) = \begin{cases} I_s(u, v) - t, & \text{if } I_s(u, v) \geq t \\ I_s(u, v) + t, & \text{if } I_s(u, v) \leq -t \\ 0, & \text{if } |I_s(u, v)| < t \end{cases}$$

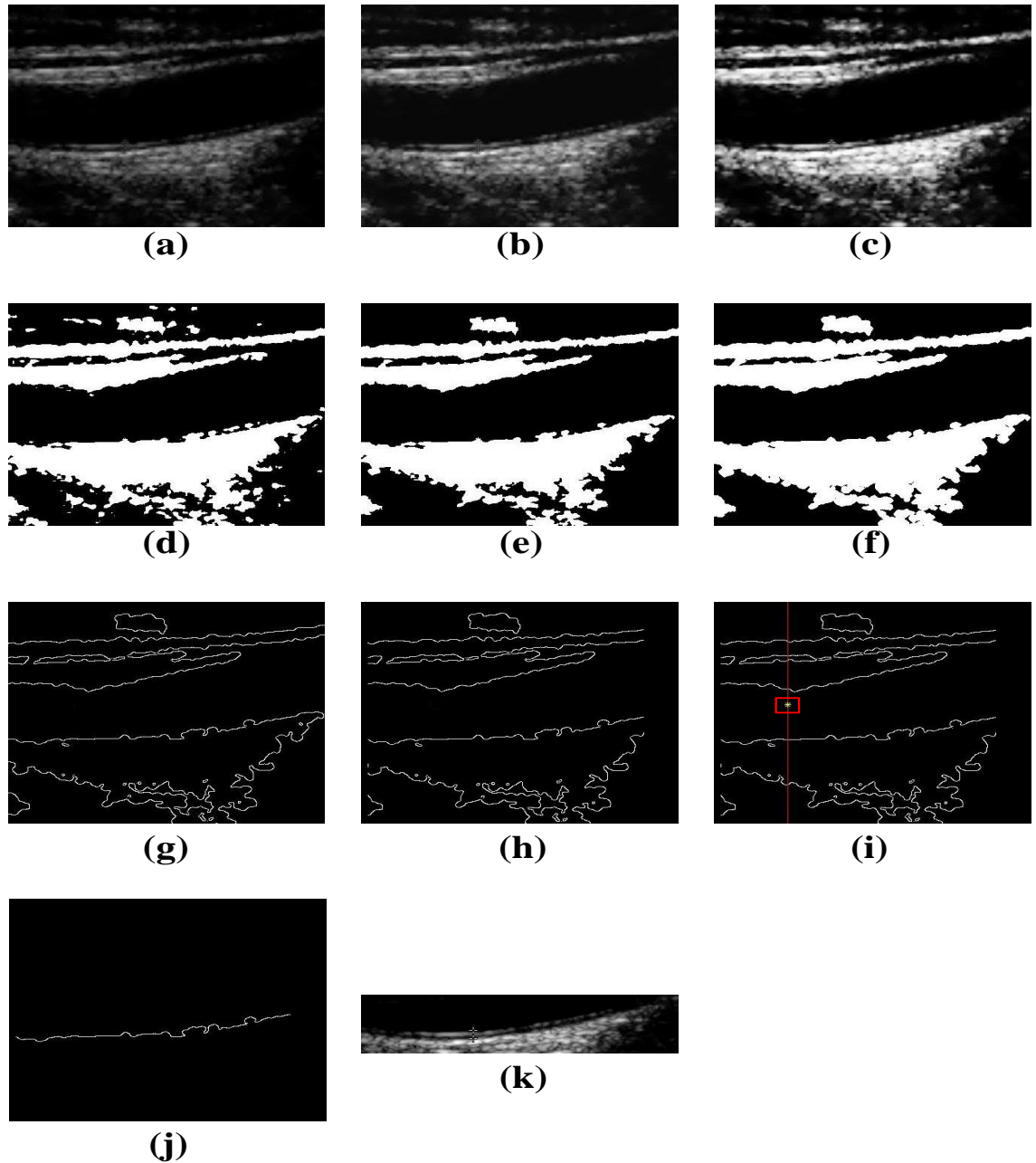
where  $t$  is the threshold.

- 5: The LL sub-band remains unchanged in the wavelet decomposition.
  - 6: Finally, the image is reconstructed from the denoised wavelet coefficient by performing an inverse discrete wavelet transform, which is followed by an anti-log transformation.
- 

The main purpose of the enhancement is to process an image such that the resultant image contains more relevant information than the original image. This work proposes the use of AGC (Huang *et al.* (2013)) for image enhancement. AGC makes use of the cumulative density function (*cdf*), and the normalized gamma function is applied to modify the transformation curve without losing any statistical information. The point transformation on pixel value  $i$  is expressed as (Huang *et al.* (2013)):

$$T(i) = i_{max}(i/i_{max})^y \quad (4.19)$$

where  $i$  denotes the intensity of each pixel in the input image and is transformed as  $T(i)$ , and  $i_{max}$  is the maximum intensity of the input. The weighting distribution function is calculated in order to modify the histogram of the image as follows (Huang



**Figure 4.16:** Automatic extraction of ROI. (a) Original carotid longitudinal ultrasound image. (b) De-speckled image using Wiener filter in the wavelet domain. (c) Enhancement using adaptive gamma correction. (d) Conversion of the binary image with automatic thresholding procedure. (e) Area opening for remove smaller objects. (f) dilation is for filling gaps and holes in the plaque contour. (g) Edge detection using canny operator. (h) The cropped canny edge detected an image. (i) Center point is detected based on maximum zeros lies on the vertical line. (j) Near-wall extraction. (k) ROI extraction.

*et al.* (2013)):

$$P_w(i) = P_{max} \left( \frac{P(i) - P_{min}}{P_{max} - P_{min}} \right)^\alpha \quad (4.20)$$

where  $\alpha$  represents the adjusted parameter, which is set to 0.6.  $P(i)$  represents the probability density function of the histogram of an image, where  $P_{max}$  and  $P_{min}$  respectively represent the maximum and minimum values.  $cdf$  is obtained as follows (Huang *et al.* (2013)):

$$cdf(i) = \frac{\sum_{i=0}^{255} P_w(i)}{\sum P_w} \quad (4.21)$$

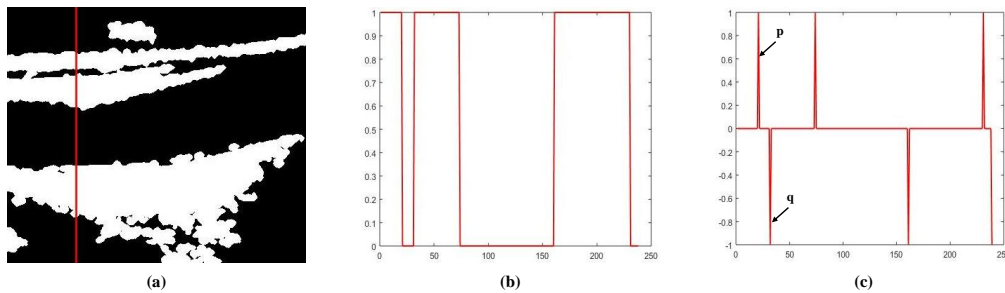
where the sum of  $P_w$  is calculated as  $\sum P_w = \sum_{i=0}^{255} P_w(i)$ , and the adaptive parameter  $\gamma$  is estimated based on  $cdf$ . In order to enhance the carotid ultrasound image using Eq.4.19,  $\gamma$  is modified as follows (Huang *et al.* (2013)):

$$\gamma = 1 - cdf(i) \quad (4.22)$$

The enhanced denoised image thus obtained is shown in Figure 4.16(c). After enhancing the image, the resultant image is converted into a binary image based on the thresholding process (Nagaraj *et al.* (2018)).

- **Morphological Module and Center Point Detection:**

The morphological operation is applied to the binary image and a detailed explanation of the morphological module and center point detection is described in Algorithm 2.



**Figure 4.17:** (a) Selection of line in the binary image for detection of a center point. (b) The intensity profile of the column denoted by a vertical line in the binary image. (c) The vertical line is differentiated based on positive peak  $p$  and negative peak  $q$ .

---

**Algorithm 2 The steps for center point detection.**

---

**Input:** Enhanced image.

**Output:** Center point detection.

*Initialization:*

- 1: The enhanced image is converted into a binary image using the adaptive thresholding technique, as shown in Figure 4.16(d).
  - 2: The large morphological area opening is applied to the binary image in order to remove the small objects, as illustrated in Figure 4.16(e).
  - 3: The structuring element of disk size 2 is applied in order to eliminate the gaps and seal the plaque contour using a dilation operation, as depicted in Figure 4.16(f).
  - 4: The edges are extracted using the Canny edge-detection technique, as shown in Figure 4.16(g).
  - 5: In order to detect the center point, the vertical profile line in the binary image is analyzed to find the maximum number of continuous zeros, as shown in Figure 4.17(a).
  - 6: The intensity on line "t" is then differentiated, as shown in Figure 4.17(b), and the general expression of differentiation is thus obtained as  $d = t - (t - 1)$ .
  - 7: After the differentiation, the locations of the positive and negative peaks are determined and respectively denoted as  $p$  and  $q$ , as shown in Figure 4.17(c).
  - 8: The starting location of the long-spanning zeros is found by using  $L = \max(q - p)$ , and the center location is chosen to be 10 pixels away from the starting location.
  - 9: Finally, the borders of some pixels are eliminated to separate the connected edges, as shown in Figure 4.16(h) and the center point is detected from the vertical profile line, as shown in the Figure 4.16(i).
- 

• **ROI extraction:**

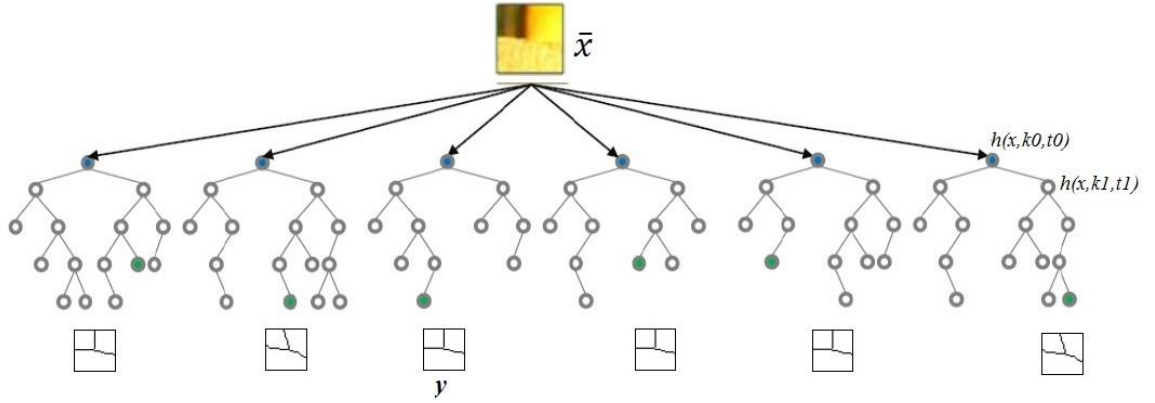
Typically, IMT thickness is estimated in the far wall region, because IMT measurements from the far wall are more reliable than those obtained from the near wall (Molinari *et al.* (2010b)). Hence, the random point is moved downward from the center point until the high-intensity grayscale value (255) is detected, as depicted in Figure 4.16(i). Using the high-intensity grayscale value, the far wall is extracted based on the connected line from the detected pixel. The extracted far wall is shown in Figure 4.16(j). Thereafter, the image region contained within 30 pixels above the line and 30 pixels below the line is extracted. Finally, the ROI is cropped for further segmentation, as shown in Figure 4.16(k).

**(c) Structured Random Forests for IMT segmentation**

The SRF represents an image patch  $x$  from a feature space  $X$ , which is given by  $x \in X$ , and encodes the corresponding local image patch  $y$  in the feature space  $Y$ , which is given

by  $y \in Y$  (Dollár *et al.* (2006b)). The training of structured labels using the random forest poses two main challenges. First, the dimension of the structured output spaces is complex in nature. Thus, scoring several candidates splits over the structured labels is prohibitively expensive. Second, the information gain over the structured labels is not well defined. In a structured forest, the structured labels  $y \in Y$  are mapped to the discrete set of labels  $c \in C$  for a given node. For the given set of labels  $C$ , the information gain is estimated directly and efficiently over  $C$ , which can serve as a proxy for the information gain over the structured labels  $Y$ . Furthermore, the resultant of each node effectively influences the training procedure of the existing random forest in the learning of the structured forest. The structure output spaces used for edge detection and estimating the similarity over  $Y$  are not well defined. Alternatively, the feature space  $Y$  is mapped to an intermediate space  $Z$  such that the Euclidean distance can be easily measured. The SRF method uses mapping from  $Y \rightarrow Z$  followed by the mapping of  $Z \rightarrow C$ .  $Z$  is a high-dimensional domain and thus presents a computational challenge. In order to reduce the dimensionality of the  $Z$  domain, principal component analysis (PCA) is used. The PCA is used for denoising  $Z$  such that it approximately preserves the Euclidean distance. Subsequently, the information gain is defined by the entropy (Criminisi *et al.* (2012)) for the continuous formulation of the  $Z$  domain. The drawback is that the ensemble model is unable to incorporate the novel labels such that any prediction  $y \in Y$  will be observed during the training. Indeed, it is not possible without information regarding  $Y$ , and the use of a specific ensemble model is preferable. The detailed explanation of the edge detection using SRF is given in Algorithm 3 and pictorial representation of ensemble training model is shown in Figure 4.18. Further, details of the SRF are available in (Dollár and Zitnick (2013)).

In this work, the problem of predicting local edge masks in a structured learning framework that is applied to random decision forests has been formulated. The standard information gain is then estimated in learning decision trees by mapping structured labels to a discrete space. In our experiment, all data must be divided into training and testing; however, owing to the lack of a dataset, the experimental results reflect poor performance. Hence, the pre-trained edge model of the BSDS500 segmentation dataset is used (Dollár and Zitnick (2013)). The dataset comprises 300 images, which include color and grayscale images. Two hundred images are used for training and each image has hand-labeled ground truth contours. The learning approach anticipates a  $16 \times 16$  structured segmentation mask from a larger image patch of  $32 \times 32$ . The training dataset begins with the augmentation of each image patch with multiple additional channels of information, thus resulting in a



**Figure 4.18:** Pictorial representation of an ensemble of independent trees in the training process.

feature vector  $x \in \mathbb{R}^{32 \times 32 \times C}$ , where  $C$  is the number of channels. From the dataset BSDS500, a total of 3328 candidate features of  $x$ , and a set of gradient channels for computing three color channels in the CIE-LUV color space along with a normalized gradient magnitude are used at two scales. In addition, each gradient magnitude channel split into 4 channels based on orientation. As a result of total 13 channels are used, among all 3 for color, 2 for magnitude and 8 for orientation channels. The pairwise difference features also computed by applying large triangle to blur each channel and downsample at a resolution of  $5 \times 5$ . Sampling all candidate pairs and computing their differences yields an addition of 300 candidate features per channel and it results in a total of 7228 candidate features. Using the pre-trained model, the mean IMT value is estimated to be 0.66 for 70 test images. Furthermore, the average processing time for the automatic segmentation of the IMC was obtained 0.47s. The test samples are used in order to derive the model behavior for unseen samples. During the testing, the number of trees in the forest to be trained is eight, the maximum tree depth is 64, and the number of trees to be evaluated per location and computation thread is four. The obtained IMT boundary pixels that are classified using the structured forest model are overlapped over the ROI image, and the boundary pixels are joined together to obtain meaningful boundaries. The mean of the IMT ( $IMT_{mean}$ ) is estimated by measuring the mean absolute distance (MAD), which is defined as follows (Molinari *et al.* (2010b)):

$$IMT_{calpixels} = \frac{1}{N} \left( \sum_{i=1}^N (x_{i1} - x_{i2}) \right) \quad (4.23)$$

where  $IMT_{calpixels}$  is the mean of a number of pixels between the two boundaries,  $N$  is



---

**Algorithm 3 Edge detection using structured random forest**

---

**Input:** Input image is any kind of objects.

**Output:** Outputs are structured objects.

*Initialisation :*

- $\widehat{x}$ : Feature vector of input image patch.
- $y$ : Structured label space.
- $x_k$ : The  $k^{th}$  feature in  $x$ .
- $t$ : Threshold
- $h(x, k, t)$ : Split function.
- $Y$ : Structured space where information gain not well defined.
- $C$ : Discrete space where information space is good defined.
- $Z$ : Intermediate space where similarity measurement is easy to compute.

1: Compute for each node based on mapping form which is defined as:

$$\pi : Y \rightarrow Z, Z \rightarrow C.$$

2: After the mapping, we have a training set of feature vector  $C$ .

3: Pick a feature  $x_j$  and a threshold  $t$  which maximize the information gain.

4: Combining predictions:

-To compute  $y_1, y_2, \dots, y_n \in Y$  into a prediction:

- Compute  $z_i = \pi \psi(y_i)$  of dimension  $m$ .  
where  $m$  is the medoid, which minimize the sum of distances to all  $z_i$ .
- Select  $y_k$ , whose  $z_k = \operatorname{argmin}_{z_k} \sum_{i,j} (z_{kj} - z_{ij})^2$  is the medoid.

5: Finally, Compute the edge map from the segmentaion masks.

---

the number of columns in the image, and  $x_{i1}$  and  $x_{i2}$  are the two IMT boundary pixels in the columns, between which the number of pixels is calculated as follows :

$$IMT_{cal} = IMT_{calpixels} * \frac{1}{SR}$$

The calculated value of  $IMT_{calpixels}$  must be multiplied by the inverse of the spatial resolution (SR) of the images, which is equal to 16.66 pixels/mm, in order to obtain the IMT in mm.

### 4.3.3 Results

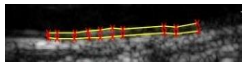
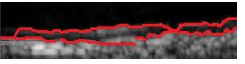
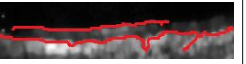
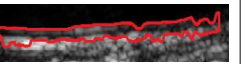
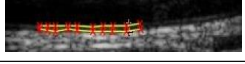
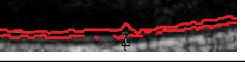
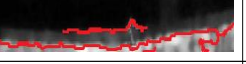
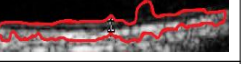
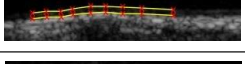



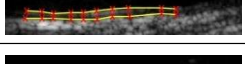
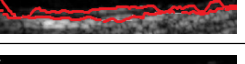
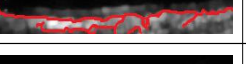
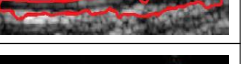

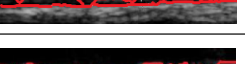


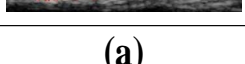
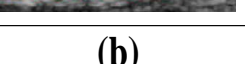
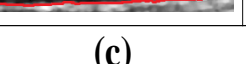
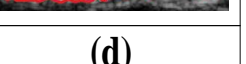
The experiment is conducted using 70 carotid ultrasound images to estimate the performance of the proposed segmentation algorithm. The results were compared with the state-of-the-art methods such as the MB (Ilea *et al.* (2013b)), DP( Li *et al.* (2014)), SS (Loizou *et al.* (2014)), threshold-based WDO (Nagaraj *et al.* (2018)), and (NN) (Menchón-Lara *et al.* (2014)) based algorithms.

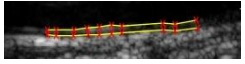


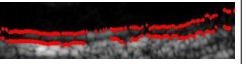
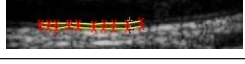
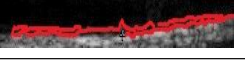

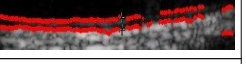
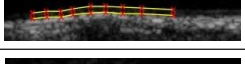
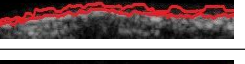

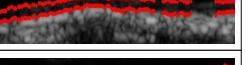
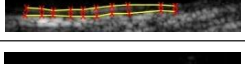



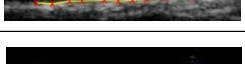


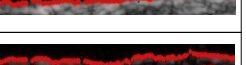

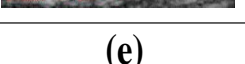


#### (a) Example on Sample Images

In order to ensure good generalization capability in existing algorithms such as the DP, MB, SS, WDO, and NN algorithms, six heterogeneous sample images from various CCA orientations were chosen for the purpose of comparison. Figure 4.19 shows the manual delineation performed by the expert and the automated segmentation of the IMT on six sample longitudinal carotid ultrasound images. Figure 4.19(a) depicts the ground truth sample images with manual delineation performed by an expert clinician. The automated segmentation of the LI and MA boundaries obtained using the DP, MB, SS, WDO, NN algorithms, and the proposed method are illustrated in Figure 4.19(b), (c), (d), (e), (f), and (g), respectively. The LI and MA boundary representations obtained by the DP algorithm are comparatively less accurate (see Figure 4.19(b)), owing to the pixel intensity variation in the image. The MB algorithm could not properly detect the edges of the IMT, as shown in Figure 4.19(c), owing to the irregularities in the IMC. Figure 4.19(d) shows the segmentation obtained using the snake contour; it is observed that the parametric curve evolution results in the self-interaction of the LI and MA boundaries. The boundary edges obtained by the WDO algorithm are not properly connected because of the lack of fine-tuning of the update equation coefficient, as shown in Figure 4.19(e). The NN algorithm fails in slating IMCs with weak boundaries, as depicted in Figure 4.19(f). Overall, the proposed method retains the details of the image and exhibits robustness in the estimation of the IMT in the LI and MA boundaries, as shown in Figure 4.19(g).

#### (b) Accuracy Performance

The average IMT value ( $IMT_{mean}$ ) is estimated using Eq.(4.23) by measuring the mean absolute distance between the LI and MA boundaries. Table 4.7 shows that the  $IMT_{mean} \pm$  std of the proposed method (  $0.66 \pm 0.14$  mm) was closer to the ground truth value ( $0.67 \pm 0.15$  mm) as compared with those of the state-of-the-art techniques. The PD metric (from Eq.2.8) also used for measuring the distance between LI and MA boundaries. The result of PD metric is tabulated in the Table 4.7 and it can be observed that  $IMT_{mean}$  value of PD metric gives a poor performance as compared to the  $IMT_{mean}$  value of MAD metric because most of the

|          | Ground Truth  | DP  | MB   | SS  |
|----------|---|---|--|---|
| Sample 1 |  |  |  |  |
| Sample 2 |  |  |  |  |
| Sample 3 |  |  |  |  |
| Sample 4 |  |  |  |  |
| Sample 5 |  |  |  |  |
| Sample 6 |  |  |  |  |
|          | (a)   | (b)   | (c)  | (d)   |

|          | Ground Truth  | WDO   | NN   | Proposed Method   |
|----------|---|---|--|---|
| Sample 1 |  |  |  |  |
| Sample 2 |  |  |  |  |
| Sample 3 |  |  |  |  |
| Sample 4 |  |  |  |  |
| Sample 5 |  |  |  |  |
| Sample 6 |  |  |  |  |
|          |   | (e)   | (f)  | (g)   |

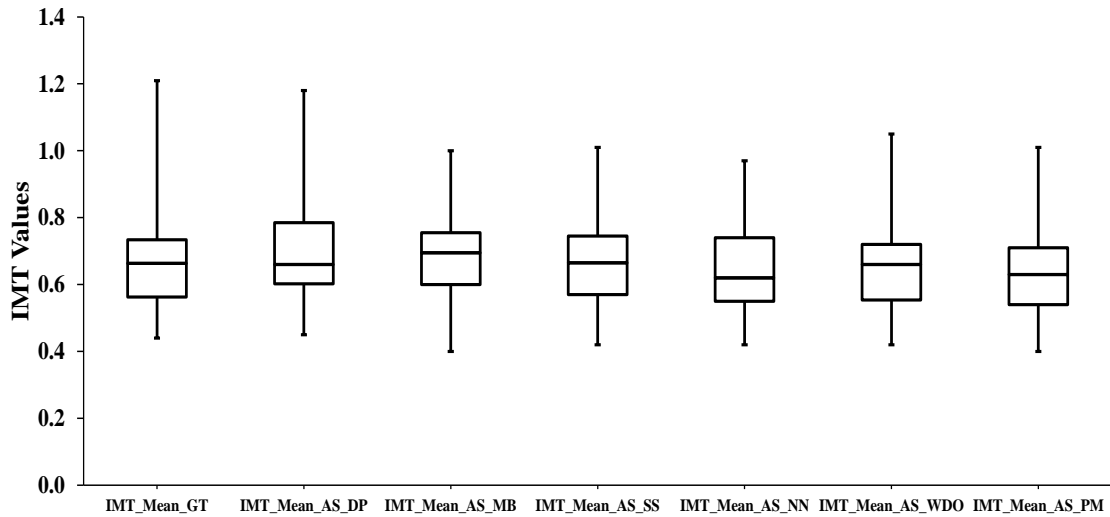
**Figure 4.19:** Manual delineation from an expert and Automated segmentation IMT using DP, MB, SS, WDO, NN and Proposed method of longitudinal carotid ultrasound six sample images.

images in our dataset have straight and horizontal lines. The PD metric gives better results for curved or inclined nature of images Molinari *et al.* (2010b). The CV of the proposed

**Table 4.7:** Mean IMT values, CV-coefficient variation, R-correlation co-efficient, mean bias and execution time of automated method and the ground truth for 70 carotid ultrasound images.

| Metrics                            | GT                | DP                | MB                | SS                | NN                | WDO               | Proposed Method   |
|------------------------------------|-------------------|-------------------|-------------------|-------------------|-------------------|-------------------|-------------------|
| $IMT_{mean} \pm std$<br>(mm) (MAD) | 0.67±0.15<br>(mm) | 0.70±0.14<br>(mm) | 0.69±0.12<br>(mm) | 0.68±0.13<br>(mm) | 0.64±0.13<br>(mm) | 0.65±0.13<br>(mm) | 0.66±0.14<br>(mm) |
| $IMT_{mean} \pm std$<br>(mm) (PD)  | 0.67±0.15<br>(mm) | 0.71±0.12<br>(mm) | 0.70±0.14<br>(mm) | 0.69±0.13<br>(mm) | 0.62±0.17<br>(mm) | 0.63±0.13<br>(mm) | 0.65±0.11<br>(mm) |
| CV%                                | 15.83             | 14.14             | 12.29             | 13.51             | 14.36             | 14.13             | 14.99             |
| R (refer Fig 4.22)                 | -                 | 0.78              | 0.88              | 0.85              | 0.77              | 0.91              | 0.92              |
| Bias (refer Fig 4.21)              | -                 | -0.02             | -0.02             | 0.004             | 0.03              | 0.02              | 0.01              |
| Execution time(Sec)                | -                 | 2.98              | 3.196             | 2.45              | 5.69              | 1.95              | 0.47              |

method (14.99%) was calculated using Eq.(2.10) and was found to be closer to the ground truth (15.83%) as compared with those of other methods. This shows that the amount of variability relative to the mean is almost the same for the proposed method and ground truth values. The Pearson correlation coefficient R (as shown in Figure 4.22) was estimated using Eq.(2.9); the R-value of the proposed method was 0.92, which was higher than the R values of the state-of-the-art techniques. The mean biases of the proposed method (0.01 mm; Figure 4.21) and SS (0.004 mm) were the lowest as compared to the other methods, which shows that the estimated IMTs obtained using the other methods were thicker than the ground truth. Figure 4.20 illustrates the box plot of automatically segmented and ground truth data for all 70 carotid ultrasound images. The interquartile range (IQR) is calculated for the box plot in order to quantify the statistical dispersion based on the division of the dataset into upper and lower quartiles. The IQRs of the DP algorithm (0.18 mm), MB algorithm (0.16 mm), SS algorithm (0.18 mm), WDO algorithm (0.16 mm), NN algorithm (0.19 mm), and proposed method (0.17 mm) are estimated with respect to the ground truth data (0.17 mm), and it was found that the proposed method shows results that are comparable to those of the other techniques. Figure 4.21 shows the Bland–Altman plots of the mean IMT values versus the difference in the average IMT values between the ground truth and automatic measurements. In the Bland–Altman plot, the centerline illustrates the mean difference (0.01); the top and bottom lines depict the limits of the agreement lying between 0.12 mm and -0.10 mm; these are referred to as the mean  $\pm 2$  SD (standard deviation) of the difference. The plot in Figure 4.21(f) shows that 95% of the data points lie on the  $\pm 2$  SD of the mean difference as compared with other methods, and some data points lying outside the



**Figure 4.20:** The mean IMT (using MAD metric) calculated for the database of 70 carotid ultrasound images for ground truth data (IMT\_mean\_GT) and the automatic segmentation (IMT\_mean\_AS) of DP, MB, SS, NN, WDO, and proposed method(PM).

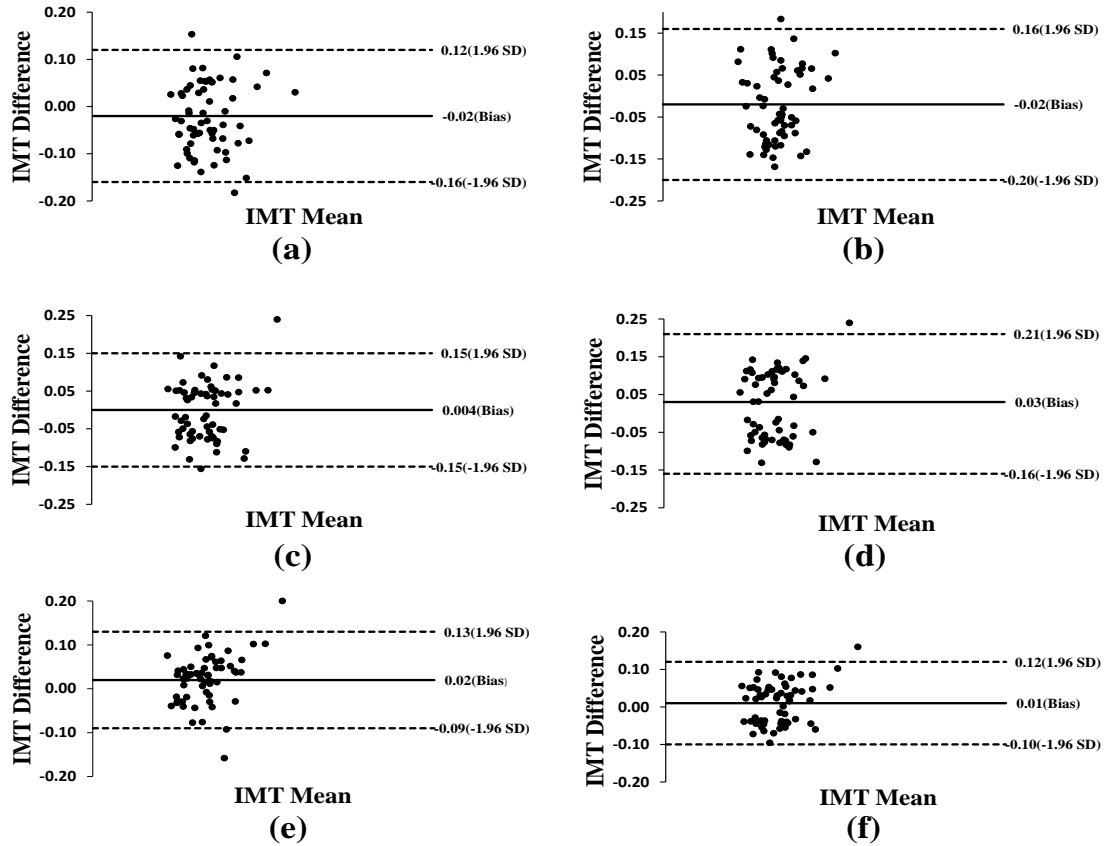
$\pm 2$  SD are considered as outliers. Figure 4.22 presents the regression plot of the automated segmentation IMT values versus the ground truth IMT values. As specified in Figure 4.22, the equation “y” anticipates the automated segmented value based on the ground truth value and correlation coefficient  $R$ , which provides the best fit between the automated value and the ground truth value. The majority of the points in the proposed method fit into the linear line, which was not the case in the existing methods.

### (c) Parameter Settings

Our approach has been compared with some existing techniques such as DP, MB, SS, WDO, and NN methods. The parameters used for the state-of-the-art algorithms are tabulated in the Table.4.8. In the NN algorithm, all the pixels are incompatible for training as the dataset would be highly imbalanced. To obtain a balanced dataset, we used 8000 patterns, among which 4000 were classified as the IMT boundary while the remaining samples were classified as the non-IMT boundary. Using the dataset, the NN was evaluated via two-fold cross-validation. It is observed that each of the 70 images was tested only once and that the mean IMT value across two-fold cross-validation was 0.64. The prior probabilities of the training and test data were the same as in each of the classes. The hidden layer in the network used for the training purpose comprised 20 neurons.

### (d) Execution time

In medical image processing, execution time is an important metric for measuring the

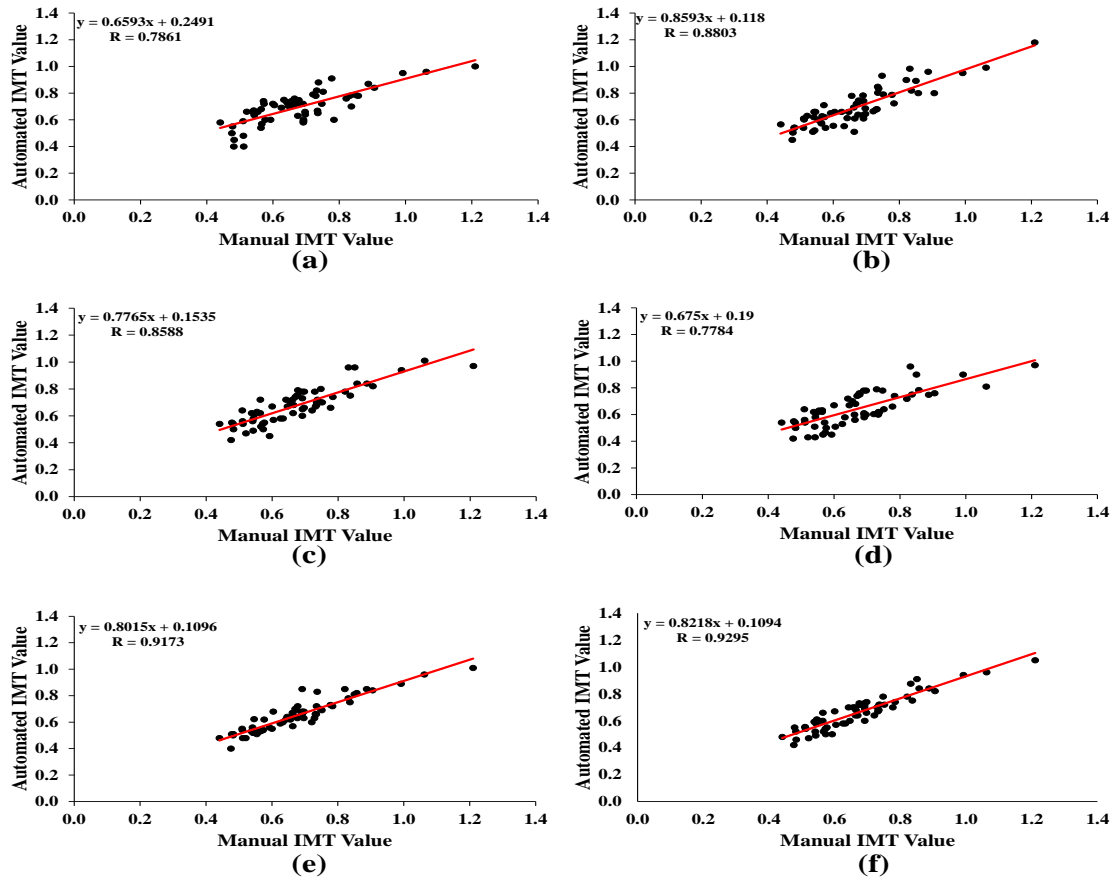


**Figure 4.21:** Bland Altman plots of the mean against the difference in the IMT mean values (automatic segmentation corresponding to the ground truth data) (using MAD metric). a) DP b) MB c) SS d) NN e) WDO f) Proposed Method.

running time of an algorithm. From Table.4.7, it can be observed that the average execution time of the proposed method (0.47 s) is less than that of the DP (2.98 s), MB (3.196 s), SS (2.45 s), WDO (1.95 s), and NN (5.69 s) algorithms. It must be noted that these average execution times are recorded during the testing of a single unknown image. The state-of-the-art algorithms were implemented in MATLAB R2015a and tested on a machine with an Intel(R) Core(TM)-i7 processor with 8 GB of RAM.

### 4.3.4 Discussion

The main objective of the work is to quantify the IMT automatically in carotid ultrasound images by effectively utilizing fast edge detection based on a structured prediction process. The experimental analysis described in the previous section show that the proposed au-



**Figure 4.22:** Regression analysis plots comparing automated segmentation measurements with manual measurement (using MAD metric). a) DP b) MB c) SS d) NN e) WDO f) Proposed Method.

Automatic IMT segmentation gives better result compared to state-of-the-art methods. Figure 4.21 Bland-Altman plot is useful for highlighting the possible bias in the IMT measurement. The negative bias of the DP and MB algorithms shows that computer methods underestimate IMT. Figure 4.22 presents that the measurements of the automatically segmented data were highly correlated to the ground truth data. We applied the Wilcoxon rank sum test to the 70 measured images in order to estimate the non-parametric significance between the automatic and ground truth IMT values. The calculated Wilcoxon rank sum test value for the proposed method is 0.21, which shows that there is no significant difference between the automated and ground truth data measurements (any Wilcoxon rank sum test value that is  $>0.05$  indicates that there is no significant deviation between the automated and ground truth data measurements). Radiology experts (with five years of experience) evaluated the

**Table 4.8:** Parameter setting used for Dynamic programming, Model based, Snake segmentation and WDO algorithms.

| <b>DP</b>                              |           |           |          |                |              |       |     |           |           |
|--|-----------|-----------|----------|----------------|--------------|-------|-----|-----------|-----------|
| Parameters                             | $r$       | $\lambda$ | $d$      | $k$            |              |       |     |           |           |
| Values used in (Li et al. (2014))      | 15        | -0.2      | 20       | $10 \times 10$ |              |       |     |           |           |
| Values used for our experiment         | 10        | -0.1      | 16       | $7 \times 7$   |              |       |     |           |           |
| <b>MB</b>                              |           |           |          |                |              |       |     |           |           |
| Parameters                             | $S_{max}$ |           |          | $\sigma$       |              |       |     |           |           |
| Values used in (Ilea et al. (2013b))   | 15        |           |          | 1.5            |              |       |     |           |           |
| Values used for our experiment         | 30        |           |          | 1.0            |              |       |     |           |           |
| <b>SS</b>                              |           |           |          |                |              |       |     |           |           |
| Parameters                             | $\alpha$  | $\beta$   | $\gamma$ | $stepsize$     | $iterations$ |       |     |           |           |
| Values used in (Loizou et al. (2015))  | 0.6       | 0.4       | 2        | -              | -            |       |     |           |           |
| Values used for our experiment         | 0.4       | 0.3       | 1.5      | 1              | 100          |       |     |           |           |
| <b>WDO</b>                             |           |           |          |                |              |       |     |           |           |
| Parameters                             | $P$       | $N$       | $i$      | $RT$           | $g$          | $\mu$ | $C$ | $u_{max}$ | $l_{max}$ |
| Values used in (Nagaraj et al. (2018)) | 20        | 3         | 200      | 3              | 0.2          | 0.4   | 0.4 | 70        | 255       |
| Values used for our experiment         | 20        | 3         | 200      | 3              | 0.2          | 0.4   | 0.4 | 70        | 255       |

**Table 4.9:** Validation(out of 5) of ultrasound carotid images from the radiology experts.

| Dataset  | Manual measure | DP   | MB   | SS   | WDO  | NN   | Proposed method |
|----------|----------------|------|------|------|------|------|-----------------|
| Expert 1 | 4.5            | 4.25 | 3.8  | 4.4  | 4.65 | 4.3  | 4.8             |
| Expert 2 | 4.5            | 3.9  | 3.55 | 4.25 | 4.4  | 4.25 | 4.75            |
| Expert 3 | 4.5            | 4.05 | 3.7  | 4.15 | 4.5  | 4.15 | 4.85            |

segmented IMT as shown in Figure 4.19 by providing a score out of 5, which is presented in Table.4.9 (0 = worst and 5 = best). Table.4.10 shows the results of other published techniques for measuring the IMTs of carotid ultrasound images. It is important to note that obtaining a direct comparison of various techniques is difficult owing to the dependence on image quality, number of images used for the experiment, measurement protocol, and characteristics of the results. In addition, most of the methods are not completely automatic, and the automated ones consider a fixed spatial resolution for the image. The major issue related to the segmentation is poor visibility of the carotid ultrasound image owing to the patient variation with respect to the structure and mechanical properties of the arterial wall, speckle noise and irregularity associated with the LI and MA boundaries caused by the non-



**Table 4.10:** Summary of IMC segmentation algorithm using other techniques

| Author                            | Images Used  | IMT(Manual/GT) (mm) | IMT (Method) (mm) | Automatic |
|-----------------------------------|--------------|---------------------|-------------------|-----------|
| Liang <i>et al.</i> (2000)        | 50           | 0.88± 0.25          | 0.93±0.25         | No        |
| Liguori <i>et al.</i> (2001)      | 20           | 0.92± 0.19          | 0.92±0.20         | No        |
| Gutierrez <i>et al.</i> (2002)    | 30           | 0.63 ± 0.12         | 0.72 ± 0.14       | No        |
| Loizou <i>et al.</i> (2007)       | 100          | 0.67± 0.16          | 0.68±0.12         | No        |
| Faita <i>et al.</i> (2008)        | 150          | 0.56± 0.14          | 0.57±0.14         | No        |
| Molinari <i>et al.</i> (2010a)    | 182          | 0.92± 0.30          | 0.75±0.39         | Yes       |
| Molinari <i>et al.</i> (2012)     | 365          | 0.95± 0.39          | 0.91±0.44         | Yes       |
| Xu <i>et al.</i> (2012)           | 50           | 0.63± 0.14          | 0.65±0.16         | No        |
| Ilea <i>et al.</i> (2013a)        | 772 (frames) | 0.60± 0.11          | 0.60±0.10         | Yes       |
| Menchón-Lara <i>et al.</i> (2014) | 60           | 0.64± 0.19          | 0.61±0.19         | Yes       |
| Li <i>et al.</i> (2014)           | 100          | 0.67± 0.12          | 0.69±0.12         | Yes       |
| Loizou <i>et al.</i> (2015)       | 976          | 0.74± 0.20          | 0.73±0.20         | No        |
| Li <i>et al.</i> (2016a)          | 224          | 0.75± 0.24          | 0.76±0.24         | No        |
| Proposed Method et.al             | 70           | 0.67± 0.15          | 0.66±0.14         | Yes       |

optical orientation of the ultrasound probe during the image acquisition. To address these problems, which are common in the analysis of CCA ultrasound data, we proposed to use SRF classifier algorithm. The state-of-the-art algorithms have some limitations. The SS includes acoustic shadowing with strong speckle noise that impedes the visual and automatic analysis of the ultrasound images. DP does not perform well in cases involving curved IMCs with weak boundaries. The MB technique does not allow the development of a robust mechanism that implements a reliable measurement of the LI and MA boundaries. The WDO algorithm outperforms other algorithms when its update equation coefficient receives fine-tuning. In NNs, the problem of overstraining always exists because minimizing the error measurement occasionally does not correspond to finding a well-generalized NN. Finally, our approach is well suited for IMC segmentation, and it facilitates a new application for high-quality edge detection.

## 4.4 Summary

In this chapter, we have presented different types of segmentation algorithms for measurement of IMT of the CCA. In the method based on SVM, the speckle noise has been reduced by using optimized BLSE filter and the enhancement based on  $TV - L_1$  norm has been applied to improve the robustness. Whereas in the method based on WDO algorithm, OBNLM filter is used to reduced the speckle noise and the enhancement based on  $TV - L_1$  norm has been applied to increase contrast of the image. These two proposed methods, takes a larger

amount of execution time for ROI extraction because of iterative processes involved. To overcome this problem, we used Weiner filtering in wavelet domain for speckle reduction and AGC has been used for the enhancement to improve the robustness. After speckle reduction and enhancement, ROI is extracted for segmentation of IMC of the CCA. In this work, totally three different types of ROI extraction is presented for detection of carotid wall. Among three types of ROI extraction, the one which is used for segmentation of IMC based on SRF gives faster and accurate results because of less iterative process involved. The proposed algorithms give better results in terms of performance metrics such as coefficient of variation, correlation coefficient, and  $IMT_{mean} \pm std$  as compared to the state-of-the-art techniques.



## Chapter 5

# CONCLUSIONS AND FUTURE WORK

### 5.1 Conclusions

Among the most common causes of death in majority of the countries, strokes rank third. About 80% of all stroke are ischaemic. The rupture of atherosclerotic plaques in the carotid artery is the major reason for ischemic strokes. Thus, there is an urgent need for better techniques for diagnosing patients at risk of stroke, and delivery of immediate treatment. The changes occurring in the carotid artery can safely be monitored via non-invasive imaging modality such as ultrasound imaging. However, since the manual measurement process is tedious and prone to error, automated software systems need to be developed which can measure the wall thickness and diameters of the carotid artery. The development of such automated systems was the primary objective of this research.

The main aim of this work was to carry out a comparative evaluation of despeckle filtering and compare them with several edge detection techniques with respect to the preservation of edges. As a pre-processing step, a robust denoising filter BLSE was proposed to reduce the speckle noise in ultrasound images by projecting it into the logarithmic space. Whereas, one of the widely accepted methods, OBFLM, was adopted in our work to reduce the speckle noise in ultrasound images. The speckle present in ultrasound image was reduced using different denoising filters and the results were compared with edge detection techniques in terms of edge preservation. In all images, the proposed BLSE algorithm achieved better results in terms of image resolution and edge delineation. The measured parameters PSNR, MSE, CoC and SSIM of BLSE denoising filter with canny edge detection

achieved better performance as compared to edge detection of other denoising methods. The visual information obtained from Figures (3.1,3.3,3.2,3.4) in chapter 3 indicate that the proposed denoising techniques yield better results as compared to existing methods. Contrast enhancement based on  $TV - L^1$  norm and AGC techniques are used for improving the robustness of the image. Further, we proposed three new approaches for fully automatic ROI extraction for detection of carotid wall. The ROI extraction based on BLSE and OBNLM denoising filter takes longer processing time because of the iterative process involved. To overcome this problem, we proposed Weiner filtering in wavelet domain for faster ROI extraction. The proposed segmentation techniques such as threshold-based WDO, SVM and SRF are robust for segmentation of IMC of the CCA. The measured parameters such as the coefficient of variation, correlation coefficient, and  $IMT_{mean} \pm std$  of the proposed methods showed better performance when compared to those of the existing methods. Based on the simulated data and visual inspection of the segmented outputs obtained from the Figures (4.3,4.9,4.10,4.19) in chapter 4 indicate that proposed segmentation approaches yield good results as compared to state-of-the-art methods. Further, among all the proposed methods, SRF exhibits superior result of  $IMT_{mean} \pm$  standard deviation of  $0.66\text{mm} \pm 0.14$ , which was closer to the ground truth value  $0.67\text{mm} \pm 0.15$  and takes an average of 0.47s processing time for the segmentation of IMC. Finally, experimental results demonstrated that the proposed segmentation techniques offer better quantitative and qualitative results as compared to other tested techniques reported in the literature. The segmentation results were also verified by different medical experts. Mean of ratings given by all three medical experts for segmentation results are above the average value. Hence, the proposed methods provide a very effective and robust fully automated technique for the measurement of IMT of the CCA.

## 5.2 Future Work

The proposed image based measurement system yields a significant tool for stroke and cardiovascular risk stratification. Significant technical and clinical progress can still be made in the field of carotid artery segmentation. The major challenge in the future will be the development of completely automated integrated systems. The future work is proposed in the following areas: 3D imaging, video segmentation and carotid artery segmentation in GPU framework.

**3D imaging:** The diagnostic performance may improve by applying the proposed tech-

niques used in this work to 3D ultrasound images (Zahalka and Fenster (2001)). Although 3D vascular imaging is very promising in revealing vascular structure and pathology, further work is needed in the directions of fast and accurate free hand scanning, semi automated and automated segmentation, user-friendly visualisation, and 3D texture analysis. Advances in these directions will enable wide spread use of 3D imaging in clinical diagnostics.

**Video segmentation:** The advent of powerful video systems nowadays allow medical video to supplement earlier imaging techniques, where medical video is used in various medical image analysis applications. Video imaging in medicine is important because it allows the expert to review the procedure and re-evaluate the initial diagnosis. The advantage of medical video imaging is the possibility of having multiple views and it allows a 3D reconstruction of the carotid artery (K. R. Subramanian (2000)). Generally, video segmentation of carotid artery is used to estimate the motion of boundaries of the plaque and classify the motion of the plaque in normal or abnormal cases.

**Carotid artery segmentation in GPU framework:** The important issue regarding modern segmentation algorithms is the computational cost. This results from different factors such as size of the image, number of sampling points and multi resolution algorithms. Further, some algorithms use complex iterative steps to achieve high accuracy for measurement. This in turn requires more processing power than conventional simple approaches which are straight forward. To avoid this limitation, a well known parallel computing architecture, GPU (graphical processing unit), can be utilized which provides excellent computing performance gain (up to 54 times faster than the parallel CPU implementation). Moreover, the technology used to develop these GPUs may vary based on the degree of versatility to be executed in different platforms. Finally, we hope that the performed research will contribute towards the advancement of medical imaging and processing technologies.

# Bibliography

- Abolmaesumi, P., M. R. Sirouspour, and S. Salcudean**, Real-time extraction of carotid artery contours from ultrasound images. *In Computer-Based Medical Systems, 2000. CBMS 2000. Proceedings. 13th IEEE Symposium on.* IEEE, 2000.
- Ahrens, C. D.**, *Meteorology today: an introduction to weather, climate, and the environment.* Cengage Learning, 2012.
- Akay, B.** (2013). A study on particle swarm optimization and artificial bee colony algorithms for multilevel thresholding. *Applied Soft Computing*, **13**(6), 3066–3091.
- Araki, T., P. K. Jain, H. S. Suri, N. D. Londhe, N. Ikeda, A. El-Baz, V. K. Shrivastava, L. Saba, A. Nicolaides, S. Shafique, et al.** (2017). Stroke risk stratification and its validation using ultrasonic echolucent carotid wall plaque morphology: a machine learning paradigm. *Computers in biology and medicine*, **80**, 77–96.
- Arbelaez, P., M. Maire, C. Fowlkes, and J. Malik** (2011). Contour detection and hierarchical image segmentation. *IEEE transactions on pattern analysis and machine intelligence*, **33**(5), 898–916.
- Association, A. H. et al.**, *Heart Disease and Stroke Statistics:... Update.* American Heart Association, 2002.
- Baldassarre, D., M. Amato, A. Bondioli, C. R. Sirtori, and E. Tremoli** (2000). Carotid artery intima-media thickness measured by ultrasonography in normal clinical practice correlates well with atherosclerosis risk factors. *Stroke*, **31**(10), 2426–2430.
- Bao, P., L. Zhang, and X. Wu** (2005). Canny edge detection enhancement by scale multiplication. *IEEE transactions on pattern analysis and machine intelligence*, **27**(9), 1485–1490.

- Bastida-Jumilla, M. C., R.-M. Menchón-Lara, J. Morales-Sánchez, R. Verdú-Monedero, J. Larrey-Ruiz, and J.-L. Sancho-Gómez** (2015). Frequency-domain active contours solution to evaluate intima-media thickness of the common carotid artery. *Biomedical Signal Processing and Control*, **16**, 68–79.
- Bayraktar, Z., M. Komurcu, J. A. Bossard, and D. H. Werner** (2013). The wind driven optimization technique and its application in electromagnetics. *IEEE transactions on antennas and propagation*, **61**(5), 2745–2757.
- Blaschko, M. and C. Lampert** (2008). Learning to localize objects with structured output regression. *Computer Vision—ECCV 2008*, 2–15.
- Bots, M. L., A. W. Hoes, P. J. Koudstaal, A. Hofman, and D. E. Grobbee** (1997). Common carotid intima-media thickness and risk of stroke and myocardial infarction the rotterdam study. *Circulation*, **96**(5), 1432–1437.
- Brosnan, T. and D.-W. Sun** (2004). Improving quality inspection of food products by computer vision—a review. *Journal of food engineering*, **61**(1), 3–16.
- Buades, A., B. Coll, and J.-M. Morel**, A non-local algorithm for image denoising. *In Computer Vision and Pattern Recognition, 2005. CVPR 2005. IEEE Computer Society Conference on*, volume 2. IEEE, 2005.
- Canny, J.** (1986). A computational approach to edge detection. *IEEE Transactions on pattern analysis and machine intelligence*, (6), 679–698.
- Chang, C.-C. and C.-J. Lin** (2011). Libsvm: a library for support vector machines. *ACM Transactions on Intelligent Systems and Technology (TIST)*, **2**(3), 27.
- Chao, S.-M. and D.-M. Tsai** (2010). An improved anisotropic diffusion model for detail- and edge-preserving smoothing. *Pattern Recognition Letters*, **31**(13), 2012–2023.
- Cheng, D.-c., A. Schmidt-Trucksäss, K.-s. Cheng, and H. Burkhardt** (2002). Using snakes to detect the intimal and adventitial layers of the common carotid artery wall in sonographic images. *Computer methods and programs in biomedicine*, **67**(1), 27–37.
- Christodoulou, C. I., C. S. Pattichis, M. Pantziaris, and A. Nicolaides** (2003). Texture-based classification of atherosclerotic carotid plaques. *Medical Imaging, IEEE Transactions on*, **22**(7), 902–912.



- C.Loizou** (2002). Ultrasound images from signal processing laboratory. URL <http://splab.cz/en/download/databaze/ultrasound>.
- Cohen, L. D.** (1991). On active contour models and balloons. *CVGIP: Image understanding*, **53**(2), 211–218.
- Coupé, P., P. Hellier, C. Kervrann, and C. Barillot** (2009). Nonlocal means-based speckle filtering for ultrasound images. *IEEE transactions on image processing*, **18**(10), 2221–2229.
- Criminisi, A., J. Shotton, E. Konukoglu, et al.** (2012). Decision forests: A unified framework for classification, regression, density estimation, manifold learning and semi-supervised learning. *Foundations and Trends® in Computer Graphics and Vision*, **7**(2–3), 81–227.
- Cyprus** (2007). E-health laboratory cs department. (available from : [www.medinfo.cs.ucy.ac.cy/index.php/downloads/datasets](http://www.medinfo.cs.ucy.ac.cy/index.php/downloads/datasets)).
- CyprusUniversity** (2007). E-health laboratory cs department. (available from : [www.medinfo.cs.ucy.ac.cy/index.php/downloads/datasets](http://www.medinfo.cs.ucy.ac.cy/index.php/downloads/datasets)).
- Delsanto, S., F. Molinari, P. Giustetto, W. Liboni, S. Badalamenti, and J. S. Suri** (2007). Characterization of a completely user-independent algorithm for carotid artery segmentation in 2-d ultrasound images. *IEEE Transactions on Instrumentation and Measurement*, **56**(4), 1265–1274.
- Destrempe, F., J. Meunier, M.-F. Giroux, G. Soulez, and G. Cloutier** (2009). Segmentation in ultrasonic b-mode images of healthy carotid arteries using mixtures of nakagami distributions and stochastic optimization. *IEEE Transactions on Medical Imaging*, **28**(2), 215–229.
- Dollar, P., Z. Tu, and S. Belongie**, Supervised learning of edges and object boundaries. In *Computer Vision and Pattern Recognition, 2006 IEEE Computer Society Conference on*, volume 2. IEEE, 2006a.
- Dollar, P., Z. Tu, and S. Belongie**, Supervised learning of edges and object boundaries. In *2006 IEEE Computer Society Conference on Computer Vision and Pattern Recognition (CVPR'06)*, volume 2. 2006b.

- Dollár, P.** and **C. L. Zitnick**, Structured forests for fast edge detection. *In Proceedings of the IEEE International Conference on Computer Vision*. 2013.
- Eberhart, R.** and **J. Kennedy**, A new optimizer using particle swarm theory. *In Micro Machine and Human Science, 1995. MHS'95., Proceedings of the Sixth International Symposium on*. IEEE, 1995.
- Ebrahim, S., O. Papacosta, P. Whincup, G. Wannamethee, M. Walker, A. N. Nicolaides, S. Dhanjil, M. Griffin, G. Belcaro, A. Rumley, and G. D. Lowe** (1999). Carotid plaque, intima media thickness, cardiovascular risk factors, and prevalent cardiovascular disease in men and women. *Stroke*, **30**(4), 841–850.
- Faita, F., V. Gemignani, E. Bianchini, C. Giannarelli, L. Ghiadoni, and M. Demi** (2008). Real-time measurement system for evaluation of the carotid intima-media thickness with a robust edge operator. *Journal of Ultrasound in Medicine*, **27**(9), 1353–1361.
- Farouj, Y., J. M. Freyermuth, L. Navarro, M. Clausel, and P. Delachartre** (2017). Hyperbolic wavelet-fisz denoising for a model arising in ultrasound imaging. *IEEE Transactions on Computational Imaging*, **3**(1), 1–10.
- Ferguson, G. G., M. Eliasziw, H. W. K. Barr, G. P. Clagett, R. W. Barnes, M. C. Wallace, D. W. Taylor, R. B. Haynes, J. W. Finan, V. C. Hachinski, and H. J. M. Barnett** (1999). The north american symptomatic carotid endarterectomy trial. **30**(9), 1751–1758.
- Freire, C. M. V., A. L. P. Ribeiro, F. B. L. Barbosa, A. I. Nogueira, M. C. C. de Almeida, M. M. Barbosa, Â. M. Q. Lana, A. C. S. e Silva, and A. Ribeiro-Oliveira Jr** (2009). Comparison between automated and manual measurements of carotid intima-media thickness in clinical practice. *Vascular health and risk management*, **5**, 811.
- Frost, V. S., J. A. Stiles, K. S. Shanmugan, and J. C. Holtzman** (1982). A model for radar images and its application to adaptive digital filtering of multiplicative noise. *Pattern Analysis and Machine Intelligence, IEEE Transactions on*, (2), 157–166.
- Garren, S. T.** (1998). Maximum likelihood estimation of the correlation coefficient in a bivariate normal model with missing data. *Statistics & probability letters*, **38**(3), 281–288.

- Ghita, O., D. E. Ilea, and P. F. Whelan** (2013). Texture enhanced histogram equalization using tv-image decomposition. *IEEE Transactions on Image Processing*, **22**(8), 3133–3144.
- Golemati, S., J. Stoitsis, E. G. Sifakis, T. Balkizas, and K. S. Nikita** (2007). Using the hough transform to segment ultrasound images of longitudinal and transverse sections of the carotid artery. *Ultrasound in medicine & biology*, **33**(12), 1918–1932.
- Golemati, S., T. J. Tegos, A. Sassano, K. S. Nikita, and A. N. Nicolaides** (2004). Echogenicity of b-mode sonographic images of the carotid artery. *Journal of ultrasound in medicine*, **23**(5), 659–669.
- Gonzalez, R. C. E., S. L. Woods, R. E. R. E. R. C. Gonzalez, R. E. Woods, and S. L. Eddins**, *Digital image processing using MATLAB*. 04; TA1637, G6. 2004.
- Gonzalez, W. and R. E. Woods** (2004). Eddins, digital image processing using matlab. *Third New Jersey: Prentice Hall*.
- Group, T. A. C. A. S.** (1994). Clinical advisory: Carotid endarterectomy for patients with asymptomatic internal carotid artery stenosis. *Stroke*, **25**, 2523–2524.
- Gustavsson, T., R. Abu-Gharbieh, G. Hamarneh, and Q. Liang**, Implementation and comparison of four different boundary detection algorithms for quantitative ultrasonic measurements of the human carotid artery. *In Computers in Cardiology 1997*. IEEE, 1997.
- Gutierrez, M., P. Pilon, S. Lage, L. Kopel, R. Carvalho, and S. Furuie**, Automatic measurement of carotid diameter and wall thickness in ultrasound images. *In Computers in Cardiology, 2002*. IEEE, 2002.
- Haider, W., M. S. Malik, M. Raza, A. Wahab, I. A. Khan, U. Zia, J. Tanveer, and H. Bashir** (2012). A hybrid method for edge continuity based on pixel neighbors pattern analysis (pnpa) for remote sensing satellite images. *International Journal of Communications, Network and System Sciences*, **5**(09), 624.
- Hassan, M., A. Chaudhry, A. Khan, and M. A. Iftikhar** (2014). Robust information gain based fuzzy c-means clustering and classification of carotid artery ultrasound images. *Computer methods and programs in biomedicine*, **113**(2), 593–609.

- Hassan, M., A. Chaudhry, A. Khan, and J. Y. Kim** (2012). Carotid artery image segmentation using modified spatial fuzzy c-means and ensemble clustering. *Computer methods and programs in biomedicine*, **108**(3), 1261–1276.
- Hassan1&2, N. and N. Akamatsu** (2009). A new approach for contrast enhancement using sigmoid function. *Int. Arab J. Inf. Technol.*, **11**(1), 22–28.
- Heath, M., S. Sarkar, T. Sanocki, and K. Bowyer**, Comparison of edge detectors: a methodology and initial study. In *Computer Vision and Pattern Recognition, 1996. Proceedings CVPR'96, 1996 IEEE Computer Society Conference on*. IEEE, 1996.
- Holdfeldt, P., M. Viberg, and T. Gustavsson**, A new method based on dynamic programming for boundary detection in ultrasound image sequences. In *Engineering in Medicine and Biology Society, 2008. EMBS 2008. 30th Annual International Conference of the IEEE*. IEEE, 2008.
- Hu, J. and X. Hu**, Application of median filter to speckle suppression in intravascular ultrasound images. In *Intelligent Information Systems, 1994. Proceedings of the 1994 Second Australian and New Zealand Conference on*. IEEE, 1994.
- Huang, C.-C., T. CHEN, T.-H. CHAO, and Y.-F. JUAN** (2004). The investigation of the relationship between carotid intima-media thickness and vascular compliance in patients with coronary artery disease. *Biomedical Engineering: Applications, Basis and Communications*, **16**(01), 37–42.
- Huang, D.-Y. and C.-H. Wang** (2009). Optimal multi-level thresholding using a two-stage otsu optimization approach. *Pattern Recognition Letters*, **30**(3), 275–284.
- Huang, S.-C., F.-C. Cheng, and Y.-S. Chiu** (2013). Efficient contrast enhancement using adaptive gamma correction with weighting distribution. *IEEE Transactions on Image Processing*, **22**(3), 1032–1041.
- Ilea, D. E., C. Duffy, L. Kavanagh, A. Stanton, and P. F. Whelan** (2013a). Fully automated segmentation and tracking of the intima media thickness in ultrasound video sequences of the common carotid artery. *IEEE transactions on ultrasonics, ferroelectrics, and frequency control*, **60**(1).

- Ilea, D. E., C. Duffy, L. Kavanagh, A. Stanton, and P. F. Whelan** (2013b). Fully automated segmentation and tracking of the intima media thickness in ultrasound video sequences of the common carotid artery. *IEEE Transactions on Ultrasonics, Ferroelectrics, and Frequency Control*, **60**(1).
- Ilea, D. E., P. F. Whelan, C. Brown, and A. Stanton**, An automatic 2d cad algorithm for the segmentation of the imt in ultrasound carotid artery images. *In 2009 Annual International Conference of the IEEE Engineering in Medicine and Biology Society*. IEEE, 2009.
- K. R. Subramanian, B. F. M. T. M. M. W. F., M. J. Thubrikar** (2000). Accurate 3d reconstruction of complex blood vessel geometries from intravascular ultrasound images: in vitro study. *Journal of Medical Engineering & Technology*, **24**(4), 131–140.
- Kanber, B., T. C. Hartshorne, M. A. Horsfield, A. R. Naylor, T. G. Robinson, and K. V. Ramnarine** (2013). Wall motion in the stenotic carotid artery: association with greyscale plaque characteristics, the degree of stenosis and cerebrovascular symptoms. *Cardiovascular Ultrasound*, **11**(1), 37.
- Kang, J., J. Y. Lee, and Y. Yoo** (2016). A new feature-enhanced speckle reduction method based on multiscale analysis for ultrasound b-mode imaging. *IEEE Transactions on Biomedical Engineering*, **63**(6), 1178–1191.
- Kaur, J., J. Kaur, and M. Kaur** (2011). Survey of despeckling techniques for medical ultrasound images. *Int. J. Comp. Tech. Appl*, **2**(4), 1003–1007.
- Kim, Y.-T.** (1997). Contrast enhancement using brightness preserving bi-histogram equalization. *IEEE transactions on Consumer Electronics*, **43**(1), 1–8.
- Kontschieder, P., S. R. Buló, H. Bischof, and M. Pelillo**, Structured class-labels in random forests for semantic image labelling. *In Computer Vision (ICCV), 2011 IEEE International Conference on*. IEEE, 2011.
- Kuan, D., A. Sawchuk, T. Strand, and P. Chavel** (1987). Adaptive restoration of images with speckle. *IEEE Transactions on Acoustics, Speech, and Signal Processing*, **35**(3), 373–383.
- Ladak, H. M., J. B. Thomas, J. R. Mitchell, B. K. Rutt, and D. A. Steinman** (2001). A semi-automatic technique for measurement of arterial wall from black blood mri. *Medical Physics*, **28**(6), 1098–1107.

- Lamont, D., L. Parker, M. White, N. Unwin, S. M. Bennett, M. Cohen, D. Richardson, H. O. Dickinson, A. Adamson, K. Alberti, et al.** (2000). Risk of cardiovascular disease measured by carotid intima-media thickness at age 49-51: lifecourse study. *Bmj*, **320**(7230), 273–278.
- Lee, J.-S.** (1986). Speckle suppression and analysis for synthetic aperture radar images. *Optical engineering*, **25**(5), 165–168.
- Li, H., S. Zhang, R. Ma, H. Chen, S. Xi, J. Zhang, and J. Fang** (2016a). Ultrasound intima-media thickness measurement of the carotid artery using ant colony optimization combined with a curvelet-based orientation-selective filter. *Medical physics*, **43**(4), 1795–1807.
- Li, H., S. Zhang, R. Ma, H. Chen, S. Xi, J. Zhang, and J. Fang** (2016b). Ultrasound intimamedia thickness measurement of the carotid artery using ant colony optimization combined with a curveletbased orientationselective filter. *Medical Physics*, **43**(4), 1795–1807.
- Li, Q., W. Zhang, X. Guan, Y. Bai, and J. Jia** (2014). An improved approach for accurate and efficient measurement of common carotid artery intima-media thickness in ultrasound images. *BioMed research international*, **2014**.
- Li, X. and Z. Zhang** (2017). Ultrasound speckle reducing anisotropic diffusion based on histogram curves matching. *Journal of Medical Imaging and Health Informatics*, **7**(1), 137–142.
- Liang, Q., I. Wendelhag, J. Wikstrand, and T. Gustavsson** (2000). A multiscale dynamic programming procedure for boundary detection in ultrasonic artery images. *IEEE transactions on medical imaging*, **19**(2), 127–142.
- Liguori, C., A. Paolillo, and A. Pietrosanto** (2001). An automatic measurement system for the evaluation of carotid intima-media thickness. *IEEE Transactions on instrumentation and measurement*, **50**(6), 1684–1691.
- Lim, J. J., P. Dollar, and C. L. Zitnick III** (2013). Learned mid-level representation for contour and object detection. US Patent App. 13/794,857.
- Liu, L.** (2008). Best: Bayesian estimation of species trees under the coalescent model. *Bioinformatics*, **24**(21), 2542–2543.

- Loizou, C. P.** (2014). A review of ultrasound common carotid artery image and video segmentation techniques. *Medical & biological engineering & computing*, **52**(12), 1073–1093.
- Loizou, C. P., T. Kasparis, T. Lazarou, C. S. Pattichis, and M. Pantziaris** (2014). Manual and automated intima-media thickness and diameter measurements of the common carotid artery in patients with renal failure disease. *Computers in biology and medicine*, **53**, 220–229.
- Loizou, C. P., T. Kasparis, C. Spyrou, and M. Pantziaris**, Integrated system for the complete segmentation of the common carotid artery bifurcation in ultrasound images. *In IFIP International Conference on Artificial Intelligence Applications and Innovations*. Springer, 2013.
- Loizou, C. P., A. Nicolaides, E. Kyriacou, N. Georghiou, M. Griffin, and C. S. Pattichis** (2015). A comparison of ultrasound intima-media thickness measurements of the left and right common carotid artery. *IEEE journal of translational engineering in health and medicine*, **3**, 1–10.
- Loizou, C. P., C. S. Pattichis, A. N. Nicolaides, and M. Pantziaris** (2009). Manual and automated media and intima thickness measurements of the common carotid artery. *IEEE transactions on ultrasonics, ferroelectrics, and frequency control*, **56**(5), 983–994.
- Loizou, C. P., C. S. Pattichis, M. Pantziaris, T. Tyllis, and A. Nicolaides** (2007). Snakes based segmentation of the common carotid artery intima media. *Medical & biological engineering & computing*, **45**(1), 35–49.
- Maini, R. and H. Aggarwal** (2009). Study and comparison of various image edge detection techniques. *International journal of image processing (IJIP)*, **3**(1), 1–11.
- Mairal, J., M. Leordeanu, F. Bach, M. Hebert, and J. Ponce** (2008). Discriminative sparse image models for class-specific edge detection and image interpretation. *Computer vision–ECCV 2008*, 43–56.
- Malik, J., S. Belongie, T. Leung, and J. Shi** (2001). Contour and texture analysis for image segmentation. *International journal of computer vision*, **43**(1), 7–27.

- Mao, F., J. Gill, D. Downey, and A. Fenster** (2000). Segmentation of carotid artery in ultrasound images: Method development and evaluation technique. *Medical physics*, **27**(8), 1961–1970.
- Masuda, M., T. Emoto, A. Suzuki, M. Akutagawa, T. Kitawaki, K. Kitaoka, H. Tanaka, S. Obara, K. Yoshizaki, S. Konaka, et al.** (2013). Evaluation of blood flow velocity waveform in common carotid artery using multi-branched arterial segment model of human arteries. *Biomedical Signal Processing and Control*, **8**(6), 509–519.
- Menchón-Lara, R.-M., M.-C. Bastida-Jumilla, J. Morales-Sánchez, and J.-L. Sancho-Gómez** (2014). Automatic detection of the intima-media thickness in ultrasound images of the common carotid artery using neural networks. *Medical & biological engineering & computing*, **52**(2), 169–181.
- Meyer, F.** (1994). Topographic distance and watershed lines. *Signal processing*, **38**(1), 113–125.
- Mojsilović, A., M. Popović, N. Amodaj, R. Babić, and M. Ostojić** (1997). Automatic segmentation of intravascular ultrasound images: a texture-based approach. *Annals of biomedical engineering*, **25**(6), 1059–1071.
- Molinari, F., C. S. Pattichis, G. Zeng, L. Saba, U. R. Acharya, R. Sanfilippo, A. Nicolaides, and J. S. Suri** (2012). Completely automated multiresolution edge snapper a new technique for an accurate carotid ultrasound imt measurement: clinical validation and benchmarking on a multi-institutional database. *IEEE Transactions on Image Processing*, **21**(3), 1211–1222.
- Molinari, F., G. Zeng, and J. S. Suri** (2010a). Intima-media thickness: setting a standard for a completely automated method of ultrasound measurement. *IEEE transactions on ultrasonics, ferroelectrics, and frequency control*, **57**(5).
- Molinari, F., G. Zeng, and J. S. Suri** (2010b). A state of the art review on intima–media thickness (imt) measurement and wall segmentation techniques for carotid ultrasound. *Computer methods and programs in biomedicine*, **100**(3), 201–221.
- Mughal, M., M. Khan, J. Demarco, A. Majid, F. Shamoun, and G. Abela** (2011). Symptomatic and asymptomatic carotid artery plaque. *Expert Review of Cardiovascular Therapy*, **9**(10), 1315–1330.



- Muthukrishnan, R.** and **M. Radha** (2011). Edge detection techniques for image segmentation. *International Journal of Computer Science & Information Technology*, **3**(6), 259.
- Nagaraj, Y., P. Madipalli, J. Rajan, P. K. Kumar,** and **A. Narasimhadhan** (2018). Segmentation of intima media complex from carotid ultrasound images using wind driven optimization technique. *Biomedical Signal Processing and Control*, **40**, 462 – 472.
- Nicolaides, A., M. Sabetai, S. Kakkos, S. Dhanjil,** *et al.* (2003). The asymptomatic carotid stenosis and risk of stroke (acsrs) study. *International angiology*, **22**(3), 263.
- Nowozin, S., C. H. Lampert,** *et al.* (2011). Structured learning and prediction in computer vision. *Foundations and Trends® in Computer Graphics and Vision*, **6**(3–4), 185–365.
- Otsu, N.** (1975). A threshold selection method from gray-level histograms. *Automatica*, **11**(285-296), 23–27.
- Oyeka, I. C. A.** and **G. U. Ebu** (2012). Modified wilcoxon signed-rank test. *Open Journal of Statistics*, **2**(02), 172.
- Pandit, A., M. Sharma,** and **R. Ramsankaran**, Comparison of the performance of the newly developed cdwm filter with enhanced lee and enhanced frost filters over the sar image. *In Industrial and Information Systems (ICIIS), 2014 9th International Conference on.* IEEE, 2014.
- Pignoli, P.** and **T. Longo** (1987). Evaluation of atherosclerosis with b-mode ultrasound imaging. *The Journal of nuclear medicine and allied sciences*, **32**(3), 166–173.
- Pižurica, A., W. Philips, I. Lemahieu,** and **M. Acheroy** (2003). A versatile wavelet domain noise filtration technique for medical imaging. *Medical Imaging, IEEE Transactions on*, **22**(3), 323–331.
- Quistgaard, J. U.** (1997). Signal acquisition and processing in medical diagnostic ultrasound. *IEEE Signal Processing Magazine*, **14**(1), 67–74. ISSN 1053-5888.
- Rafati, M., M. R. Rahimzadeh, F. Raygan, V. Nikseresht,** and **H. Moladoust** (2015). A new 2d-based method for carotid intima-media thickness quantification from ultrasound sequences. *Iranian Red Crescent Medical Journal*, **17**(3).
- Regionprop** (2002). Measure properties of image regions. (*available from* : <https://in.mathworks.com/help/images/ref/regionprops.html>).

- Rocha, R., A. Campilho, J. Silva, E. Azevedo, and R. Santos** (2010). Segmentation of the carotid intima-media region in b-mode ultrasound images. *Image and Vision Computing*, **28**(4), 614–625.
- Sagheer, S. V. M. and S. N. George** (2017). Ultrasound image despeckling using low rank matrix approximation approach. *Biomedical Signal Processing and Control*, **38**, 236 – 249.
- Selzer, R. H., W. J. Mack, P. L. Lee, H. Kwong-Fu, and H. N. Hodis** (2001). Improved common carotid elasticity and intima-media thickness measurements from computer analysis of sequential ultrasound frames. *Atherosclerosis*, **154**(1), 185–193.
- Sivakumar, R., M. K. Gayathri, and D. Nedumaran**, Speckle filtering of ultrasound b-scan images - a comparative study between spatial and diffusion filters. 2010.
- Solbo, S. and T. Eltoft** (2004). Homomorphic wavelet-based statistical despeckling of sar images. *IEEE Transactions on Geoscience and Remote Sensing*, **42**(4), 711–721.
- Sonka, M. and J. M. Fitzpatrick** (2000). Handbook of medical imaging, vol. 2: Medical image processing and analysis. *SPIE-International Society for Optical Engine*.
- Srivastava, R., J. Gupta, and H. Parthasarthy** (2010). Comparison of pde based and other techniques for speckle reduction from digitally reconstructed holographic images. *Optics and Lasers in Engineering*, **48**(5), 626–635.
- Stein, J. H., C. E. Korcarz, M. E. Mays, P. S. Douglas, M. Palta, H. Zhang, T. LeCaire, D. Paine, D. Gustafson, and L. Fan** (2005). A semiautomated ultrasound border detection program that facilitates clinical measurement of ultrasound carotid intima-media thickness. *Journal of the American Society of Echocardiography*, **18**(3), 244–251.
- Taskar, B., V. Chatalbashev, D. Koller, and C. Guestrin**, Learning structured prediction models: A large margin approach. *In Proceedings of the 22nd international conference on Machine learning*. ACM, 2005.
- Thompson, R. D.**, *Atmospheric processes and systems*. Psychology Press, 1998.
- Touboul, P.-J., P. Prati, P.-Y. Scarabin, V. Adrai, E. Thibout, and P. Ducimetière** (1992). Use of monitoring software to improve the measurement of carotid wall thickness by b-mode imaging. *Journal of hypertension*, **10**, S37–S42.

- Vert, J.-P., K. Tsuda, and B. Schölkopf** (2004). A primer on kernel methods. *Kernel Methods in Computational Biology*, 35–70.
- Vese, L. A. and S. J. Osher** (2003). Modeling textures with total variation minimization and oscillating patterns in image processing. *Journal of scientific computing*, **19**(1-3), 553–572.
- Walker, M. D., J. R. Marler, M. Goldstein, P. A. Grady, J. F. Toole, W. H. Baker, J. E. Castaldo, L. E. Chambless, W. S. Moore, J. T. Robertson, et al.** (1995). Endarterectomy for asymptomatic carotid artery stenosis. *Jama*, **273**(18), 1421–1428.
- Wang, Z., A. C. Bovik, H. R. Sheikh, and E. P. Simoncelli** (2004). Image quality assessment: from error visibility to structural similarity. *IEEE Transactions on Image Processing*, **13**(4), 600–612.
- Wells, P. N. T.** (2000). Current status and future technical advances of ultrasonic imaging. *IEEE Engineering in Medicine and Biology Magazine*, **19**(5), 14–20.
- Wendelhag, I., Q. Liang, T. Gustavsson, and J. Wikstrand** (1997). A new automated computerized analyzing system simplifies readings and reduces the variability in ultrasound measurement of intima-media thickness. *Stroke*, **28**(11), 2195–2200.
- WHO** (2013). World health organisation , cardiovascular disease. (available from : <http://www.who.int/cardiovascular diseases/en/>).
- Williams, D. J. and M. Shah** (1992). A fast algorithm for active contours and curvature estimation. *CVGIP: Image understanding*, **55**(1), 14–26.
- Wong, A., A. Mishra, K. Bizheva, and D. A. Clausi** (2010). General bayesian estimation for speckle noise reduction in optical coherence tomography retinal imagery. *Optics express*, **18**(8), 8338–8352.
- Xiao, G., M. Brady, J. A. Noble, and Y. Zhang** (2002). Segmentation of ultrasound b-mode images with intensity inhomogeneity correction. *Medical Imaging, IEEE Transactions on*, **21**(1), 48–57.
- Xiaofeng, R. and L. Bo**, Discriminatively trained sparse code gradients for contour detection. *In Advances in neural information processing systems*. 2012.

- Xu, X., Y. Zhou, X. Cheng, E. Song, and G. Li** (2012). Ultrasound intima–media segmentation using hough transform and dual snake model. *Computerized Medical Imaging and Graphics*, **36**(3), 248–258.
- Yang, X.-S.**, *Nature-inspired optimization algorithms*. Elsevier, 2014.
- Yu, Y. and S. T. Acton** (2002). Speckle reducing anisotropic diffusion. *IEEE Transactions on image processing*, **11**(11), 1260–1270.
- Zahalka, A. and A. Fenster** (2001). An automated segmentation method for three-dimensional carotid ultrasound images. *Physics in Medicine and Biology*, **46**(4), 1321.
- Zarins, C. K., C. Xu, and S. Glagov** (2001). Atherosclerotic enlargement of the human abdominal aorta. **155**(1), 157 – 164.
- Zhang, J., G. Lin, L. Wu, C. Wang, and Y. Cheng** (2015). Wavelet and fast bilateral filter based de-speckling method for medical ultrasound images. *Biomedical Signal Processing and Control*, **18**, 1 – 10.
- Zhang, Q., C. Li, H. Han, L. Yang, Y. Wang, and W. Wang** (2014). Computer-aided quantification of contrast agent spatial distribution within atherosclerotic plaque in contrast-enhanced ultrasound image sequences. *Biomedical Signal Processing and Control*, **13**, 50–61.
- Zheng, S., A. Yuille, and Z. Tu** (2010). Detecting object boundaries using low-, mid-, and high-level information. *Computer Vision and Image Understanding*, **114**(10), 1055–1067.
- Zong, X., A. F. Laine, and E. A. Geiser** (1998). Speckle reduction and contrast enhancement of echocardiograms via multiscale nonlinear processing. *IEEE transactions on medical imaging*, **17**(4), 532–540.
- Zuo, C., Q. Chen, X. Sui, and J. Ren** (2014). Brightness preserving image contrast enhancement using spatially weighted histogram equalization. *Int. Arab J. Inf. Technol.*, **11**(1), 25–32.

# Publications based on the thesis

## *A. Refereed International Journals:*

1. **Nagaraj Y**, Pardhu Madipalli, Jeny Rajan, P Krishna Kumar and A V Narasimhadhan, “Segmentation of intima media complex from carotid ultrasound images using wind driven optimization technique” (2017), *Journal of Biomedical Signal Processing and Control*, Vol.40 , pp. 462-472, **Elsevier Publisher. (SCI Indexed)**.  
doi:<https://doi.org/10.1016/j.bspc.2017.08.009>.
2. **Nagaraj Y**, Asha C S, Hema Sai Teja A and A V Narasimhadhan, “Carotid wall segmentation in longitudinal ultrasound images using structured random forest” (2018), *Journal of Computers & Electrical Engineering*, Vol., pp. **Elsevier Publisher. (SCI Indexed)**.  
doi:<https://doi.org/10.1016/j.compeleceng.2018.02.010>
3. **Nagaraj Y**, Hema Sai Teja A and A V Narasimhadhan, “Automatic segmentation of intima media complex in carotid ultrasound images using Support Vector Machine” (2018), *Journal of Arabian Journal of Science and Engineering*, Vol. , pp. **Springer Publisher. (SCI Indexed)**

## *B. Refereed National/International Conference Proceedings:*

1. **Nagaraj Y**, Asha C S and A V Narasimhadhan, (Nov, 2016), “Assessment of speckle denoising in ultrasound carotid images using least square Bayesian estimation approach”, *Region 10 Conference (TENCON)*, pp. 1001-1004, Singapore. **(Accepted)**
2. **Nagaraj Y**, A V Narasimhadhan, (Dec, 2017), “Comparison of edge detection algorithms in the framework of despeckling carotid ultrasound images based on Bayesian estimation approach”, *National Conference on Computer Vision, Pattern Recognition, Image Processing and Graphics (NCVPRIPG)*, Indian Institute of Technology, Mandi. **(Accepted)**

3. Pardhu Madipalli, Sandeep Kotta, Harish Dadi, **Nagaraj Y**, Asha C S and A V Narasimhadhan, (Feb, 2018), “Automatic segmentation of Intima Media Complex in Common Carotid Artery using Adaptive Wind Driven Optimization”, *National Conference on Communications (NCC)*, Indian Institute of Technology Hyderabad. **(Accepted)**



# NAGARAJ Y

Research scholar (EC14F06),  
Dept. of E&C Engg.,  
National Institute of Technology Karnataka,  
Surathkal, Karnataka - 575025, India.  
*Mobile:* +91 9620406299  
*Email :* nagraj.p.y@gmail.com

## EDUCATION

---

|  |              |
|--|--------------|
| <b>Ph.D(pursuing) Medical Image Processing</b><br><i>National Institute of Technology Karnataka</i><br>CGPA : 7.28 (Course Work) | 2014-Present |
| <b>M.Tech. Digital Signal Processing</b><br><i>Jain University</i><br>Percentage : 79.50   | 2010-2012    |
| <b>B.E Electronics and Communication Engineering</b><br><i>Visvesvaraya Technological University</i><br>Percentage : 61.50       | 2005-2009    |

## RESEARCH INTERESTS

---

- Medical Image Processing
- Computer Vision
- Machine Learning

## PERSONAL DETAILS

---

*Address:* , S/O P.N.Yamanakkanavar, Mruthunjaya Nagar 4th cross,  
Banashankari Badavane, Ranebennur  
Haveri District, Karnataka - 581115, India.  
*Email* nagraj.p.y@gmail.com  
nag.ec14f06@nitk.edu.in